**Title:** Glymphatic flow resistance in humans measured by multifrequency impedance dispersion

**Authors:** Paul Dagum, MD, PhD[1]; Laurent Giovangrandi, PhD[1]; Swati Rane Levendovszky, PhD[2]; Jake J. Winebaum[1]; Tarandeep Singh, MS[1]; Yeilim Cho, MD[3]; Robert M. Kaplan, PhD[4]; Michael S. Jaffee, MD[5]; Miranda M. Lim, MD, PhD[6,7,8]; Carla Vandeweerd[9,10], PhD; Jeffrey J. Iliff, PhD[3,11,12]

**Affiliations:** [1]Applied Cognition Inc, Redwood City, CA; [2]Department of Radiology, University of Washington School of Medicine, Seattle, WA; [3]VISN 20 NW Mental Illness Research, Education and Clinical Center, VA Puget Sound Healthcare System, Seattle, WA; [4]Clinical Excellence Research Center, Stanford University School of Medicine, Stanford, CA; [5] Department of Neurology, University of Florida Health, Gainesville, FL; [6]VISN 20 Northwest Mental Illness Research, Education and Clinical Center (MIRECC), VA Portland Health Care System, Portland, OR; [7]Neurology Service, Research Service, VA Portland Health Care System, Portland, OR; [8]Department of Neurology, Oregon Alzheimer's Disease Research Center, Oregon Health & Science University, Portland, OR; [9]University of Florida Health Precision Health Research Center, Clinical and Translational Science Institute, University of Florida, Gainesville, FL; [10]Health Outcomes and Biomedical Informatics, College of Medicine, University of Florida, Gainesville, FL; [11]Department of Psychiatry and Behavioral Science, University of Washington School of Medicine, Seattle, WA; [12]Department of Neurology, University of Washington School of Medicine, Seattle, WA;

**Corresponding Author:**
Paul Dagum, MD, PhD
Applied Cognition Inc
1629 Main St.
Redwood City, CA 94063
paul@appliedcognition.com
Ph: (415) 378-5456

**ABSTRACT**

Glymphatic function in animal models supports the clearance of brain proteins whose mis-aggregation is implicated in neurodegenerative conditions including Alzheimer's and Parkinson's disease. The measurement of glymphatic function in the human brain has been elusive, limiting its potential in translational research. Here we described a non-invasive multimodal device for the first-in-human continuous measurement of sleep-active glymphatic flow resistance using repeated electrical impedance spectroscopy measurements through two separate clinical validation studies. Device measurements successfully (i) paralleled sleep-associated changes in extracellular volume that regulate glymphatic function, (ii) replicated preclinical findings showing glymphatic function is increased with increasing sleep EEG delta power, and is decreased with increasing sleep EEG beta power and heart rate, and (iii) predicted glymphatic solute exchange measured by contrast-enhanced MRI. The present investigational device permits the continuous and time-resolved assessment of glymphatic flow resistance in naturalistic settings necessary to determine the contribution of glymphatic impairment to risk and progression of Alzheimer's disease, and to enable target-engagement studies that modulate glymphatic function in humans.

**Words 11957**

**Without methods 5467**

53 **INTRODUCTION**

54 The glymphatic system is a brain-wide network of perivascular pathways along which the
55 cerebrospinal fluid (CSF) surrounding the brain exchanges with brain interstitial fluid, supporting
56 nutrient distribution and waste clearance (**Figure 1a-b**). In animal models, glymphatic function
57 supports the clearance of amyloid beta[1,2], tau[3-5], and alpha synuclein[6,7], whose mis-aggregation
58 is implicated in the pathogenesis of neurodegenerative conditions including Alzheimer's and
59 Parkinson's disease. Glymphatic function is further postulated to be a mechanism for volume
60 transmission of the neurotransmitters acetylcholine, serotonin and norepinephrine, and of
61 neurohormones regulating brain-body homeostasis[8]. While this system is foundational to brain
62 health and disease, measurement of glymphatic function in the human brain, principally by
63 magnetic resonance imaging (MRI), is conducted in only a handful of academic neuroimaging
64 centers[9]. Without a consistent, reproducible and accessible way of measuring this important
65 neurobiology in humans, the promise of developing therapeutic interventions that target
66 glymphatic function to treat and prevent neurological and psychiatric diseases remains elusive.
67

68 Studies in rodents have demonstrated that glymphatic function is more rapid during sleep
69 compared to the awake state[2,10]. During periods of wakefulness, the interstitial space is narrow
70 and tortuous, forming a high-resistance pathway that suppresses glymphatic flow, while during
71 sleep fluid shifts from the intracellular compartment into the extracellular (interstitial) space,
72 widening these pathways, and enhancing glymphatic function by ~60% (**Figure 1c-d**).
73 Measuring glymphatic function across a range of physiological conditions demonstrated that
74 faster glymphatic exchange is associated with increased electroencephalogram (EEG) delta
75 band power, decreased EEG beta power, and reduced heart rate[11]. Studies utilizing contrast-
76 enhanced (CE)-MRI to measure solute exchange between the CSF and brain interstitial
77 compartments have confirmed in human participants more rapid glymphatic function during
78 sleep[12], although the poor temporal resolution of this approach[13-15] has not permitted the

relationship between EEG or cardiovascular features and glymphatic function to be defined in the human brain.

Electrical impedance spectroscopy (EIS) is widely used in medicine for body composition analysis and for monitoring cellular changes in settings including tumors and edema[16-19]. When alternating current is injected into tissue, at low frequencies the voltage drop depends primarily on the resistive pathway of the extracellular (interstitial) fluid, while at high frequencies cell membranes behave like capacitors allowing current to also pass relatively freely through the intracellular space (**Figure 1c-e**). This frequency dependence is the β-dielectric dispersion of the underlying tissue and its repeated measurement permits the detection of shifts in the extracellular and intracellular distribution of water within tissue[17,20].

We propose that the biophysics of EIS can be leveraged to measure the fluid shift that occurs with changes in sleep-active glymphatic function. Because intracranial volume is constant, any change in this frequency dependence across repeated EIS measures reflects changes in the resistance of the extracellular space, which is inversely proportional to the extracellular fluid volume (**Figure 1c-e**). Within the brain, the extracellular compartment includes the brain interstitial space (~16% of total volume) and a combination of CSF (~10%) and blood plasma (~6%)[21]. Small diurnal fluctuations occur in blood volume and in the CSF compartments, however these changes are small and offset one another across physiological states[22,23]. In contrast, sleep-wake differences in glymphatic function are associated with much larger shifts in the intracellular and particularly interstitial volumes[2]. Thus, sleep-wake changes in EIS measures will be sensitized to changes in brain intracellular and interstitial volume, and EIS-based measures of parenchymal resistance ($R_P$) may represent a novel approach to track sleep-active glymphatic function.

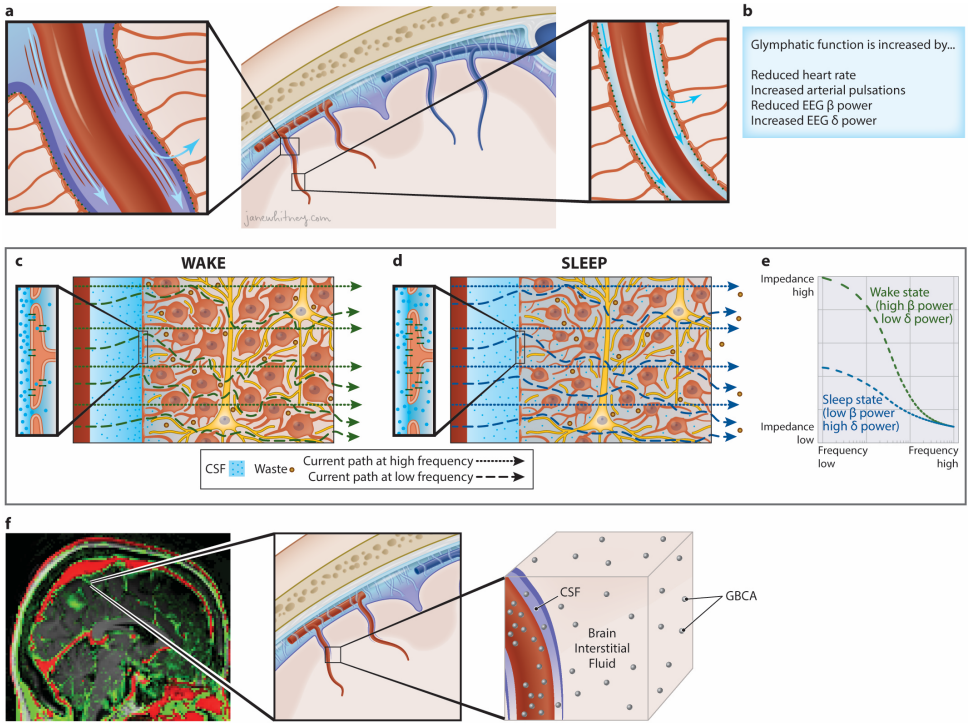


**Figure 1. Detection of sleep-wake changes in glymphatic flow resistance by impedance spectroscopy. a**, Glymphatic function involves the influx of cerebrospinal fluid (CSF) influx along perivascular spaces (PVSs) surrounding penetrating arteries (center). Glymphatic flow is driven by arterial pulsations and vasomotor oscillations (right). Astrocytic endfoot processes create the barrier between the PVS and the brain parenchyma, with gaps allowing CSF to exchange through the brain interstitial space. The endfoot processes are studded with perivascular aquaporin-4 water channels that also enable water to move into the astrocytes and out to the interstitial space. **b,** Data from physiological studies in rodents suggest that glymphatic function is increased in conditions of reduced heart rate, increased vasomotor pulsations, reduced EEG beta power, and increased EEG delta power (Hablitz et al. 2019). **c,** The interstitial space is dynamically regulated. Under conditions of low EEG delta power and high EEG beta power common to the awake state, it is narrow and tortuous, forming a high-resistance pathway that suppresses glymphatic function. When alternating current is injected into the brain parenchyma, at low frequencies the current cannot penetrate the capacitive cell membranes and its propagation depends primarily on the resistive pathway of the interstitial fluid. At high current frequencies, the current readily penetrates the capacitive cell membranes and its propagation depends on the resistance of the total tissue volume. This frequency difference is the β-dielectric dispersion of the underlying tissue. If the intracranial volume is constant, a change in the dielectric dispersion reflects a change in the low-frequency resistance pathway of the interstitial fluid. **d,** Under high EEG delta power and low EEG beta power common to the sleep state, fluid shifts from the intracellular compartment into the interstitial space, enhancing glymphatic function by ~60% in rodent studies (Xie et al. 2013). This widening of interstitial pathways reduces the current resistance at low-frequencies which reduces the measured dielectric dispersion. **e**, An impedance-frequency graph shows the change in dielectric dispersion between the two sleep/wake EEG states. The change in glymphatic flow resistance between these two states is inversely proportional to the relative change in the dielectric dispersion. **f,** Contrast-enhanced MRI following intravenous gadolinium-based contrast agent (GBCA) injection shows vascular regions that enhance immediately (t=30 min) upon GBCA injection (red), and CSF and brain parenchymal regions that enhance late (t=3 hrs) after leakage of GBCA first into the CSF and thence into the brain interstitium (green). A given MRI voxel includes GBCA within the blood, CSF and brain interstitial fluid compartments.

We developed a wearable investigational device (**Figure 2a-f**) that overcomes several technical challenges surrounding the implementation of EIS as a measure of glymphatic flow resistance. To define the dynamic relationship between $R_P$, sleep EEG features, and cardiovascular parameters through the course of an overnight period, EIS measurements must be made with high accuracy and temporal resolution. The investigational device performs measurements at frequencies between 1kHz and 256kHz and has a ~3% measurement error in $R_P$ (**Supplemental 4)** enabling it to detect small changes in dispersion between repeated measures. It is important to ensure that device measurements are not affected by changes in electrode impedances that can occur over time, including those caused by the effects of motion on the electrode-skin interface. A non-traditional four-electrode impedance configuration was used with multiple excitation and sense configurations in combination with low-impedance, non-polarizable electrodes. This ensured high-fidelity measurements including at low frequencies due to the reduced sensitivity to motion artifacts, low noise, and stability of the skin-gel-electrode interface. A signal processing approach enabled identification of signal from noise using the real and imaginary parts of the impedance to establish if the measured response is related to the excitation signal or has been distorted by artifact. The device further integrated shielded cables to reduce effects of electromagnetic interferences, both external and internal to the device, and the design minimized stray capacitances affecting higher frequencies. The device is described in more detail in **Methods** and **Supplemental Information** including **Supplemental Figure 2, Supplemental Figure 3** and **Supplemental Tables 7 – 12**. We note that glymphatic flow is determined by the parenchymal resistance to flow and the motive force driving CSF along the perivascular spaces (PVS) into the interstitial compartment. The resistance measured by the device is transcranial with a high temporal resolution of changes in global intracellular to interstitial fluid shifts.

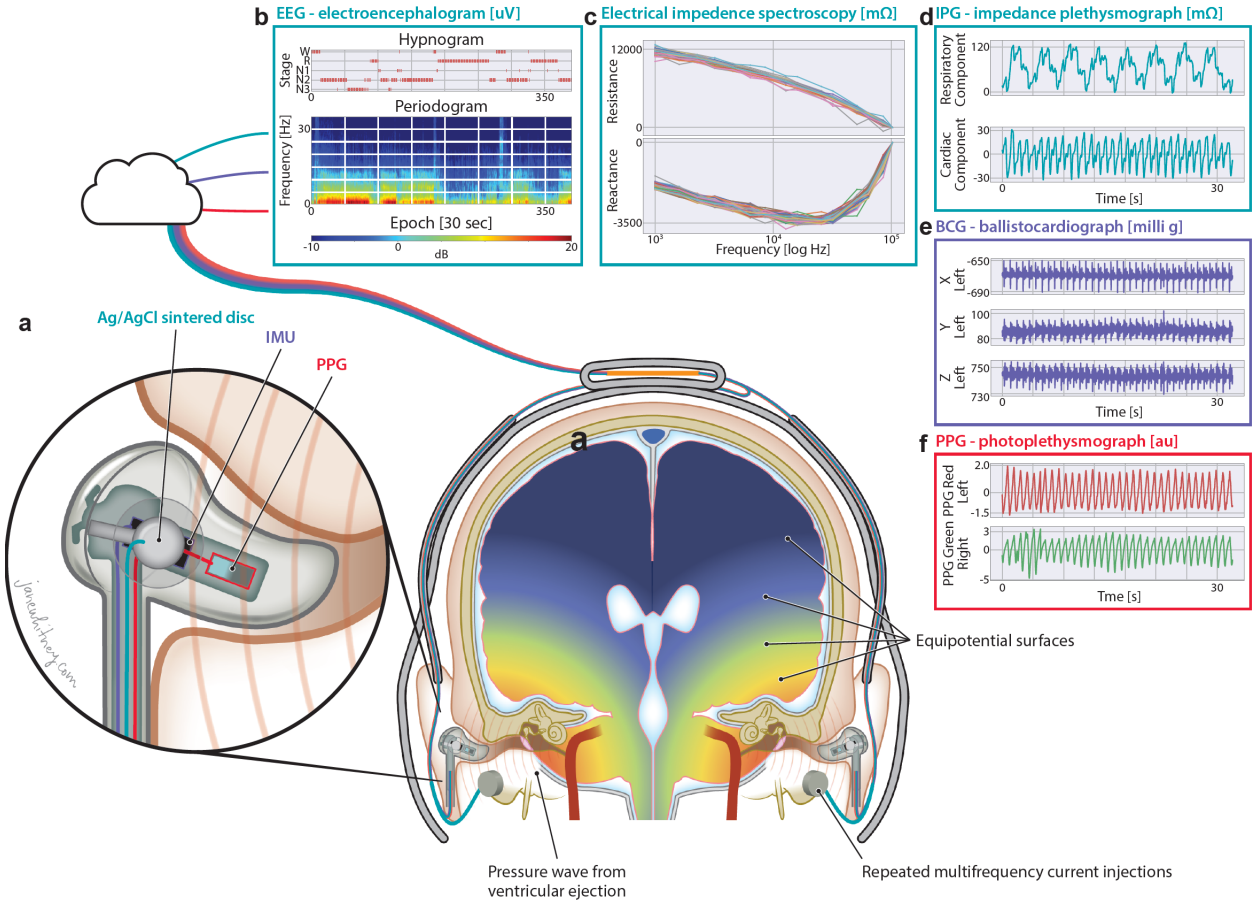


**Figure 2. Technical schematic of investigational device and its output signals.** Data for this study was acquired with a non-invasive multimodal skin-interfaced wireless device for continuous measurement of brain parenchymal resistance using repeated electrical impedance spectroscopy EIS time-multiplexed with EEG and cardiovascular measurements. EEG differential measurements were made between the two in-ear electrodes and a left mastoid was used to drive the common mode. These electrodes were shared with the EIS and the two measurements were time-multiplexed with a pair of analog multiplexers that decoupled EEG and EIS. The transcranial multi-frequency alternating current injections created an electric field through the brain and orthogonal equipotential surfaces. **a**, Each in-ear electronics housed PPG and IMU sensors. **b**, Data from the sensors were stored on the device's FLASH memory and transferred via a USB port to a cloud signal processing pipeline for offline analysis. Data from a participant visit is shown, which includes the device EEG periodogram and hypnogram. **c**, The EIS resistance and reactance frequency plots for this participant reveal an approximate 2000 mOhm change in the dielectric dispersion during the sleep visit. **d**, The IPG respiratory and cardiac impedance variations are 120 mΩ and 50 mΩ, respectively. **e**, Cardiac ejection of blood is detected by the in-ear IMUs in the ballistocardiogram. The J peak of the ballistocardiogram marks the aortic valve opening. **f**, Time delay between the ballistocardiogram and in-ear PPG measures the pulse-transit time (PTT) to the that ear.

## RESULTS

Data were acquired using the investigational medical device developed by Applied Cognition Inc[24,25]. Transcranial impedance dispersion is estimated from each EIS measure using a dielectric relaxation model. In addition to EIS measurements, the device measures EEG, photoplethysmogram (PPG), impedance plethysmogram (IPG) and head motion (**Figure 2a-f**). We propose that the change in transcranial impedance dispersion, which we will henceforth term parenchymal resistance $R_P$ ($R_P = R_0 - R_\infty$), reflects shifts in brain intracellular and interstitial compartment fluid volumes that underlie changes in glymphatic function (**Figure 1c-e**). **Supplemental 3** contains an intuitive justification of the physiological connection between EIS change and changes in glymphatic function. To test this, we evaluated whether $R_P$ measured with this device in human participants aligned with the central features of glymphatic function described in rodent models[2,11].

### *Study Design*

We conducted two clinical studies (denoted as "Benchmarking Study" and "Replication Study") to validate the performance of the device's $R_P$ measure as a surrogate of glymphatic flow resistance during sleep and wake (**Figure 3**, top). Both studies were cross-over trials where participants wearing the investigational device were subjected to one night of natural sleep and one night spent awake, separated by two or more weeks. The Benchmarking Study was conducted in The Villages® community, an active-lifestyle senior living community in Central Florida where the University of Florida maintains a satellite academic research center, The University of Florida Health Precision Health Research Center (UF Health PHRC). The Benchmarking Study was designed to define the effect of sleep on overnight $R_P$ measurements, as well as the relationship between $R_P$ and glymphatic function. It included overnight device recordings, overnight gold-standard polysomnography (PSG), and morning contrast-enhanced magnetic resonance imaging (CE-MRI) following intravenous gadolinium-based contrast agent

210 (GBCA) administration as a measure of glymphatic function. During the morning period,
211 following pre-contrast MRI scanning, GBCA injection, and immediate post-contrast MRI
212 scanning (totaling 2.5 hours spent awake), participants that were sleep deprived overnight were
213 provided a 1.5 hr sleep opportunity prior to the final MRI scan, while those that slept normally
214 overnight were kept awake during the 1.5 hr period (**Figure 3**, top). We evaluated whether, as
215 predicted from prior rodent studies on the sleep-modulation of glymphatic function[2,11], **a)** $R_P$ is
216 reduced in sleeping compared to awake participants, **b)** whether reduced $R_P$ is associated with
217 more rapid CSF-brain interstitial solute exchange measured by CE-MRI, **c)** whether $R_P$ is
218 associated with increasing sleep EEG delta power and decreasing sleep EEG beta power, and
219 **d)** whether reduced $R_P$ is associated with decreasing heart rate. The Replication Study
220 conducted at the University of Washington did not include overnight PSG or morning CE-MRI
221 and had as a primary outcome confirming the effect of sleep state on device-measured $R_P$, and
222 secondary outcomes confirming the associations between $R_P$ and sleep stages, heart rate, and
223 EEG spectral band power. As noted in the detailed study description in the Methods section,
224 these studies also evaluated novel non-contrast MRI measures of glymphatic function, sleep-
225 sensitive changes in cognitive function, and sleep-sensitive changes in plasma Alzheimer's
226 disease biomarkers across a range of physiological sleep conditions. Those findings will be
227 reported elsewhere.
228
229 **Inclusion and Exclusion Criteria**
230 All studies were performed between October 2022 – June 2023 and were reviewed and
231 approved by University of Florida Institutional Review Board (IRB No. 202201364,
232 Benchmarking Study) and Western Institutional Review Board (IRB No. 20225818, Replication
233 Study). The studies have been registered at ClinicalTrials.gov
234 (https://clinicaltrials.gov/study/NCT06222385 and https://clinicaltrials.gov/study/NCT06060054 ).
235 Written informed consent was obtained from all study participants during a screening visit, prior

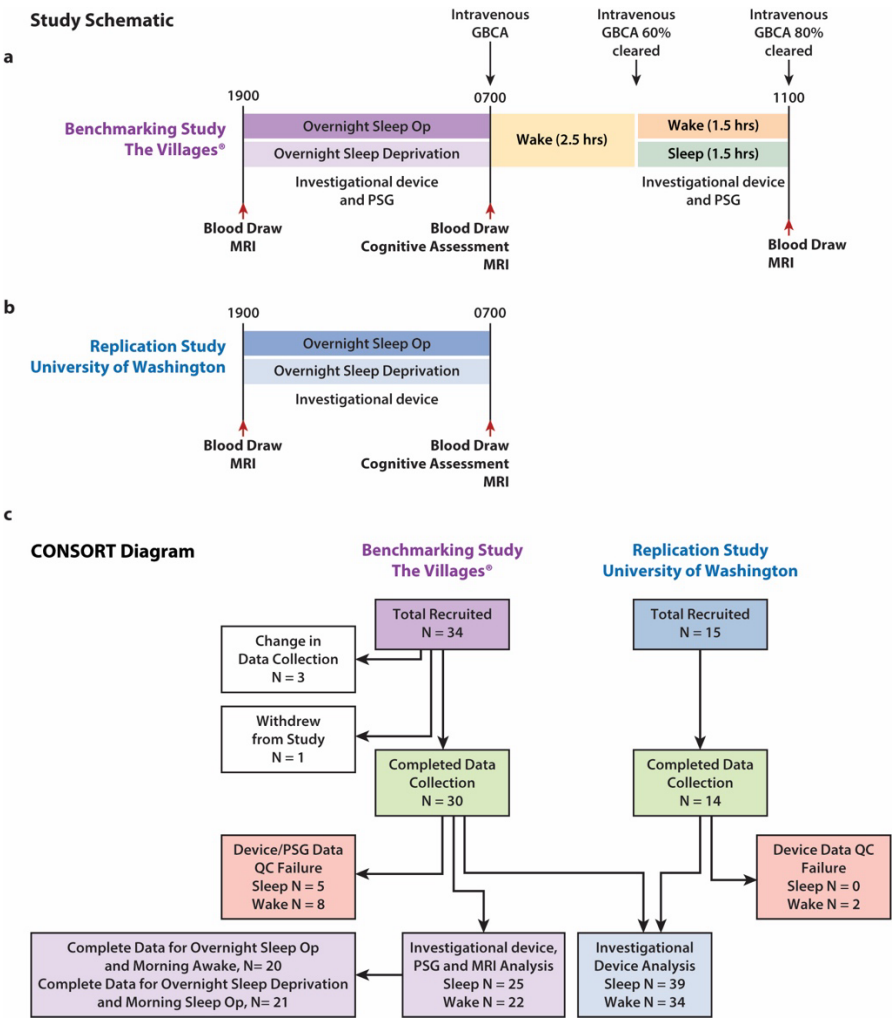


**Figure 3. Study schematic and CONSORT diagram for Benchmarking Study and Replication Study. a**, The Benchmarking Study conducted at The Villages® was designed to define the relationship between parenchymal resistance ($R_P$) and glymphatic function. Reported here are the overnight and morning device recordings, overnight and morning gold-standard polysomnography (PSG), and morning contrast-enhanced magnetic resonance imaging (CE-MRI) following intravenous gadolinium-based contrast agent (GBCA) administration as a measure of glymphatic function. Primary and secondary outcome data not reported here included blood analysis of amyloid β and tau levels, cognitive assessment, and non-contrast MRI. **b**, The Replication Study conducted at the University of Washington had a primary outcome of confirming the effect of sleep state on device-measured $R_P$, and secondary outcomes of confirming the associations between $R_P$ and sleep stages, heart rate, and EEG spectral band power. The Replication Study also included secondary outcomes on blood analyses for amyloid β and tau levels, cognitive assessment and non-contrast MRI. **c**, The Benchmarking Study enrolled 34 participants of which 30 completed both visits. Three were censored due to changes in device data collection and sensor locations. One withdrew following the first MRI scan. Of the 30 that completed the study, 5 overnight sleep visits and 8 overnight wake visits failed the data quality control (QC) criteria to provide sufficient artifact free data to yield results. This resulted in 25 sleep and 22 wake device, PSG and MRI complete data sets. Of these, 20 sleep and 21 wake device participants had complete data from both the overnight and morning sleep/wake periods. The Replication Study enrolled 14 participants. All 14 completed the study, of which 3 wake visits failed the data QC criteria and no sleep visit failed. (sleep op, sleep opportunity)

257 to any study activities. Studies were carried out in accordance with the principles of the Belmont
258 Report. The Benchmarking Study enrolled 34 healthy participants 56-66 years of age. The
259 Replication Study enrolled 14 healthy participants 49-63 years of age. Participants were
260 excluded if they had cognitive impairment or clinical depression. Cognitive impairment was
261 assessed using the Montreal Cognitive Assessment[26] (MoCA, 28.1 +/- 1.2; range 26, 30) and
262 depression was evaluated using the 15-item Geriatric Depression Scale[27] (GDS, 0.7 +/- 1.1;
263 range 0, 4). Participants with a self-reported history of diabetes, hypertension, coronary artery
264 disease, pulmonary disease, neurological disease, depression or anxiety were also excluded
265 from the study, as were participants planning travel to alternate time zones within two weeks of
266 study participation. Participant demographics, MoCA and GDS scores are listed for each study,
267 and for the combined dataset in **Supplemental Table 1**.
268
269 A Consolidated Standards of Reporting Trials (CONSORT) diagram for the Benchmarking Study
270 and Replication Study is provided in **Figure 3** (bottom). Within the Benchmarking Study, the first
271 three participants were removed from analysis because of a design change in the
272 investigational device sensor positions. One participant was unable to complete the first MRI
273 session and withdrew from the study. Of the remaining 30 participants (61.8 $\pm$ 2.7 years of age;
274 14 female, 16 male) that completed the Benchmarking Study, five overnight sleep studies and
275 eight overnight wake studies failed data quality control due to excessive artifacts in the
276 recordings, leaving 25 overnight sleep studies and 22 overnight wake studies in the
277 Benchmarking Study with complete device, PSG and MRI data. Excessive movement artifacts
278 during the morning recording periods resulted in the exclusion of data from five additional
279 morning wake and one additional morning sleep opportunity periods, leaving 20 overnight
280 sleep/morning wake and 21 overnight wake/morning sleep opportunity datasets with complete
281 overnight and morning data. All participants enrolled in the Replication Study (55.6 $\pm$ 4.6 years

282 of age; 7 female, 7 male) completed the protocol. All overnight sleep data were usable, but
283 three overnight wake studies were removed, two because of excessive artifact and one because
284 of non-compliance with the wake protocol. The higher number of quality control failures in the
285 Benchmarking Study was largely due to the physical challenges caused by simultaneous data
286 acquisition from both PSG and investigational device on the same night. Note that when the
287 investigational device was used in the absence of PSG in the Replication Study, quality control
288 failures were less frequent and restricted to motion artifacts in the awake condition.
289
290 ***Assessment of sleep and wake changes in parenchymal resistance***
291 Study participants underwent one night of normal sleep and one night of sleep deprivation
292 separated by 2-4 weeks. Sleep/wake or wake/sleep visit order was determined by random
293 assignment following informed consent. In the Benchmarking Study, sleep and wake status was
294 confirmed by PSG with anticipated differences in rapid eye movement (REM), and non-REM
295 (NREM: N1, N2, N3) sleep stages observed between sleep and wake conditions. Similar
296 differences were observed in the Replication Study, in which investigational device-based EEG
297 was used to evaluate sleep parameters. EEG was assessed with the investigational device in
298 both the Benchmarking and Replication Studies; these measures were used when combining
299 EEG parameters between both studies. Averaged hypnograms showing sleep stage distribution
300 throughout the overnight sleep period for the Benchmarking and Replication Studies are shown
301 in **Figure 4a-b** (top), respectively. The averaged hypnogram for the overnight and morning
302 periods for the Benchmarking study participants with complete data during both periods is
303 shown in **Figure 4c** (left)**.**
304
305 During the overnight period $R_P$ was continuously monitored. The results from the Benchmarking
306 Study are provided in **Figure 4a** (bottom), which depicts the mean and standard errors of
307 overnight $R_P$. Each participant's $R_P$ was normalized to the $R_P$ at onset of the observation period,

308 and linear interpolation was used for missing $R_P$ values within each participant. Compared to the
309 wake condition, overall $R_P$ during sleep was reduced by 8% (Wake 1.00 ± 0.06, Sleep 0.92 ±
310 0.06, T-test $p < 0.001$). When evaluated through the course of the overnight period, the $R_P$
311 during the wake period remained largely constant. In contrast, during the sleep period the mean
312 $R_P$ decreased monotonically, reaching at the end of the sleep period a nadir ~20% lower than at
313 onset or under the awake condition. Similar results were observed the Replication Study
314 (**Figure 4b**, bottom). Within the Benchmarking study, participants that were sleep deprived
315 overnight received a 1.5 hr sleep opportunity in the morning. Over this period, $R_P$ began at a
316 higher value (resulting from overnight sleep deprivation) but declined over the 1.5 hr sleep
317 opportunity (**Figure 4c**, right). Among participants that slept overnight but were kept awake in
318 the morning, $R_P$ during the morning period began at a low value (resulting from overnight sleep)
319 but increased over the 1.5 hr period of wakefulness. These data demonstrate across two study
320 populations that $R_P$ remains constant or increases during periods of waking but declines steadily
321 through periods of sleep.
322
323 ***Association between sleep parameters and glymphatic function***
324 Following the overnight sleep periods, participants in the Benchmarking Study underwent CE-
325 MRI for the assessment of glymphatic function. Beginning at 7am, participants underwent a pre-
326 contrast T1-weighted MRI scan, received intravenous GBCA (Gadavist, 0.1 mmol/kg), followed
327 by T1-weighted MRI scans at 7-10 min ($T_{10}$) and 240 min ($T_{240}$) post-injection. We evaluated
328 contrast enhancement in eight regions of interest (ROIs): frontal cortical gray and white matter,
329 parietal cortical gray and white matter, temporal cortical gray and white matter, and occipital
330 gray and white matter. Contrast enhancement at the $T_{10}$ time point primarily reflects GBCA
331 within the blood column, while enhancement at the $T_{240}$ time point reflects GBCA leakage into
332 the cerebrospinal fluid (CSF) and into the brain interstitial compartments[14,15]. Glymphatic
333 function was defined by measuring brain parenchymal contrast enhancement, the % change in

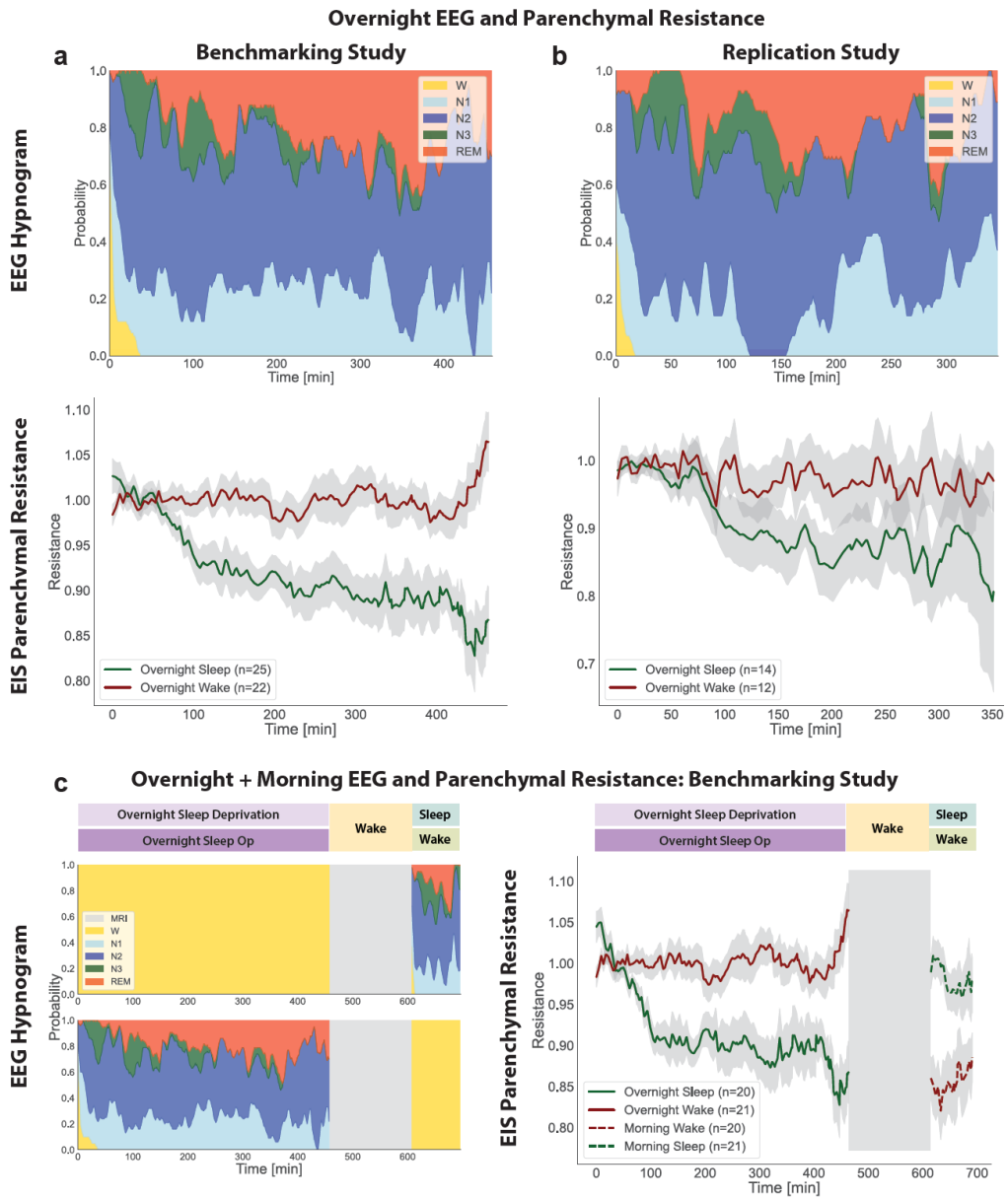


**Figure 4. Brain parenchymal resistance is reduced periods of sleep. a.** Averaged EEG hypnograms from the sleep condition are shown for the overnight period of the Benchmarking Study with WASO excluded in both the hypnograms and sleep $R_P$ (top). Over that period, parenchymal resistance ($R_P$, bottom) remained constant during the awake state (red) but declined gradually in the sleep state (green). **b.** Similar trends were observed in the Replication Study. **c.** During the morning period of the Benchmarking Study, participants underwent a 1.5 hr sleep opportunity or period of wakefulness. Averaged EEG hypnograms for the overnight and morning periods are shown at left. At right, during the morning awake period, $R_P$ increased gradually (dashed red), while it declined gradually during the sleep state (dashed green). Parenchymal resistances $R_P$ shown **(a)**, **(b)** and **(c)** are the average across the participants after normalizing each participant's $R_P$ measurements by their value at onset of the sleep or wake period. $R_P$ in **(c)** for morning wake is plotted starting at the ending value of overnight $R_P$ for illustration purposes. Standard error of the means are shown for each plot in light grey. The combined overnight and morning Benchmarking Study **(c)** includes participants who's overnight and morning data passed quality controls.

T1-weighted signal intensity between 10-240 min post-GBCA injection (100% * ($T_{240}$-$T_{10}$)/$T_0$) within each ROI.

To evaluate different sleep-related contributions to glymphatic function, we developed a general random intercept mixed model with eight ROI groups fit to the $T_{10}$-$T_{240}$ change in brain parenchymal enhancement. Our **null hypothesis** was that parenchymal contrast, including contrast in the interstitial compartment, was not influenced by sleep variables. Glymphatic function supports the movement of solutes into and out of the brain interstitial compartment, yet brain parenchymal enhancement includes contrast signal from the blood compartment (the initial source of the GBCA) and the CSF compartment (the intermediate space linking the blood and brain interstitium) in addition to the interstitial compartment (**Figure 1f**). Thus, we defined the **null model** to include regressors for vascular and CSF contrast in the mixed model: the $T_{10}$-$T_{240}$ change in blood signal within the internal carotid artery, and the $T_{10}$-$T_{240}$ change in CSF signal within the cerebral lateral ventricles. We also included the confounding biological variables of age, gender, and APOE ε4 status in the null model *shown in* **Supplemental** (bottom). The analyses of EEG powerbands, heart rate and sleep staging were performed on the overnight sleep period recordings. Pulse plethysmography and EEG were acquired concurrently and heart rate, EEG powerbands, sleep stage durations (REM; N1, N2, N3 NREM), number of awakenings and wake after sleep onset (WASO) were computed and included independently in the null model (**Supplemental Table 2**), and likelihood ratio tests used to compare the individual predictor model with the null model. Relative EEG delta, theta, alpha and beta powerbands were each expressed as the overnight mean of the powerband normalized to the average powerband value of the first three sleep epochs. Higher EEG delta power (mean 19.12, 95% CI 5.4819, 32.7599; P=0.0072), lower EEG alpha (mean -7.28, 95% CI -12.2638, -2.2935; P=0.0052) and beta (mean -5.33, 95% CI -7.7859, -2.8728; P<0.001) power were significantly associated with greater contrast enhancement. We next evaluated EEG-derived sleep stages within individual mixed models. Neither number of awakenings during

377 the sleep period, nor wake after sleep onset (WASO) were associated with parenchymal
378 contrast enhancement. Lower N1 sleep time was significantly associated with greater
379 parenchymal contrast enhancement (mean -0.1274, 95% CI -0.2130, -0.0420; P=0.0043), while
380 N2, N3 and REM sleep time had no significant association with parenchymal enhancement
381 within these individual models (**Supplemental Table 2**). Thus, within individual mixed models,
382 increased overnight EEG delta band power, reduced alpha and beta band power, and reduced
383 time in N1 sleep are each associated with greater glymphatic function, each rejecting the null
384 hypothesis that parenchymal contrast was not influenced by sleep variables (**Supplemental**
385 **Table 2**).
386
387 ***Direct association between parenchymal resistance and glymphatic function***
388 The device $R_P$ values were computed repeatedly throughout the overnight sleep period from
389 each EIS scan. During sleep recordings, the $R_P$ was non-stationary, decreasing throughout the
390 night as shown in **Figure 4a-c**. We observed that lower overnight $R_P$ was significantly
391 associated with higher glymphatic contrast enhancement (mean -38.08, 95% CI -61.34805, -
392 14.8115; P=0.0018, **Supplemental Table 2**).
393
394 ***Combined effects of overnight parenchymal resistance, EEG spectral power, and heart***
395 ***rate on glymphatic function***
396 We next utilized a comprehensive mixed model to define the contributions of $R_P$, EEG spectral
397 band power, and heart rate to parenchymal contrast enhancement. As in the individual mixed
398 models above, this comprehensive model extended the null model that contains only contrast
399 enhancement in the blood and cerebral ventricles as regressors, and age, APOE4 status, and
400 gender as confounding biological variables. We evaluated the relative delta, theta and beta
401 powerbands, omitting the alpha powerband to avoid multicollinearity in the model. We subjected
402 the model to a backward elimination algorithm with a Wald's p-value threshold of 0.05. **Table 1**

provides the full outputs of the analyses for each of the four intervention periods of overnight sleep opportunity, morning sleep opportunity, overnight sleep deprivation and morning awake of the study (**Figure 3**, top).

In reference to the models selected by backward elimination shown in **Table 1**, as expected, both blood and ventricular CSF contrast enhancement were strongly associated with parenchymal enhancement following the overnight sleep opportunity (blood mean 8.89; 95% CI 3.62, 14.16; P = 0.001; CSF mean 170.45; 95% CI 143.86, 197.04; P<0.001) and overnight sleep deprivation (blood mean 13.09; 95% CI 7.09, 19.10; P < 0.001; CSF mean 162.36; 95% CI 129.54, 195.19; P<0.001). For the overnight sleep opportunity, lower heart rate (mean -54.48, 95% CI -79.51, -29.45; P<0.001) and lower $R_P$ (mean -52.55, 95% CI -74.76, -33.33; P<0.001) predicted greater contrast enhancement. Reduced EEG beta power predicted greater parenchymal enhancement (mean -6.29, 95% CI -8.54, -4.05; P < 0.001), while neither delta nor theta power exhibited significant associations within the multivariate model. In the overnight sleep deprivation condition, reduced EEG delta power (mean -20.77, 95% CI -34.34, -7.20; P = 0.004) and increased theta power (mean 7.89, 95% CI 1.13, 14.64; P = 0.026) predicted greater parenchymal enhancement, while neither beta power, heart rate nor $R_P$ showed significant associations within the multivariate model.

***Combined effects of morning parenchymal resistance, EEG spectral power, and heart rate on glymphatic function***

As shown in the study schematic (**Figure 3**, top), between 7:10 am and 9:30am (140 min post-injection, $T_{140}$) participants underwent MRI scanning followed by instrumentation with the investigational device and PSG for the morning sleep opportunity or awake intervention. Because the mean terminal half-life of intravenous GBCA in adults with normal renal function is

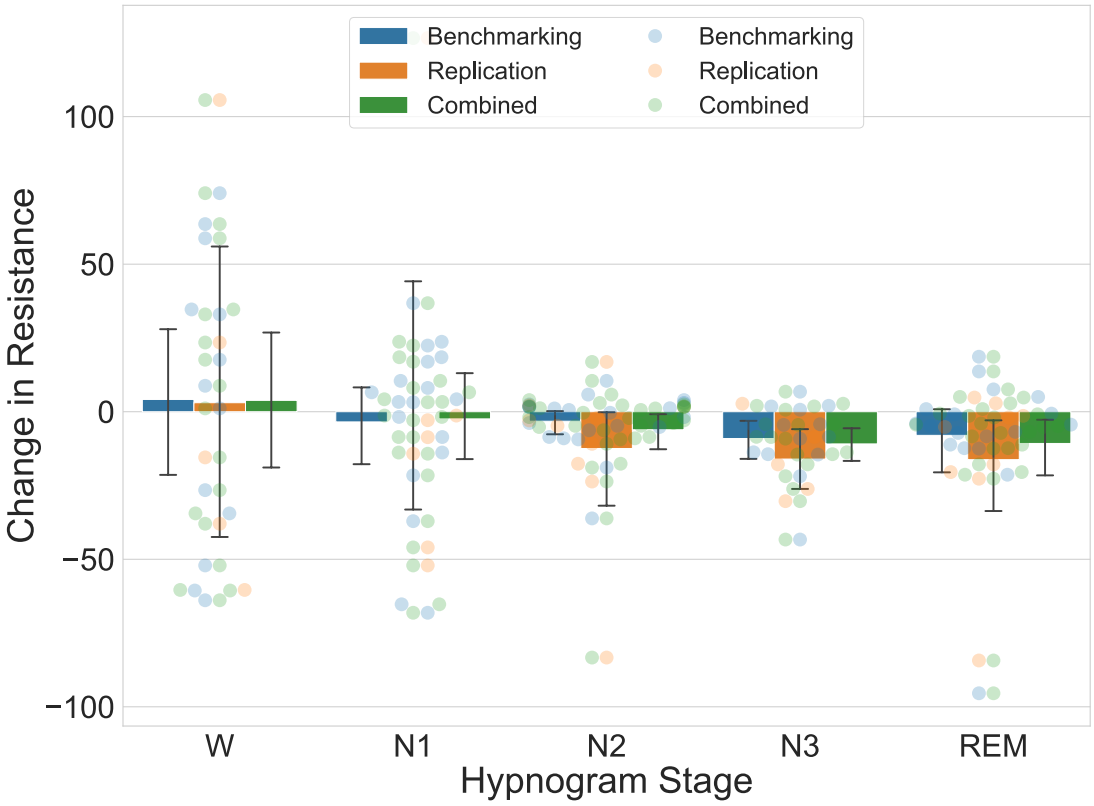


**Figure 5. Effect of sleep stages on $R_P$.** The mean first-order difference $\Delta R_P$ is shown by sleep stage and study for the overnight sleep period with 95% confidence intervals. During N2, N3 and REM sleep $\Delta R_P$ is negative for each study and when combined reaches significance. Benchmarking N2 (mean -3.21, 95% CI -9.07, -0.33; P = 0.113), N3 (mean -9.07, 95% CI -17.04, -3.75; P = 0.005), REM (mean -8.01, 95% CI -25.64, -1.18; P = 0.133). Replication N2 (mean -12.46, 95% CI -34.94, -1.49; P = 0.115), N3 (mean -16.04, 95% CI -25.32, -5.32; P = 0.002), REM (mean -16.24, 95% CI -42.19, -4.65; P = 0.065). Combined N2 (mean -6.10, 95% CI -14.78, -1.71; P = 0.04), N3 (mean -10.91, 95% CI -17.35, -5.93; P < 0.001), REM (mean -10.75, 95% CI -23.86, -3.91; P = 0.023). Units of $\Delta R_P$ are mΩ.

441 109 min[28], the post-injection blood contrast during the morning recordings was 60% cleared by
442 $T_{140}$ and 80% cleared by $T_{240}$. Glymphatic function in the period between $T_{140}$ and $T_{240}$, would
443 therefore dilute existing parenchymal contrast with CSF having 60% to 80% lower contrast
444 concentration, a process analogous to 'clearance' of interstitial contrast. Thus, we would expect
445 that an increase in glymphatic function during the period between $T_{140}$ and $T_{240}$ would be
446 reflected as reduced parenchymal contrast enhancement at $T_{240}$ (**Supplemental Figure 1**).
447
448 In reference to the models selected by backward elimination in **Table 1**, once again both blood
449 and ventricular CSF contrast enhancement were strongly associated with parenchymal
450 enhancement following the morning sleep opportunity (blood mean 11.73; 95% CI 7.89, 15.57;
451 P < 0.001; CSF mean 145.25; 95% CI 125.08, 165.42; P<0.001) and awake intervention (blood
452 mean 9.83; 95% CI 5.37, 14.29; P < 0.001; CSF mean 232.52; 95% CI 210.27, 254.77;
453 P<0.001). During the morning sleep opportunity, $R_P$ begins to decrease (**Figure 4c**). Higher
454 EEG delta power (mean -35.94, 95% CI -44.10, -27.78; P < 0.001) and lower $R_P$ (mean 55.35,
455 95% CI 33.01, 77.70; P < 0.001) predicted reduced parenchymal enhancement (greater
456 contrast clearance).
457
458 During the morning awake period, $R_P$ increases from its overnight sleep ending level (**Figure**
459 **4c**). During this intervention, higher EEG delta power (mean -20.98, 95% CI -30.19, -11.77; P <
460 0.001), theta power (mean -15.27, 95% CI -19.51, -11.03; P < 0.001) and beta power (mean -
461 21.38, 95% CI -24.34, -18.43; P < 0.001) predicted greater contrast clearance as did lower heart
462 rate (mean 235.70, 95% CI 201.64, 269.76; P < 0.001) and lower $R_P$ (mean 29.38, 95% CI 5.63,
463 53.13; P < 0.021). These findings are similar to those observed for the morning sleep
464 opportunity and consistent with the explanation that an increase in glymphatic influx of CSF
465 during this period dilutes the ISF contrast concentration and reduces the $T_{240}$ MRI signal
466 intensity.

**Table 1. Multivariate models of brain parenchymal contrast enhancement using $R_p$, HR and EEG power band predictors.**

| | | Full Model | | | Selected Model | | | Bootstrap Analysis | | | |
|---|---|---|---|---|---|---|---|---|---|---|---|
| **Predictor Period** | **Fixed Effect Predictors** | **Estimate** | **CI** | **p** | **Estimate** | **CI** | **p** | **Bootstrap Inclusion Frequency (%)** | **RMSD Ratio** | **Relative Conditional Bias (%)** | **Bootstrap Median** |
| **Overnight Sleep Opportunity** | Blood CE | 10.57 | (4.89, 16.25) | **<0.001** | 8.89 | (3.62, 14.16) | **0.001** | 100 | 1.00 | -11.89 | 9.22 |
| | CSF CE | 169.37 | (141.53, 197.22) | **<0.001** | 170.45 | (143.86, 197.04) | **<0.001** | 100 | 0.96 | 0.70 | 171.06 |
| | Age | 0.50 | (-0.03, 1.04) | 0.071 | – | – | – | 29.8 | 1.40 | 63.40 | 0 |
| | Male Sex | -6.10 | (-9.89, -2.31) | **0.002** | -2.98 | (-5.63, -0.34) | **0.030** | 61.0 | 1.10 | -29.97 | -3.19 |
| | APOE ε4 | 5.13 | (1.89, 8.37) | **0.003** | 4.29 | (1.13, 7.46) | **0.010** | 71.2 | 0.84 | -1.90 | 4.08 |
| | $R_P$ | -55.47 | (-77.74, -33.20) | **<0.001** | -52.55 | (-74.76, -30.33) | **<0.001** | 70.2 | 1.03 | 2.38 | -49.70 |
| | Delta Power | 12.69 | (-1.93, 27.32) | 0.098 | – | – | – | 28.0 | 1.25 | -15.65 | 0 |
| | Theta Power | -8.69 | (-18.01, 0.63) | 0.075 | – | – | – | 18.4 | 1.77 | -9.60 | 0 |
| | Beta Power | -5.21 | (-8.11, -2.32) | **0.001** | -6.29 | (-8.54, -4.05) | **<0.001** | 98.4 | 1.03 | 14.11 | -5.96 |
| | Heart Rate | -81.28 | (-112.92, -49.63) | **<0.001** | -54.48 | (-79.51, -29.45) | **<0.001** | 93.0 | 1.63 | -26.68 | -57.59 |
| **Morning Sleep Opportunity** | Blood CE | 10.76 | 6.24, 15.29 | **<0.001** | 11.73 | (7.89, 15.57) | **<0.001** | 99.6 | 0.89 | 3.26 | 11.30 |
| | CSF CE | 154.87 | 125.96,183.78 | **<0.001** | 145.25 | (125.08, 165.42) | **<0.001** | 100.0 | 1.02 | -0.58 | 151.27 |
| | Age | -1.38 | -1.95, -0.81 | **<0.001** | -1.26 | (-1.74, -0.79) | **<0.001** | 99.6 | 1.05 | -1.70 | -1.33 |
| | Male Sex | -0.36 | -2.75, 2.02 | 0.771 | – | – | – | 13.6 | 2.38 | 425.36 | 0 |
| | APOE ε4 | -2.89 | -6.31, 0.53 | 0.109 | -3.94 | (-6.74, -1.15) | **0.007** | 53.6 | 1.17 | 58.42 | -3.17 |
| | $R_P$ | 56.58 | 32.87, 80.29 | **<0.001** | 55.35 | (33.01, 77.70) | **<0.001** | 98.6 | 1.03 | -5.03 | 53.67 |
| | Delta Power | -39.36 | -51.30, -27.42 | **<0.001** | -35.94 | (-44.10, -27.78) | **<0.001** | 100.0 | 1.03 | -2.48 | -37.30 |
| | Theta Power | 9.01 | -6.18, 24.20 | 0.259 | – | – | – | 40.0 | 1.26 | 74.24 | 0 |
| | Beta Power | -2.68 | -12.06, 6.70 | 0.585 | – | – | – | 24.0 | 1.85 | 190.46 | 0 |
| | Heart Rate | 72.92 | 44.23, 101.62 | **<0.001** | 77.55 | (49.74, 105.35) | **<0.001** | 100.0 | 0.88 | 5.61 | 77.21 |
| **Overnight Sleep Deprivation** | Blood CE | 7.42 | -0.407, 15.25 | 0.076 | 13.09 | (7.09, 19.10) | **<0.001** | 56.6 | 1.59 | 72.95 | 8.57 |
| | CSF CE | 199.82 | 152.77, 246.87 | **<0.001** | 162.36 | (129.54, 195.19) | **<0.001** | 100.0 | 1.81 | -0.67 | 193.14 |
| | Age | 0.06 | -0.60, 0.72 | 0.871 | – | – | – | 4.0 | 2.01 | -118.25 | 0. |
| | Male Sex | -6.53 | -10.37, -2.70 | **0.002** | -4.81 | (-8.05, -1.57) | **0.005** | 90.8 | 0.96 | 1.08 | -6.23 |
| | APOE ε4 | 6.17 | -0.71, 13.05 | 0.093 | – | – | – | 58.4 | 1.60 | 60.69 | 6.40 |
| | $R_P$ | 12.37 | -31.98, 56.71 | 0.600 | – | – | – | 8.8 | 1.31 | 199.07 | 0 |
| | Delta Power | -31.79 | -54.44, -9.13 | **0.009** | -20.77 | (-34.34, -7.20) | **0.004** | 85.4 | 1.24 | 12.63 | -30.78 |
| | Theta Power | 19.96 | 7.38, 32.53 | **0.003** | 7.89 | (1.13, 14.64) | **0.026** | 83.8 | 1.45 | 7.75 | 19.85 |
| | Beta Power | -17.30 | -32.72, -1.89 | **0.036** | – | – | – | 62.0 | 1.26 | 42.29 | -17.71 |
| | Heart Rate | -25.01 | -63.14, 13.11 | 0.218 | – | – | – | 44.2 | 1.75 | 97.16 | 0 |
| **Morning Awake** | Blood CE | 10.58 | 5.67, 15.49 | **<0.001** | 9.83 | (5.37, 14.29) | **<0.001** | 98.0 | 0.86 | -5.59 | 9.91 |
| | CSF CE | 232.82 | 210.603, 255.04 | **<0.001** | 232.52 | (210.27, 254.77) | **<0.001** | 100.0 | 1.07 | 0.84 | 233.00 |
| | Age | -0.88 | -1.72, -0.04 | 0.049 | -0.72 | (-1.43, -0.01) | 0.057 | 63.8 | 1.14 | 28.44 | -0.81 |
| | Male Sex | 0.96 | -1.69, 3.61 | 0.495 | – | – | – | 20.2 | 2.18 | 223.65 | 0 |
| | APOE ε4 | 11.02 | 8.30,13.74 | **<0.001** | 10.54 | (8.16, 12.92) | **<0.001** | 100.0 | 1.63 | -2.35 | 10.62 |
| | $R_P$ | 25.30 | -0.93, 51.53 | 0.071 | 29.38 | (5.63, 53.13) | **0.021** | 64.0 | 1.15 | 51.96 | 30.70 |
| | Delta Power | -22.53 | -32.67, -12.39 | **<0.001** | -20.98 | (-30.19, -11.77) | **<0.001** | 98.6 | 1.38 | -5.75 | -21.33 |
| | Theta Power | -15.37 | -19.62, -11.134 | **<0.001** | -15.27 | (-19.51, -11.03) | **<0.001** | 100.0 | 1.15 | -2.22 | -15.00 |
| | Beta Power | -21.09 | -24.15, -18.04 | **<0.001** | -21.38 | (-24.34, -18.43) | **<0.001** | 100.0 | 1.13 | 0.73 | -21.42 |
| | Heart Rate | 230.91 | 194.43, 267.38 | **<0.001** | 235.70 | (201.64, 269.76) | **<0.001** | 100.0 | 1.19 | 0.74 | 234.67 |

Parenchymal Resistance, $R_P$; Heart Rate, HR; Contrast Enhancement, CE; 95% Confidence Interval, CI; Backward Elimination, BE; Root-Mean Square Deviation, RMSD; within ROI variability, $\sigma^2$; inter-ROI variability, $\tau_{00\ ROI}$. **Bolded P values reflect significant associations at P < 0.05**. Shaded cells demark the **null model** that includes blood CE, CSF CE and potential biological confounders.

472 We used bootstrap analysis of the backward elimination algorithm for stability investigations on
473 the impact of variable selection on bias and variance of the regression coefficient and bootstrap
474 inclusion frequencies. We estimated the multivariate model using the backward elimination
475 algorithm on 500 bootstrap data replicates with replacement for each intervention period (**Table**
476 **1**). The bootstrap inclusion frequency represents the percent of the 500 backward elimination
477 models that retained each variable, while the bootstrap median is the median estimate for that
478 variable. The relative conditional bias quantified the omitted variable selection bias of each
479 variable from inclusion/non-inclusion of other variables from the full model. In the overnight
480 sleep opportunity, in addition to vascular and CSF contrast enhancement (each with an
481 inclusion frequency of 100%), $R_P$ (70.2%), EEG beta power (98.4%), and heart rate (93.0%) had
482 high bootstrap inclusion frequencies and bootstrap median estimates comparable to the
483 selected model estimates. Device-measured $R_P$ and ventricular contrast enhancement had the
484 lowest relative conditional bias, and therefore their predictions of parenchymal contrast uptake
485 were least affected by inclusion of the other variables. Findings in the morning sleep opportunity
486 also showed high inclusion frequencies of the variables retained in the backward elimination
487 algorithm on the full data set and bootstrap median estimates comparable to the selected model
488 estimates, with vascular contrast enhancement (99.6%), CSF contrast enhancement (100%), $R_P$
489 (98.6%), EEG delta power (100%), and heart rate (100%). These regressors also had low
490 relative conditional bias. These analyses suggest high model stability to perturbations of the
491 data set[29].
492
493 Lastly, we computed the percent of the residual variance of the null model that was explained by
494 including EEG power band, heart rate and $R_P$ regressors for each intervention and computed
495 the LRT between the null model and the intervention models. For the overnight sleep and sleep
496 deprivation interventions, 24.5% and 12.7% of the residual null model variance was explained
497 by including these regressors, respectively. The null hypothesis that parenchymal contrast

498 enhancement is not influenced by these variables was rejected for the overnight sleep model
499 (likelihood ratio 52.6, p-value < 0.001) and the sleep deprivation model (likelihood ratio 14.1, p-
500 value = 0.015). Including the regressors in morning sleep and awake models explained 38.3%
501 and 74.8% of the residual null model variance, respectively. The null hypothesis that the
502 parenchymal contrast enhancement is not influenced by these variables during the morning
503 sleep (likelihood ratio 79.5, p-value < 0.001) and awake condition (likelihood ratio 149.6, p-value
504 < 0.001) were also both rejected.
505
506 ***Combined effects of parenchymal resistance and sleep stages on glymphatic function***
507 We developed a second comprehensive mixed model to define the relationship among $R_P$,
508 sleep stages, heart rate and parenchymal contrast enhancement. As above, this comprehensive
509 model extended the null model that contained contrast enhancement in the blood and cerebral
510 ventricles as regressors, and age, APOE4 status, and gender as confounding biological
511 variables. We evaluated WASO time, and time in N1, N2, N3 and REM sleep stages.
512 **Supplemental Table 3** provides the model output for the overnight sleep opportunity (top) and
513 the morning sleep opportunity (bottom). In the overnight sleep opportunity model selected by
514 backward elimination, as before lower $R_P$ was significantly associated with greater parenchymal
515 contrast enhancement (mean -67.17; 95% CI -87.78, -46.56; P<0.001). In this model, more time
516 in REM sleep (mean 0.16; 95% CI 0.09, 0.23; P<0.001), and less time in N1 (mean -0.32; 95%
517 CI -0.43, -0.21; P<0.001), N2 (mean -0.10; 95% CI -0.15, -0.06; P<0.001), N3 (mean -0.07; 95%
518 CI -0.12, 0.02; P=0.007) sleep and WASO (mean -0.07; 95% CI -0.12, -0.02; P=0.006) were
519 each associated with greater contrast enhancement. Bootstrap analysis showed that blood and
520 CSF contrast enhancement (each with an inclusion frequency of 100%), as well as $R_P$ (100%),
521 REM sleep time (99.0%), N1 sleep time (98.8%) and N2 sleep time (98.0%) were the most
522 stable elements of the model relating sleep stages to parenchymal glymphatic function, while
523 the RMSD ratio for N2 sleep time, N3 sleep time and WASO showed substantial variance

524 deflation following backward elimination (**Supplemental Table 3**) that is associated with weak
525 or noise predictors.
526
527 In the morning sleep opportunity model selected by backward elimination, lower $R_P$ was
528 significantly associated with greater parenchymal contrast clearance (mean 34.42; 95% CI 5.25,
529 63.59; P = 0.025), similar to the EEG band power model for this intervention. In this model, less
530 time in REM sleep (mean 0.41; 95% CI 0.20, 0.62; P<0.001), and more time in N1 (mean -0.26;
531 95% CI -0.50, -0.02; P=0.04) and N3 (mean -0.17; 95% CI -0.33, -0.021; P=0.031) were
532 associated with less contrast enhancement, or greater contrast clearance. N3 sleep did not
533 survive bootstrap analysis while $R_P$, REM and N1 sleep had inclusion frequencies of 65.4%,
534 88.2% and 61.6%, respectively (**Supplemental Table 3).**
535
536 ***Effects of sleep stages on brain parenchymal resistance***
537 To understand if sleep stages had a differential effect on the overnight change in $R_P$, we
538 computed the mean of the first-order differences $\Delta R_P$ for each sleep stage for the Benchmarking
539 and Replication studies separately and combined (**Figure 5**). The mean $\Delta R_P$ was negative and
540 largest for N2, N3 and REM sleep stages reaching significance when the values for both studies
541 where pooled together. This suggests that $R_P$ in **Figure 4a-c** decreases during N2, N3 and
542 REM sleep.
543
544 ***Effects of large changes in EEG spectral power on brain parenchymal resistance***
545 To define the relationships between sleep EEG powerbands, heart rate and $R_P$, we modeled the
546 relationship between the first-order difference $\Delta R_P$ and the difference in spectral band power
547 ($\Delta$delta, $\Delta$theta, $\Delta$alpha, $\Delta$beta) and changes in heart rate $\Delta$HR, during NREM, REM and Wake
548 (**Table 2**). We utilized threshold regression to model the relationships between $\Delta R_P$ and large

changes in (Δ) band power or heart rate. A custom estimation procedure described in **Supplemental Information** was used to jointly estimate the threshold regression for the full positive and negative ranges of Δ band power and ΔHR. The full output of the threshold regression models is provided for the combined study data in **Table 2**. In both REM and NREM sleep, a large increase in Δdelta was significantly associated with a decrease in $\Delta R_P$ (**Figure 6a**). In contrast during REM and NREM sleep, a large increase in Δbeta was significantly

**Table 2. The change in parenchymal resistance resulting from large changes in EEG band power and heart rate occurring during REM sleep, NREM sleep, wake, and at NREM-REM and sleep-wake transitions.**

| | | | Fixed Effects | | | | Threshold Model Parameters | | |
|---|---|---|---|---|---|---|---|---|---|
| **Study Condition** | **Period** | **Predictors** | **Estimate** | **CI** | **p** | **DF** | **Positive Threshold** | **Negative Threshold** | **Slope Ratio** |
| **Overnight Sleep Op** | **NREM** | Δdelta | -0.28 | (-0.50, -0.058) | **0.014** | 1380 | 1.5 | -1.5 | 0.7 |
| | | Δtheta | -0.08 | (-0.23, 0.063) | 0.265 | 1380 | 1.5 | -0.98 | 0.5 |
| | | Δalpha | -0.14 | (-0.30, 0.022) | 0.091 | 1380 | 1.5 | -1.25 | 0.65 |
| | | Δbeta | 0.04 | (0.0022, 0.080) | **0.039** | 1380 | 0.18 | -1.5 | 2 |
| | | ΔHR | 0.10 | (-0.0033, 0.19) | 0.059 | 1115 | 0.43 | -0.43 | 0.5 |
| | **REM** | Δdelta | -0.57 | (-0.77, -0.37) | **<0.001** | 319 | 1.5 | -1.5 | 2 |
| | | Δtheta | -0.41 | (-0.70, -0.13) | **0.005** | 319 | 0 | -1.5 | 0.5 |
| | | Δalpha | -0.09 | (-0.21, 0.041) | 0.189 | 319 | 1.45 | 0 | 2 |
| | | Δbeta | 0.45 | (0.14, 0.77) | **0.006** | 319 | 1.5 | -1.3 | 0.5 |
| | | ΔHR | 0.31 | (-0.057, 0.68) | 0.101 | 271 | 1.5 | -1.15 | 0.5 |
| | **NREM to REM** | Δdelta | -0.29 | (-0.82, 0.24) | 0.293 | 67 | 1.5 | -1.05 | 2 |
| | | Δbeta | 0.77 | (0.04, 1.49) | **0.046** | 67 | 0.6 | -1.5 | 0.5 |
| | **REM to NREM** | Δdelta | -1.50 | (-2.35, -0.66) | **0.001** | 58 | 1 | -1.5 | 0.5 |
| | | Δbeta | -0.05 | (-0.24, 0.14) | 0.615 | 58 | 0.1 | -1.5 | 1.85 |
| | **Sleep to Wake** | Δdelta | 0.03 | (-0.34, 0.4) | 0.885 | 66 | 1.5 | -0.3 | 1.95 |
| | | Δbeta | 0.73 | (0.13, 1.32) | **0.021** | 66 | 0.35 | -1.23 | 0.5 |
| | **Wake to Sleep** | Δdelta | -0.20 | (-0.64, 0.25) | 0.392 | 113 | 0.05 | -1.35 | 0.6 |
| | | Δbeta | 0.37 | (-0.01, 0.76) | 0.065 | 113 | 1.5 | -1.05 | 2 |
| **Overnight Sleep Deprivation** | **WAKE** | Δdelta | -0.06 | (-0.15, 0.034) | 0.216 | 1137 | 1.5 | 0 | 0.5 |
| | | Δtheta | -0.07 | (-0.17, 0.035) | 0.198 | 1137 | 1.4 | -1.45 | 2 |
| | | Δalpha | 0.06 | (-0.030, 0.14) | 0.206 | 1137 | 1.15 | 0 | 0.73 |
| | | Δbeta | 0.12 | (0.0075, 0.23) | **0.037** | 1137 | 1.5 | -1.43 | 1.93 |
| | | ΔHR | -0.10 | (-0.20, -0.011) | **0.029** | 1002 | 0.25 | -0.25 | 0.5 |

Rapid eye movement, REM; non-REM, NREM; Confidence Interval, CI; Degrees of Freedom, DF; EEG band power predictor units in percent of total band power; HR predictor units beats-per-minute. **Bolded P values reflect significant associations at P < 0.05**. Predictor and parenchymal resistance values in regression models were scaled to zero mean and unit standard deviation with coefficient estimates representing effect size in standard deviations. Positive and negative thresholds are in units of predictor standard deviation. Models included confounding biological variables age, gender, and APOE ε4 status.

associated with an increase in $\Delta R_P$. The threshold models for the significant estimated effects of $\Delta$ band power on $\Delta R_P$ are plotted in **Figure 6b**. The full output of the threshold regression model is provided for each site individually in **Supplemental Table 4**. Because the variables were standardized before model estimation, the regression estimates in **Table 2** and **Supplemental Table 4** can be interpreted as standardized effect sizes. Note that because of the slope ratio $r$, changes that exceed the positive change point $t_p$ have effect sizes given by the regression estimate multiplied by the slope ratio. The positive and negative thresholds are in units of standard deviation.

The asymmetric effect of EEG band power changes on $R_P$ shown in Figure 5 accounts for the progressive decline in $R_P$ that occurs through the course of the overnight sleep period, shown in **Figure 4a-c**. In the overnight wake state, $\Delta$beta had a significant but small effect on $\Delta R_P$. $\Delta$HR in NREM and wake had a small effect on $\Delta R_P$ and a larger but non-significant effect in REM. The threshold model findings in **Table 2** and plots in **Figure 6a** demonstrate that large changes in spectral band power are needed to alter $R_P$. Because such large changes in EEG powerbands and HR occur at sleep stage transitions, we explored the associations between $\Delta$delta and $\Delta$beta and $\Delta R_P$ at NREM-REM and REM-NREM transitions, and at Sleep-Wake and Wake-Sleep transitions. **Table 2** provides the full model output on sleep stage transitions for data pooled from both study sites, while the significant estimated effects of $\Delta$delta and $\Delta$beta on $\Delta R_P$ are plotted in **Figure 6c**. The full output of the threshold regression model on sleep stage transitions is provided for each site individually in **Supplemental Table 5**. During the NREM-REM, Wake-Sleep, and Sleep-Wake transitions, changes in EEG beta power and not EEG delta power underlie the observed changes in $\Delta R_P$. In contrast, during the REM-NREM transition, changes in EEG delta power and not beta power were associated with changes in $\Delta R_P$. In total,

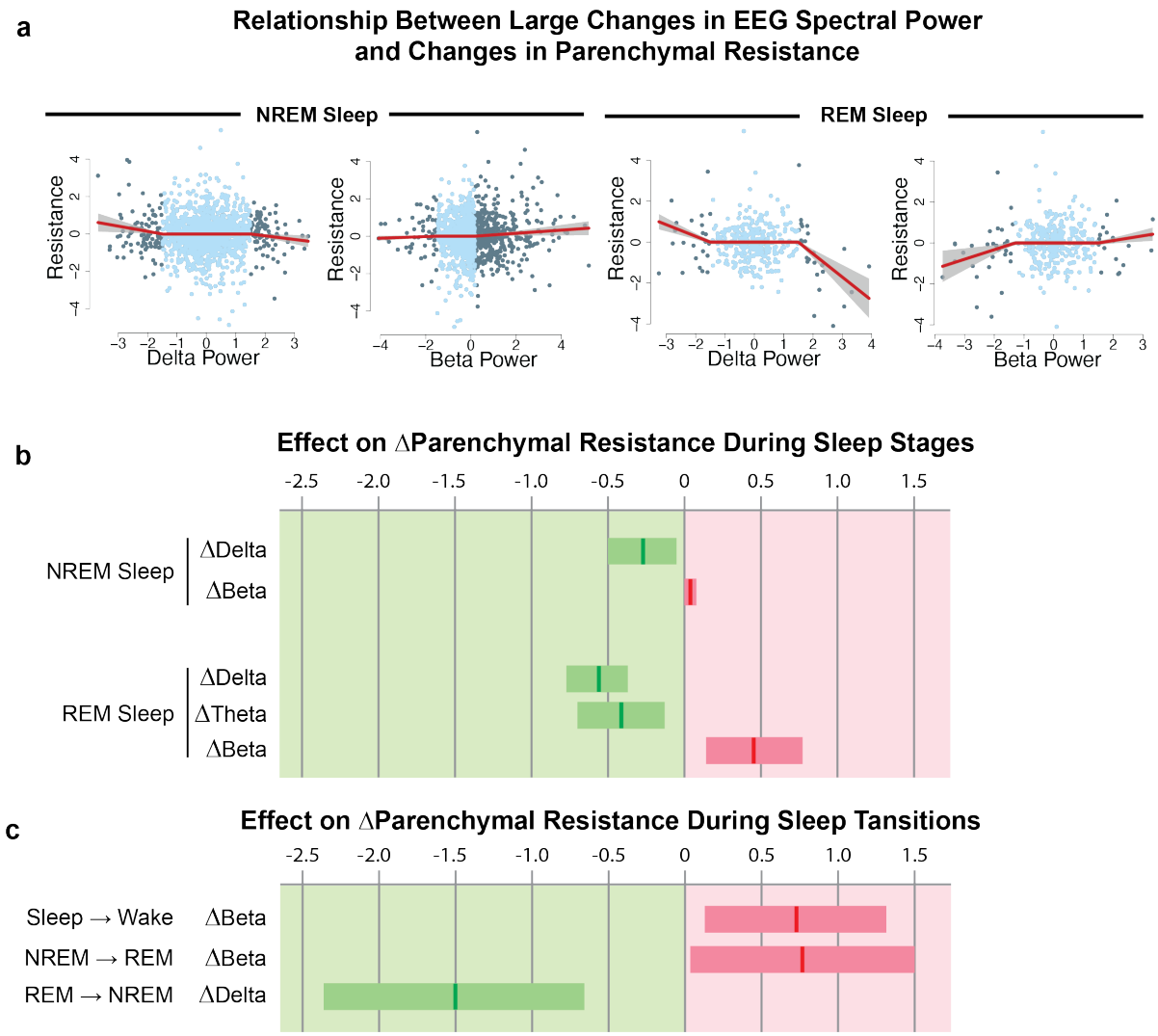


**Figure 6. Brain parenchymal resistance is increased by large changes in EEG beta power and reduced by large changes in EEG delta power. a**, Threshold linear mixed regression model of $R_P$ against EEG delta and beta power for REM and NREM sleep shown with standard error after differencing both $R_P$ and powerband values to make data stationary, standardizing the $\Delta R_P$ and $\Delta$ powerband values to zero mean and unit standard deviation, and adjusting for site, age, gender, APOe4 and site-age interaction confounders. Units of $\Delta R_P$ and $\Delta$ powerband are in standard deviations. Data in light blue are inside the change points and data in dark blue are outside the change points. When delta and beta power changes between successive measurements exceed 1.0 to 1.5 stand deviations, we observe significant changes in $\Delta R_P$**. b**, 95% CI of regression coefficients show that large changes in REM delta, theta and beta, and NREM delta and beta are significant predictors of $\Delta R_P$. For a 1 standard deviation increase in $\Delta$ powerband, an increase (decrease) in $\Delta R_P$ is illustrated in red (green) with units along the top in standard deviation of $\Delta R_P$. **c**, Large changes in beta and delta powerbands at sleep-wake and NREM-REM transitions show significant effect on $\Delta R_P$ consistent with the step change in beta and delta power at these transitions. For a 1 standard deviation increase in $\Delta$ powerband across a sleep-wake or NREM-REM transition, an increase (decrease) in $\Delta R_P$ is illustrated in red (green) with units along the top in standard deviation of $\Delta R_P$.

these data show that glymphatic function is enhanced by declining $R_P$, and that $R_P$ in turn declines with reduced EEG beta power and heart rate, and with increasing EEG delta power.

## DISCUSSION

We have described a non-invasive multimodal skin-interfaced wireless device for continuous measurement of brain parenchymal resistance $R_P$ using repeated EIS time-multiplexed with EEG and cardiovascular measurements. Through two separate clinical validation studies, we observe that brain $R_P$ measured by the device faithfully captures sleep-active changes in glymphatic flow resistance based on three complementary criteria established from studies in the murine and human brain. Brain $R_P$ declines overnight, paralleling sleep-associated changes in extracellular volume that regulate glymphatic function[2]. Brain $R_P$ is reduced with increasing sleep EEG delta power, and is increased with increasing sleep EEG beta power and heart rate[11]. Lastly, brain $R_P$ is a robust predictor of glymphatic function, measured by CE-MRI[12-15,30]. These findings demonstrate that this investigational device provides the first remote, non-invasive, and time-resolved measure of glymphatic flow resistance suitable for defining this sleep-active biology in naturalistic settings.

Several technological advances have enabled this work. We have developed a technique for low-noise EIS measurements using multiple excitation and sense configurations to determine the brain parenchymal impedances accurately. A signal processing approach enabled the segregation of signal and noise, using the Kramers-Kronig relations[31,32] between the real and imaginary parts of the impedance to establish if the measured response is related to the excitation signal or has been distorted by noise or other artifact. Unlike applications of EIS to neurological conditions such as seizures, tumors or cerebral edema[33-36], the rapid evolution of

636 glymphatic function during sleep and its nightly variability make it suitable for monitoring with
637 longitudinal repeated assessments. Data collected under a variety of scenarios in benchtop
638 testing, agar phantom testing with biological interfaces and in-human testing indicate that this
639 system yields consistent, repeatable results and shows longitudinal stability of the measured
640 impedances.
641
642 A key first step in validating any potential measure of glymphatic function is assessing its
643 performance against established, principally contrast-based, measures of glymphatic exchange.
644 Initial studies characterizing glymphatic function in rodents utilized dynamic in vivo
645 fluorescence-based imaging[1,2,37]. More recent studies in rodents, and recently in human
646 participants, have utilized CE-MRI following either intrathecal or intravenous GBCA
647 injection[12,14,15,30,38]. We evaluated whether device-based $R_P$ measures reflect glymphatic
648 function by measuring overnight and morning $R_P$, EEG, and the movement of GBCA into brain
649 tissue over a four-hour timeframe. In the analysis, both overnight and morning $R_P$ emerged as
650 robust explanatory variables of net contrast movement, in a regression model that included CSF
651 and blood contrast levels, EEG neurophysiological parameters, age, gender and APOE e4
652 confounders. It is important to note that device-based $R_P$ measures are acquired with 2-minute
653 temporal resolution whereas CE-MRI captures overall glymphatic function over a 4-hour
654 window. This fine temporal resolution enabled translational validation of the physiological drivers
655 of glymphatic function in the human brain for the first time. It further revealed that while key
656 events during sleep were necessary to lower parenchymal resistance $R_P$, low $R_P$ was sufficient
657 to enhance glymphatic function independent of sleep in the morning period. In addition, it
658 showed that sleep-related changes in RP do not shift with sleep-wake in a stepwise fashion, but
659 rather accumulate through the course of time spent sleeping or awake. These observations are
660 not inconsistent with prior studies in rodents that used real-time iontophoresis to measure sleep-
661 associated increases in brain extracellular volume fraction[2], as these observational studies did

662 not directly test the causal effect of these changes in extracellular volume on glymphatic
663 function, and did not monitor changes in extracellular volume fraction in a time-resolved manner
664 over extended period. Future studies of the determinants of glymphatic function in human sleep
665 will likely further refine existing conceptual models of sleep-wake regulation of glymphatic
666 function.
667
668 The physiological mechanisms regulating glymphatic function have been defined almost
669 exclusively through experimental rodent studies[1,2,10,11,30,37,39,40], due in large part to invasiveness
670 and poor temporal resolution of contrast-based measures of glymphatic function[12-15,30]. It is
671 noteworthy that these rodent studies are not all in agreement. While multiple studies have
672 reported more rapid glymphatic exchange under conditions of sleep, or under certain anesthetic
673 regimes[2,11,41-45], two studies[46,47] have reported apparently slower clearance during sleep or
674 under anesthesia. In the present human clinical studies, we demonstrate within-participant
675 longitudinal declines in brain $R_P$ during overnight sleep, but not in awake participants. During
676 morning recovery sleep, we demonstrate within-participant longitudinal declines in brain $R_P$ and
677 during morning wake we observe increases in brain $R_P$. This pattern is consistent with sleep-
678 wake changes in extracellular volume fraction measured in mice and reported by Xie et al.[2].
679 Using overnight PSG followed by CE-MRI in human participants, we confirmed that glymphatic
680 function in the human brain is associated with lower EEG beta power and heart rate, and in a
681 simplified model with increasing EEG delta power. These findings sustain the physiological
682 findings in mice from Hablitz et al.[11]. More broadly, these human CE-MRI-based imaging studies
683 demonstrate that glymphatic solute exchange is more rapid under conditions of natural sleep, at
684 least in human participants, and that these sleep-wake differences are regulated by sleep-
685 related changes in $R_P$, heart rate, and EEG spectral band power.
686

687 Linking changes in $R_P$ with sleep EEG features, we further demonstrate that the investigational
688 device-based measure of $R_P$ exhibits the same dependence upon EEG delta power, EEG beta
689 power, and heart rate during sleep. Conducting parallel time-resolved sleep EEG and $R_P$
690 measurements, we observed that rapid changes in $R_P$ occurred at sleep stage transitions
691 between REM and NREM, and between sleep and wake. Transitions between REM and NREM
692 exhibit large changes in EEG delta and beta powerbands, and in HR, consistent with our
693 findings. Large changes in an EEG power within a frequency band can occur because of
694 sudden bursts of oscillatory activity within the band's frequency range. In rodents, recent
695 experiments support a role for such synchronized oscillatory activity as a mechanism driving
696 glymphatic flow by creating propagating ionic waves within the brain interstitium[41]. To our
697 knowledge, this is the first time that these physiological drivers of glymphatic function have been
698 confirmed in human participants, within an experimental setting permitting validation against
699 current benchmark CE-MRI-based measures of glymphatic function well established preclinical
700 features.
701
702 There are clear limitations both of the investigational device, and of the present study design.
703 Existing MRI-based measures of glymphatic function remain poorly time-resolved but provide
704 excellent cranium-wide anatomical resolution. In contrast, the present investigational device
705 captures a measure of global brain glymphatic flow resistance with high temporal resolution.
706 While finer anatomical resolution may have value in future iterations of the investigational
707 device, it is important to note that the present design was sufficient to capture sleep-wake
708 changes in glymphatic function, and to define novel neurophysiological drivers of these
709 processes in the human brain. Study methodological limitations include protocol differences
710 between the Benchmarking Study and Replication Study. The Benchmarking Study included
711 CE-MRI as part of the neuroimaging package and gold-standard PSG concurrent with the
712 device usage whereas the Replication Study did not include CE-MRI and used the device's

single-derivative EEG. Furthermore, the Benchmarking Study enrolled participants 55-65 years old living in Florida whereas the Replication Study enrolled participants 50-65 years old living on the West Coast. Despite these differences, after adjusting for age, study site and age-site interaction effects, we confirmed that the device's single-derivative EEG showed good agreement with the PSG of the Benchmarking Study. Additionally, the pooled analysis and study-specific analyses of $R_P$, EEG and HR were all in good agreement between studies. The Benchmarking Study was powered to detect a low to moderate correlation between $R_P$ and CE-MRI measures of glymphatic function, which was confirmed. Quality control of the investigational device filtered out measurements that did not satisfy the Kramers-Kronig relations[31,32]. Failed measurements were more common in the Benchmarking Study, particularly during the awake conditions. This is attributable to excessive motion, likely due to the technical challenges associated with conducting concurrent PSG and device-based sleep EEG measures in participants being kept awake by study staff. The low rate of quality-control failures in the Replication Study that did not involve PSG instrumentation supports this conclusion.

The characterization of the glymphatic system in rodents beginning in 2012 has spurred a great deal of interest into its potential mechanistic role linking sleep to cognitive performance, and sleep disruption to a wide range of neurological and psychiatric conditions including Alzheimer's disease, Parkinson's disease, chronic traumatic encephalopathy, stroke, traumatic brain injury, headache and others[42-45]. Preclinical studies have demonstrated that glymphatic function is impaired in the setting of aging[48], sleep disruption[2], cerebrovascular injury[49,50], and traumatic brain injury[3], all risk factors for neurodegenerative conditions including Alzheimer's disease. Experimental impairment of glymphatic function is sufficient to promote the development of the amyloid beta[51-53] and tau pathology[3-5] characteristic of Alzheimer's disease. In clinical populations, genetic and histological associations support a link between glymphatic dysfunction and the development of clinical disease[52,54-56]. Yet the technical challenges of real-time dynamic

739 measurements of glymphatic function in human clinical populations have proven a challenging
740 barrier to defining the causal role of glymphatic function and dysfunction in the development of
741 neurological and psychiatric conditions in these populations. Whether glymphatic dysfunction
742 contributes to development of conditions such as Alzheimer's disease remains to be directly
743 tested. The present investigational device may permit the continuous and time-resolved
744 assessment of glymphatic function in naturalistic settings necessary to define whether
745 glymphatic impairment contributes to risk and progression of Alzheimer's disease and its
746 underlying pathological processes. The ability to assess glymphatic function over short
747 timescales may enable target-engagement studies to identify and test pharmacological, device-
748 based and lifestyle/behavioral interventions for modulating glymphatic function in humans.
749 Assessment of these processes may also permit the identification of clinical populations with
750 impaired glymphatic function, at risk for the development of Alzheimer's disease, and who would
751 thus be ideal candidates for therapeutic approaches targeting glymphatic clearance. Similar
752 avenues now remain open outside the realm of neurodegenerative conditions as glymphatic
753 dysfunction is implicated in an ever-increasing list of sleep-related neurological and psychiatric
754 conditions.

## METHODS

### *Investigational Device*

*System Architecture*

The Applied Cognition device is a wearable multi-sensor acquisition system that uses an STM32WB5MMG microcontroller (ST Microelectronics, NV). It consists of a primary module housing the main electronics board and a 430 mAh Li-ion battery, two earpieces each housing one electrode, one accelerometer and one photoplethysmogram sensor, and two separate mastoid electrodes. A device schematic and visualization of signal outputs is provided in **Figure 2a-f**. Sensor data is stored in on-board FLASH memory and is downloaded via a USB port for offline analysis. The relevant sub-systems are further described below.

*Electrical Impedance Spectroscopy*

Electrical impedance spectroscopy (EIS) was used to measure electrical impedance using the AFE4500 analog front-end (AFE) from Texas Instruments. Four electrodes – two in-ear and two mastoid – were used to deliver the excitation current across the head and sense the resulting voltage. The two mastoid current injection sources were initially co-located inside the ear next to the Ag/AgCl sensors but because of salt-bridging were externalized to the mastoids. In a departure from traditional four-electrode measurements, where excitation and sense electrodes are fixed, the AFE4500 was programmed to implement a technique developed by Texas Instruments where multiple excitation and sense configurations are used to determine the contact impedance and body impedance accurately.

Measurements were successively performed at eighteen frequencies ranging from 1 kHz to 256 kHz following a logarithmic series, all with excitation current below 50 μA root-mean-square (rms). Frequencies were in alternating order from high-low to minimize any impact on impedance drift during each scan. Sensed voltages were quadrature-demodulated, filtered and

digitized internally by the AFE4500 to provide in-phase and out-of-phase components. Measurement time for each frequency was adjusted to give consistent signal-to-noise ratio across the frequency range, resulting in a scan time of 106 seconds.

*Electroencephalogram*

Electroencephalogram (EEG) was measured with an ADS1299-4 AFE from Texas Instruments, between the two in-ear electrodes (differential measurement). A third electrode (left mastoid) was used to drive the common mode. While these electrodes were shared with the EIS, the two measurements were time-multiplexed and a pair of analog multiplexers (TMUX1136, Texas Instruments, Inc.) effectively decoupled EEG and EIS sub-circuits and respective measurements. For EEG, both in-ear electrodes were also buffered (OPA376, Texas Instruments, Inc.) in the earpiece. These buffers were bypassed (analog multiplexer TMUX1136, Texas Instruments, Inc.) for EIS or electrode impedance measurement.

The ADS1299-4 was programmed to have a sampling rate of 250 samples-per-second (24-bit samples) and an input range of ±180 mV. The common mode drive was actively derived from the in-ear electrodes. Both mastoid electrodes were also connected to an input channel so that the low-frequency (31.25 Hz) impedance of each electrode could be measured using the internal current source of the ADS1299-4. Such impedance measurements were performed before starting a recording session, and then automatically between EEG periods and EIS. EEG measurement periods were 170 seconds long, and the sequence EEG-EIS-Electrode impedance repeated until the end of the recording session. A sample EEG spectrogram and hypnogram, derived from the device EEG is shown in **Figure 2b**.

*Impedance Plethysmogram*

806 In addition to impedance spectroscopy, real-time bioimpedance was acquired simultaneously
807 with the EEG, using the MAX30001 AFE (Analog Devices, Inc.). The four-electrode
808 configuration shared electrodes with the EEG, with the two mastoid electrodes used for current
809 injection and the two in-ear electrodes for voltage sensing. A 96 μA current at 82 kHz was used
810 for excitation. Such high frequency excitation is effectively filtered by the ADS1299-4 and does
811 not corrupt the EEG signal. The MAX30001 built-in synchronous demodulator filtered and ADC
812 recovered the in-phase component of the sensed voltage and digitized it at 64 samples-per-
813 second (20-bit resolution). The resulting impedance measurements had a noise floor of 3 mΩ
814 rms (100 Ω load), enabling the detection of blood pulsations. A sample trace from a study
815 participant, derived from the device IPG is shown in **Figure 2d.** Note that the impedance shifts
816 measured in either the respiratory or cardiac frequency bands range between 50 to 150 mΩ. In
817 contrast, impedance shifts detected by EIS were at least an order of magnitude greater.
818
819 *Photoplethysmogram and Acceleration*
820 In-ear reflective photoplethysmogram (PPG) was measured with two miniature, fully-integrated
821 optical sensors MAXM86161 (Analog Devices, Inc.) located in each earpiece, facing the anterior
822 wall of the ear canal. One side was programmed to use green light (530 nm), while the other
823 used alternatively red (660 nm) and infrared (880 nm) lights. To achieve a tight synchronization
824 with EEG samples, the sensors ran at 1024 Hz for each color, and the most recent samples
825 available at the time of the EEG read were averaged, resulting in a 250 Hz output rate and a
826 phase variation <1 ms. A sample trace of the left (red) and right PPG (green) from a study
827 participant is provided in **Figure 2f.**
828
829 In-ear acceleration (X,Y,Z) was measured using two miniature MEMS Inertial Measurement Unit
830 (IMU) LSM6DSOX (ST Microelectronics, NV) located in each earpiece. Similar to the PPG, the

831 sensors were run at 833 Hz (each axis) and averaged to ensure tight time synchronization
832 between sensors. A noise floor of 1 mg rms enabled the resolution of cardiac/blood pulsations,
833 in addition to posture and activity. From these accelerometer data, a ballistocardiogram is
834 derived, as shown for a study participant in **Figure 2e**.
835
836 *Electrodes*
837 In-ear electrodes were laser-cut from silver sheets 100 microns thick and 99.9% purity. The
838 electrodes were 4.5 mm diameter plates with a 1 mm-wide stem. The electrodes were abraded
839 and sonicated in distilled water, dip-coated with Ag/AgCl ink provided by Creative Materials Inc
840 (SKU EXP 2653-138-1) and cured at 100°C for 60 min. Following curing, they were sintered at
841 427°C for 60 minutes under low-flow argon gas.
842
843 Once fabricated, all electrodes were characterized according to the ANSI/AAMI EC12 standard
844 for AC impedance[57], DC offset voltage, combined offset instability and internal noise, and bias
845 current tolerance (**Supplemental Table 7**). Pairs of electrodes were also connected to the
846 earpiece circuits with clip-on wires and tested on an agar phantom as described in the *Device*
847 *Testing* section.
848
849 *Electrical Impedance Spectroscopy Validation*
850 Measurement accuracy was first evaluated using a test fixture simulating the load and the four
851 electrodes (**Supplemental Figure 2**). The load was either purely resistive (*R*, 20-100 Ω), or
852 slightly reactive (*2R1C*, 20-100 Ω in parallel with 470 Ω and 22 nF in series) to mimic the brain
853 parenchyma. The electrodes were implemented as either (i) low impedance (270 Ω resistor in
854 series with a 1 kΩ resistor and 180 nF capacitor in parallel), or (ii) high impedance (620 Ω
855 resistor in series with a 3.3 kΩ resistor and 82 nF capacitor in parallel), in order to simulate the

frequency-dependence of typical Ag/AgCl electrodes, but also to ensure a minimal impedance at high frequencies. Two 10 Ω resistors were added between the electrodes connected to the same side of the load to simulate the tissue impedance between these electrodes as well. **Supplemental Table 8** describes the benchtop tests performed and **Supplemental Table 9** and **Supplemental Table 10** contain the results.

*Device Testing*

In addition to the EIS test fixture, stability and reproducibility of EIS measurements over twelve hours were evaluated with an agar phantom. A slab (5-10 mm thick) of conductive agar was first cast using a solution of 2.5% weight agar (Living Jin USA, Inc.), 0.64% weight NaCl (RND Center, Inc.) and distilled water. Electrodes (mastoids and earpieces for the final testing) were then coated with conductive gel (Electro-Gel, Electro-Cap International) to reduce the contact resistance, and placed on the agar slab in a pattern geometrically similar to the electrode location on the head. A 12-hour recording was performed, resulting in a total of 450 minutes of EEG recording, 159 EIS cycles and 160 electrode impedance checks. The results of a 12 hr agar phantom EEG test is shown in **Supplemental Figure 3.**

*Signal Processing – Parenchymal Resistance*

A python neuroprocessing pipeline developed by Applied Cognition performed the data analysis of the signals captured by the investigational device. The neuroprocessing pipeline runs in the Amazon Web Services cloud on a distributed architecture allowing for fast parallel execution of participant device readings.

An EIS scan by the investigational device measured impedances Z(ω) at 18 frequencies $f$ ($\omega = 2\pi f$) ranging from 1,000 Hz to 256,000 Hz and took 106 seconds. The frequencies were measured in the following permuted order for each scan (all in Hz): 2276, 102400, 1600, 64000,

4551, 51200, 12800, 85333, 3200, 25600, 1000, 32000, 6400, 8533, 128000, 204800, 256000. During the EIS scan, all other device sensors were powered off except the left-in-ear IMU that sampled at 1Hz to detect head motion and position. The EIS scans were duty-cycled throughout the recording period with 165 second neurophysiology scans that captured data from the other sensors: EEG, PPGs and IMUs. Four electrode impedance checks at 30Hz and lasting 7 seconds were performed during the neurophysiology scan and immediately preceding the EIS scan.

The Cole-Cole model[58-60] is commonly used to analyze EIS data. The analysis is based on the four parameters contained in the Cole equation $R_0$, $R_\infty$, α and τ.

$$Z(\omega) = R_\infty + \frac{R_0 - R_\infty}{1 + (j\omega\tau)^\alpha}$$

As the excitation frequency ω $(\omega = 2\pi f)$ increases to large values, the capacitive cell membranes are invisible to the excitation frequency and the impedance Z(ω) approaches $R_\infty$. The four excitation and response electrodes are positioned trans-cranially and at large ω measure total intracranial brain volume. As the excitation frequency ω decreases approaching DC values, the capacitive cell membranes prevent any transmembrane conduction and the impedance Z(ω) approaches $R_0$ the measure of electrical resistance through extracellular fluid.

The value of τ in the Cole-Cole model is the inverse of tissue characteristic frequency $2\pi f_c$. The Cole-Cole α describes the divergence of a measured dielectric dispersion from the ideal dispersion exhibited by a Debye type of dielectric relaxation, and is widely assumed to be related to a distribution of the relaxation times in the system involved. The value of α ranges from 0.5 to 1 with a value of 1 reducing the Cole-Cole model to the Debye model.

For each EIS scan, the four parameters were estimated using a non-linear least-squares fit (Python SciPy's least_squares) with the Trust Region Reflective algorithm that is a robust method suitable for large sparse problems with bounds. The α parameter was found to be close to one in the estimations and thereafter set to one, reducing the Cole-Cole model to the Debye model. The remaining three parameters were estimated with bounds of 0 to 90Ω for $R_0$, 0 to 70Ω for $R_\infty$ and bounds for $\tau = \frac{1}{2\pi f_c}$determined by requiring the characteristic frequency $f_c$ to lie between 16kHz and 160kHz. The parameter bounds where confirmed to encompass neurophysiological values in all participants by plotting all EIS scan resistance (real values of impedances Z(ω)) and reactance (imaginary values of impedance Z(ω)). Furthermore, no parameter solutions lay on a boundary for each scan across the range of dynamic impedance spectroscopy measurements for all participants.

Prior to fitting the Debye model to the EIS scan data, to compensate for stray capacitance, time delay effects from signal transmission and electrical components, the impedances Z from each scan were rotated by multiplying by the factor $e^{-j\omega T}$ with the value $T$ chosen so that the reactance at the highest frequency of the scan was zero[59]. This rotation was independently validated using EIS scans recorded on the benchtop tests using known impedance loads (**Supplemental Table 10**). The root-mean-squared-error (RMSE) of the Debye model fits to the benchtop tests (**Supplemental Table 8)** are reported in **Supplemental Table 11**.

Each EIS scan measures $R_P$ at a point in time and to evaluate glymphatic function the Debye model fits need to detect small changes in $R_P$. With the device time-multiplexing settings, the device completes approximately 84 scans over a 7-hour night of sleep. The statistical models require significance testing of the mean change in $R_P$ between sleep and wake, and testing significance of predictors of $R_P$ in linear mixed models. These tests depend on the SD of the

931 Debye model dispersion and the number of EIS scans (**Supplemental Table 12**). Details of
932 these analyses are found in **Supplemental 4**.
933
934 During EIS, tissue behaves as a linear, time-invariant and causal system allowing the use of
935 Kramers-Kronig relations to identify electrical impedance measures that are corrupted by
936 artifacts from motion, electrode impedances and other sources[31,32]. The Kramers-Kronig
937 transform allows the real part of the electrical impedance measure to be derived from the
938 imaginary part and vice versa[31]. These relations are used as validity tests for measured
939 spectrums. When the real and imaginary impedance measures do not satisfy the Kramers-
940 Kronig relation the measure is discarded. The Python PyEIS1.0.10 repository was used for
941 Kramers-Kronig impedance validation. The validation uses the method of Schönleber[32] to avoid
942 ambiguities in the linear Kramers-Kronig validity tests due to under- and over-fitting.
943
944 In addition to the Kramers-Kronig validity tests, EIS measures were discarded if for any of the
945 four electrode impedances, the difference across successive time measures exceeded 1kΩ or if
946 the EIS scan was collected during a wake interval on a participant randomized to sleep. The first
947 condition ensured that the electrode impedances were maintained within a narrow range during
948 the EIS scans and the second condition ensured that the EIS scans were representative of
949 sleep physiology for participants randomized to sleep.
950
951 *Signal Processing – Electroencephalography*
952 The raw EEG tracings from the device and the commercial PSG (Philips Respironics Alice 6
953 LDx Diagnostic Sleep System) were time-synchronized by time-aligning a 100-ms square pulse
954 generated by the device every 10 seconds and stored both in the device flash memory and in
955 the PSG recording through as an unused auxiliary analog input channel. Each raw tracing was
956 notch filtered at 60 Hz using a second-order infinite impulse response (IIR) notch digital filter

(Python SciPy *iirnotch*). The digital filter was applied to the signal forward and backward with a combined filter phase of zero (Python SciPy *filtfilt*). The signal was then bandpass filtered between 0.3 Hz and 50 Hz using a finite impulse response (FIR) filter with a Hann window (Python SciPy *firwin*). The length of the low-pass filter was 501 and the length of the high-pass filter was 2,401.

During the observation periods, participants were not allowed to touch devices that were plugged to power outlets. Other non-physiologic sources included excessive head motion that led to signal artifacts from the electrode-skin interface. Physiologic sources of signal artifact included electrooculogram, electrocardiogram and electromyogram. The signals where partitioned into time-aligned 30- second epochs. Epochs containing one or more peak-to-peak signal amplitude exceeding 350 μV or maximum power in the Welch power spectrum exceeding 1,000 $\mu V^2$/Hz were removed. In addition, the device left in-ear and right-in ear IMU signals were used to filter excessive motion by filtering epochs with peak-to-peak values on an x-, y-, or z-axis on either ear that exceeded 100 milli-g during sleep and 200 milli-g during wake.

The power spectral density of each 30-second epoch was computed using Welch's method[61] (Python Scipy *welch*) using 10-second segments and 50% overlap across successive segments. Relative power bands were computed for delta power (1-4 Hz), theta power (4-8 Hz), alpha power (8-12 Hz), sigma power (12-15 Hz), beta power (15-30 Hz) and low gamma power (30-50 Hz), each normalized to the total power in the power spectral density. Simpson integration of the power spectral density was used for computing the total power and respective band powers.

Hypnogram staging of each 30-second epoch used automated scoring (Python yasa 0.6.3 *SleepStaging*) trained and validated on 3,000 nights of data from the National Sleep Research

983 Resource[62]. The automated scoring uses a single EEG derivative and a single EOG channel.
984 For device hypnogram staging the single in-ear transcranial derivative was used and for the
985 commercial PSG, hypnogram staging using C3-A2 and C4-A1 derivatives were recorded
986 separately. The PSG left EOG channel was used for commercial PSG hypnogram staging. An
987 additional T3-T4 transcranial PSG derivative was used for hypnogram staging as another
988 comparison to the device's transcranial in-ear derivative. The internal agreement of commercial
989 PSG and agreement between investigational device-based EEG and PSG are presented in
990 **Supplemental Table 6**.
991
992 *Signal Processing – Heart Rate*

993 The photoplethysmography (PPG) left and right raw signals were bandpass filtered between 0.5
994 Hz and 10 Hz using a finite impulse response (FIR) filter with a Hann window (Python SciPy
995 *firwin*). Empirical mode decomposition was used to identify peaks in the raw signals (Python
996 emd 0.6.2) using a box-car rolling window of 100 observations[63]. Heart rate variability metrics
997 were computed after removing outliers, ectopic beats and interpolating missing values (Python
998 Aura-healthcare *hrvanalysis*). Both time-domain features (standard deviation (SD) of the inter-
999 beat-interval of normal sinus beats, *sdnn*) and frequency-domain features using the Lomb-
1000 Scargle periodogram [ref] (low-frequency signal power *lf* between 0.04-0.15 Hz considered a
1001 mixture of sympathetic and parasympathetic activity, high-frequency signal power *hf* between
1002 0.15-0.4 Hz representing beat-to-beat changes from parasympathetic vagal activity, and the
1003 low-frequency to high-frequency ratio (*lf-hf-ratio*) were computed[64].

1004 The device inertial-measurement units (IMU) were located inside the left and right ear canal and
1005 provided left and right cartesian coordinates of acceleration measured in milli-g where 1,000
1006 milli-g is the acceleration caused by earth's gravitational force. Each in-ear component from the
1007 device is uniquely and reproducibly oriented on account of the ellipsoidal shape of the human

ear-canal and the matching shape of the in-ear component. From this orientation, head position and motion (acceleration) were resolved from each set of IMU samples that included gross positions such as *supine*, *reclined*, *upright*, *left* and *right*.

### ***Clinical Study Design***

The Investigational Device was evaluated in two studies, a Benchmarking Study conducted in The Villages community in Florida in partnership with the UF Health PHRC, and a Replication Study conducted at the University of Washington in Seattle. These studies were reviewed and approved by University of Florida Institutional Review Board (IRB No. 202201364) and Western Institutional Review Board (IRB No. 20225818), respectively. Written informed consent was obtained from all study participants during a screening visit, prior to any study activities.

#### *Participant Recruitment*

Following distribution of study flyers in public-facing locations in senior recreation and/or local medical centers, the Benchmarking Study enrolled 34 healthy participants 56-66 years of age and the Replication Study enrolled 14 healthy participants 49-63 years of age. Participants were cognitively intact and had no history of clinical depression, confirmed during screening using the Montreal Cognitive Assessment (MOCA) and Geriatric Depression Scale (GDS). Other exclusion criteria included a history of diabetes, hypertension, coronary artery disease, pulmonary disease, neurological disease, or anxiety. Participants planning travel to alternate time zones within two weeks of study participation were also excluded. Consolidated Standards of Reporting Trials (CONSORT) diagram for the Benchmarking Study and Replication Study is provided in **Figure 3** (bottom), and participant exclusions are detailed in the Results section. Demographic data including age, sex, APOE4 allele status, MOCA and GDS for the Benchmarking Study, Replication Study, and Combined Studies are provided in **Supplemental Table 1.**

1034

1035 *Study Protocol*

1036 As shown in the study schematic (**Figure 3**, top), this is a cross-over study in which participants
1037 took part in two overnight study visits, one undergoing normal sleep and the other undergoing
1038 overnight sleep deprivation, at a 2-4 week interval. Each overnight study visit consisted of three
1039 study periods beginning at 1900 hrs, 0700 hrs, 1330 hrs separated by two intervals – an
1040 overnight interval (2300-0630 hrs), and a morning interval (0800-1130 hrs).

1041

1042 <u>Benchmarking Study:</u> Beginning with arrival to the study suite at 1900, participants underwent a
1043 blood draw for APOE genotyping and assessment of amyloid β and tau biomarkers ($A\beta_{1-40}$, $A\beta_{1-}$
1044 $_{42}$, phospho-tau181, phosho-tau217, non-phospho-tau181, non-phospho-tau217; $C_2N$
1045 Diagnostics[65-67]) and 60 min of non-contrast magnetic resonance imaging (MRI) scanning
1046 (sequences detailed below). On completion, participants were instrumented for commercial
1047 polysomnography (PSG, Philips Respironics Alice 6 LDx Diagnostic Sleep System) that
1048 included a 10-20 EEG montage with electro-oculogram (EOG) and submental electromyogram
1049 (EMG). Electrode impedances were required to be below 5 kΩ. Participants were last
1050 instrumented with the Investigational Device, and device electrode impedances required to be
1051 below 5 kΩ.

1052

1053 The Overnight interval lasted from 2300-0630 hrs the following morning. To support study
1054 planning, participants were randomized to undergo either normal sleep or sleep deprivation for
1055 their initial overnight visit following completion of their informed consent, however this
1056 information was not shared with the participants. To reduce likelihood of preparation bias on the
1057 part of participants (i.e. altering sleep schedules or taking naps in anticipation of sleep
1058 deprivation visits) participants were not informed of their initial visit assignment until 4pm the

1059 day of their arrival. Both PSG and Investigational Device recordings took place continuously
1060 throughout the Overnight interval. Throughout the overnight period, sleep-assigned participants
1061 were allowed to sleep normally without interruption. Participants assigned to the sleep
1062 deprivation were monitored by study staff to ensure adherence to the sleep deprivation protocol.
1063
1064 Between 0700-0745 hrs the next morning, all participants were administered a cognitive battery
1065 that included the 5-minute psychomotor vigilance test for sustained attention[68,69], symbol-digit
1066 modality test of processing speed, trail making test part A and part B for assessing executive
1067 function[70], and digit span forward test of working memory[71]. Following the cognitive battery,
1068 participants underwent a blood draw for amyloid β and tau biomarkers and a second non-
1069 contrast MRI scanning session (denoted $T_0$ in Results section). Immediately following the
1070 second non-contrast MRI scan, participants underwent intravenous gadolinium-based contrast
1071 agent (GBCA) injection (Gadavist, 0.1 mmol/kg), followed by T1- and T2-weighted contrast-
1072 enhanced MRI scans 7-10 min after GBCA injection (denoted $T_{10}$ in Results section).
1073
1074 Participants were escorted back to the study suite where they were re-instrumented with the
1075 commercial PSG and the Investigational Device. The Morning Interval ran from 0800 to 1130.
1076 Participants who assigned to the sleep condition in the Overnight Interval were required to
1077 remain awake and were monitored by study staff to ensure adherence; those assigned to the
1078 sleep deprivation condition in the Overnight were allowed to sleep. During this interval both the
1079 PSG and Interventional Device recorded data. The third assessment period commenced at the
1080 end of the Morning Interval. Participants underwent a final blood draw for amyloid β and tau
1081 biomarker assessment and then had a third MRI scanning session, including non-contrast
1082 sequences and T1- and T2-weighted contrast-enhanced sequences at approximately 4 hrs
1083 post-GBCA injection (denoted $T_{240}$ in Results section).

1084

1085 Replication Study: The Replication protocol was an abridged version of the Benchmarking
1086 protocol. The inclusion/exclusion criteria were identical to the Benchmarking study except for
1087 the lower age cut-off. Participants were similarly randomized to a night of sleep or a night of
1088 sleep deprivation on their first visit, with a crossover to the alternative sleep/sleep deprivation
1089 assignment on their second visit. The protocol for the Replication Study was identical to that of
1090 the Benchmarking Study excepting that 1) Participants did not undergo commercial PSG, sleep
1091 was assessed by Investigational Device EEG; 2) Participant sleep deprivation adherence in the
1092 Overnight Interval was assessed retrospectively using the sleep EEG; 3) The cognitive battery
1093 did not include the digits forward working memory test; 4) Participants underwent only non-
1094 contrast, and not contrast-enhanced MRI.

1095

1096 Cognitive Assessments: The 5-minute PVT from Texas A&M University System CSE[72] and
1097 digits forward recall from Cambridge Cognition[71] were administered on an iPad. The paper-
1098 based SDMT from Western Psychological Services[73], the TMT A and TMT B[74], were
1099 administered by a clinical coordinator trained in administering these tests. The cognitive battery
1100 was administered in a quiet room with minimal distractions on the morning following sleep/wake
1101 and prior to the neuroimaging and phlebotomy. The administration of each test was preceded by
1102 the corresponding practice test. We have included a description of these tests within the overall
1103 protocol for completeness. The results of these cognitive tests, and their relationship to
1104 Investigational Device outputs, sleep parameters, fluid biomarkers, and MRI measures of
1105 glymphatic function will be reported elsewhere.

1106

1107 Plasma Biomarkers: The APOE genotyping, amyloid β and tau plasma biomarkers were
1108 analyzed using mass spectrometry by $C_2N$ Diagnostics[75]. The sample collection procedure was
1109 provided by $C_2N$ Diagnostics. Venipuncture and blood draw from the antecubital fossa were

1110 performed using a 22-gauge butterfly needle to minimize red blood cell hemolysis. A total of 10
1111 ml of blood was drawn into a $K_2$ EDTA Vacutainer. The blood was centrifuged for 15 min using a
1112 swinging bucket rotor at 500-700 x g with the brake on. Immediately after centrifugation, four 1.0
1113 mL plasma samples were aliquoted into four Sarstedt 2.0 ml Micro Tube without disrupting the
1114 plasma/cell interface when transferring plasma. A calibrated air-displacement hand-held pipette
1115 with a polypropylene pipette tip was used. After aliquoting plasma into the Sarstedt Micro
1116 Tubes, the tubes were immediately capped and frozen at -40$^{o}$C. When the tubes were ready to
1117 be shipped to $C_2$N Diagnostics, they were packed into a plastic zip-lock bag with plenty of dry
1118 ice, placed in an absorbent towel and cryobox, and express couriered to $C_2$N Diagnostics
1119 priority overnight. In the present report, we utilize APOE4 allele status as a covariate in our
1120 analysis, and we have included a description of plasma biomarker assessment within the overall
1121 protocol for completeness. However, the fluid biomarker levels, and their relationship to
1122 Investigational Device outputs, sleep parameters, cognitive tests, and MRI measures of will be
1123 reported elsewhere.
1124
1125 *Magnetic Resonance Imaging Approach*
1126 MRI scanning at The Villages site was conducted on a 3T Siemens Vida system at Lake
1127 Medical Imaging, while scanning at the University of Washington site was conducted on a 3T
1128 Philips Ingenia Elition X at the Diagnostic Imaging Sciences Center. In the present report, to
1129 define the relationship between brain $R_P$ and glymphatic function, we utilize CE-MRI from
1130 Benchmarking Study participants following the overnight sleep condition. We have included a
1131 description of the other MRI-based approaches within the overall protocol for completeness.
1132 However, the relationship between these different MRI measures of glymphatic function,
1133 Investigational Device outputs, sleep parameters, cognitive tests, and fluid biomarker levels will
1134 be reported elsewhere.
1135

1136 Contrast-Enhanced MRI: Contrast-enhanced MRI involves intravenous administration of a
1137 Gadolinium chelate that shortens T1, T2, and T2* relaxation parameters of the tissue it
1138 traverses through. Specifically, in this study, shortening of the T1 relaxation parameter
1139 enhances MRI signal that is proportional to the amount of Gadolinium and its characteristic
1140 relaxivity. Gadolinium passes quickly through the cerebral and peripheral vasculature within the
1141 first 5-30 minutes. A fraction of the contrast enters the CSF and ISF[14,15] over many hours and
1142 finally almost 99% of the contrast exits the body by renal clearance. The passage of intravenous
1143 GBCA from the vasculature to the CSF and ISF was measured in terms of a delayed signal
1144 enhancement at approximately 4 hours after administration. Two prior studies have shown that
1145 delayed enhancement following contrast injection between 3 and 6 hours is indicative of solute
1146 (in this case, GBCA) transport via the CSF-ISF glymphatic exchange[14,15]. At the Villages®, we
1147 performed 3D T1-weighted magnetization-prepared rapid acquisition with gradient echo
1148 (MPRAGE) with TR/TI/TE = 2300/900/2 ms, resolution = $1\times1\times1$ mm$^3$, field-of-view =
1149 $256\times256\times208$ mm$^3$, total acquisition time = 5:12 min before contrast injection. The post-contrast
1150 MRI image ($T_{10}$) was acquired approximated 7-10 minutes after contrast injection and its
1151 acquisition was identical to the pre-contrast image. A second post-contrast scan was acquired
1152 about 4 hours ($T_{240}$) later using identical imaging parameters.
1153
1154 Structural MRI: Structural T1 MRI was used for classifying the brain tissue into lobar gray
1155 matter, lobar white matter, and CSF as well as for segmenting regions-of-interests including the
1156 hippocampus, sagittal sinus, internal carotid arteries, lateral ventricle, and subarachnoid space.
1157 The T1 images were also used for registration purposes for all other imaging modalities. The T1
1158 images were used for determining PVS morphometry[76,77]. Scanning parameters for the
1159 Benchmarking Study are identical to the contrast-enhanced MRI. Scanning parameters for the
1160 Replication Study were TR/TI/TE = 12/1000/4.5 ms, resolution = $0.8\times0.8\times0.8$ mm$^3$, field-of-view

1161 = 256×240×166 $mm^3$, total acquisition time = 5:24 min. Since inclusion of T2 MRI significantly
1162 improves PVS detection, a T2 MRI with TR/TE = 3200/561 ms, resolution = 0.8×0.8×0.8 $mm^3$,
1163 field-of-view = 256×240×166 $mm^3$, total acquisition time = 4:32 min was also added.
1164
1165 Intravoxel Incoherent Motion MRI: Intravoxel incoherent motion (IVIM) MRI is a multi-shell
1166 diffusion imaging approach to measure water movement at different scales of distance and time.
1167 Glymphatic transport includes movement of CSF in the subarachnoid space and the interstitium
1168 at a slow speed (~1 mm/s) over large distances (~100-200 um)[1,30,40]. This perivascular
1169 movement of CSF through the subarachnoid compartment is upstream of its exchange with the
1170 ISF along the penetrating intraparenchymal vasculature and hence could serve as an important
1171 correlate of glymphatic function[78]. The imaging parameters for the Benchmarking Study were:
1172 TR/TE = 5500/124 ms, resolution = 1×1×5 $mm^3$, field-of-view = 250×250×150 $mm^3$, parallel
1173 imaging factor = 2, multi-band factor = 3, fat suppression with Spectral Presaturation with
1174 Inversion Recovery (SPIR), b values = 0, 50, 100, 150, 200, 250, 300, 350, 400, 500, 700, 800,
1175 and1000 s/$mm^2$, and total acquisition time = 7:01 min. The b = 0 s/$mm^2$ was acquired with
1176 reverse phase encoding to correct for field distortions. The imaging parameters for the
1177 Replication Study were TR/TE = 2978/90 ms, resolution = 1×1×5 $mm^3$, parallel imaging factor =
1178 2.2, field-of-view = 230×196×115 $mm^3$, fat suppression with SPIR, b values = 0,
1179 10,40,80,100,150,200, 300,500,700, 800, 900,1000 s/$mm^2$, and total acquisition time = 8:08
1180 min. A Split echo (SPLICE) acquisition was used to eliminate the need for distortion correction.
1181
1182 Multi-Echo, Multi-Delay Arterial Spin Labeling (ASL) MRI: Multi-echo, multi-delay ASL measures
1183 perfusion and time for exchange of water across the endothelium. This time metric is dependent
1184 on perfusion, endothelial permeability, and the glial vascular unit including the AQP4 water
1185 channels that are critical to the perivascular CSF-ISF exchange[78,79]. This protocol was

implemented only for the Replication Study as a Hadamard-encoded ASL acquisition, TR/TE = 5000 ms, resolution = 1×1×5 $mm^3$, field-of-view = 230×196×115 $mm^3$, post labeling delay = 650, 950,1210,1510,2083,2383 ms with background suppression, label duration = 3400 ms, and TE = 0,40,80, 120 ms. Total acquisition time = 12:40 min. A conventional arterial spin labeling (ASL) protocol was implemented in the Benchmarking Study due to the lack of availability of the multi-echo component. The parameters were: TR/TE = 4420/22 ms, resolution = 1.7×1.7×4 $mm^3$, field-of-view = 220×220×96 $mm^3$, post labeling delay = 500, 900,1000,1100,1200,1400,1600,1800, label duration = 1800 ms. Total acquisition time = 2:37 min. The sequence was acquired twice. A reference M0 images was acquired in both studies with identical parameters but without background suppression or labeling.

<u>Fast Functional MRI:</u> A sub-second functional MRI sequence was implemented to separate and regress physiological noise (cardiac and respiratory signals) as well as to capture slow CSF oscillations in the ventricles[80]. The protocol for the Benchmarking Study was TR/TE = 400-500/30 ms, resolution = 3.6×3.6×3.6 $mm^3$, flip angle = 70°, multi-band factor = 4, field-of-view = 230×2430×101 $mm^3$, fat suppression, no. of volumes = 365 using SPIR, total acquisition time = 2:37 min. Heart rate and respiration were monitored using the BIOPAC MR160 and synchronized with MRI acquisition. The Replication Study used a gradient-echo, echo planar imaging sequence with TR/TE = 400-500/30 ms, resolution = 3×3×4 $mm^3$, flip angle = 42°, multi-band factor = 6, field-of-view = 240×240×123 $mm^3$, slice gap = 0.4 mm, fat suppression using SPIR, no. of volumes = 450, total acquisition time = 3:00 min. Two single volume, spin echo acquisitions were also acquired with opposite phase encoding to allow for distortion correction. Heart rate and respiration were monitored using the sensors built into the Philips scanner and synchronized with MRI acquisition. Glymphatic CSF-ISF exchange is at least partly driven by vasomotion, which may be reflected by periodic motion in the CSF spaces. This CSF motion

1211 correlates well with sleep stages, with power of the slow CSF oscillation increasing from
1212 wakefulness to the N1 and finally to the N2 stage[80].
1213
1214 Phase-Contrast MRI: The phase contrast MRI is used to quantify CSF efflux from the Aqueduct
1215 of Sylvius. The peristaltic motion of CSF at the Aqueduct is measured by gating the MRI signal
1216 to the participants and calculating the CSF motion into and out of the brain over a cardiac
1217 signal. Variations in CSF efflux velocity appear to follow the cardiac and respiratory signals and
1218 may impact glymphatic CSF-ISF exchange. The Benchmarking Study protocol for this MRI was
1219 the following: a single slice acquisition perpendicular to the Aqueduct of Sylvius, TR/TE = 21/6.6
1220 ms, resolution = $30.6\times0.6\times6$ $mm^3$, flip angle = 10°, 40 phases per cardiac cycle, and velocity
1221 encoding for 12 cm/s, total acquisition time: 2:00 min. The Replication Study protocol included
1222 the following: a single-slice acquisition perpendicular to the Aqueduct of Sylvius, TR/TE = 12/7.9
1223 ms, resolution = $30.6\times0.6\times4$ $mm^3$, flip angle = 10°, 15 phases per cardiac cycle, and velocity
1224 encoding for 12 cm/s, total acquisition time: 2:02 min
1225
1226 *Statistical Approach*
1227 The Benchmarking study was designed to have 80% power at a significance level of 5% to
1228 detect a low-to-moderate correlation $r$ ($r$=0.5) between the device measurements and CE-MRI
1229 measurement of glymphatic function. The Replication study was designed to have 80% power
1230 at a significance level of 20% to detect a low-to-moderate correlation $r$ ($r$=0.5) between the
1231 device measurements and non-contrast MRI measurement of glymphatic function and to detect
1232 overnight sleep/wake differences in brain parenchymal resistance.
1233
1234 The parenchymal resistances $R_P$ computed from each EIS scan from the device were
1235 normalized to the sleep/wake onset values to allow comparison across visits and participants.

To reduce measurement variability of the sleep/wake onset value, the value was inferred from a linear regression to the initial $R_P$ values. The overnight change in $R_P$ per participant visit was taken as the average of the normalized values for that visit. For example, a value of 1 indicated that there was no overnight change from the onset value and a value of 0.8 indicated a 20% overnight reduction from onset. A Student's T-test group comparison between sleep/wake visits, group mean and SD were calculated.

Contrast-enhanced MRI of sleep-related glymphatic function was analyzed using a random intercept linear mixed effect model (R, lme in the lmne package). Glymphatic function was defined by measuring brain parenchymal contrast enhancement, the % change in T1-weighted signal intensity between 10-240 min post-GBCA injection (100% * $(T_{240}-T_{10})/T_0$) at each of eight regions of interest (ROIs): frontal cortical gray and white matter, parietal cortical gray and white matter, temporal cortical gray and white matter, and occipital gray and white matter. Only sleep visits were analyzed leading to a one level of grouping, the eight ROIs, for the participant sleep visit. All models included regressors in the mixed model for the $T_{10}$-$T_{240}$ change in blood signal within the internal carotid artery, and the $T_{10}$-$T_{240}$ change in CSF signal within the cerebral lateral ventricles to compensate for the influence of vascular and CSF contrast on parenchymal enhancement. Potentially confounding biological variables age, gender, and APOE ε4 status were also included in all models.

To evaluate different sleep-related contributions to glymphatic function, overnight changes from sleep onset for each of the four recorded EEG relative band powers (delta, theta, alpha, beta) and for HR were computed. The recorded values were normalized to their respective value at sleep onset and a single statistic, the average of the overnight normalized values, computed per participant visit. The four hypnogram sleep stages (N1, N2, N3, REM) and WASO were each summed into single total sleep stage durations and total WASO duration per participant visit.

The device $R_P$ normalization and averaging has been previously described. Models were run separately for each of the four EEG relative band powers (delta, theta, alpha, beta), for each of the four hypnogram sleep stages (N1, N2, N3, REM), for WASO, for HR and for device $R_P$. Two full models were then fit to the data, with the EEG band power and the hypnogram sleep stages separated into distinct models because of collinearity across those predictors. The variance inflation factor (R 'vif' function from the 'car' package) was used to test for predictor collinearity using a threshold of 5. The EEG powerbands included were limited to delta, theta and beta because of collinearity among the four relative band powers. HR and the device $R_P$ were included in both full models. Each full model was reduced to a selected model using backward elimination of predictors with a threshold Wald's p-value of 0.05.

Model selection stability, or robustness of the selected model to perturbations in the dataset, was tested using resampling-based multi-model inference[29]. The dataset was bootstrapped resampled with replacement to generate 500 bootstrapped datasets. For each of these datasets the two full models were estimated and reduced to a selected model using backward elimination. The bootstrap inclusion frequency (the percent of bootstrap datasets that included the predictor), the RMSD ratio (the RMSD of the predictor bootstrap estimate divided by the standard error of that coefficient in the full model and expressing the variance inflation or deflation caused by variable selection), the relative conditional bias (quantifying the variable-selection-induced bias to expect if a predictor is selected) and the bootstrap median of each predictor coefficient were reported.

The analyses of device $R_P$ values with EEG band powers, heart rate and hypnogram staging were performed on the overnight sleep recordings. Analyses were grouped into REM sleep and NREM sleep (N1, N2 and N3). The device resistances were computed repeatedly throughout the night from each EIS scan. During sleep recordings, these data were non-stationary. After

normalization to sleep onset as previously described, first-order differences $\Delta R_P$ and $\Delta X$ for X one of the EEG band powers or HR were incorporated into individual random intercept linear mixed models to evaluate their relationship. Threshold regression models were used in the linear mixed model. A custom estimation procedure described in **Supplemental Information** was used to jointly estimate the threshold regression for the full positive and negative range of the predictors. The hinge threshold model was analytically reduced to estimation by linear regression which allowed it to be used in a random intercepts linear mixed effects regression model. The autocorrelation function and augmented Dickey Fuller tests were used to confirm stationarity of the differenced variables $\Delta R_P$ and $\Delta X$ and also of the fitted model residuals (R, acf and adf functions).

In addition to the analyses of $\Delta R_P$ and $\Delta X$ for X one of the EEG powerbands or HR during REM sleep and NREM sleep, these were analyzed at hypnogram transitions NREM to REM, REM to NREM, sleep to wake and wake to sleep. The analysis was similar, using threshold regression models in a random intercept mixed linear model.

Univariate outliers were trimmed at the 0.5 and 99.5 percentile. For multivariate analysis, the Mahalonobis distance was computed and outliers trimmed at the 0.5 and 99.5 percentile of the Mahalonobis distance. All regressions were adjusted for potential confounding effects of age, sex and APOE genotype. All tests were considered significant at a 5% level if the 95% confidence interval (CI) did not contain the null hypothesis. All statistical analyses were performed in R version 4.2.1 (2022-06-23) or Graphpad Prism 8.0.0.

We reported the pooled findings of the Benchmarking and Replication study for both the investigational device transcranial resistance measurements and EEG parameters.

## SUPPLEMENTAL INFORMATION

### *Supplemental 1: Analysis of device EEG and commercial polysomnography*

The single derivative device EEG was validated against the commercial PSG (Philips Respironics Alice 6 LDx Diagnostic Sleep System) in participants that underwent concurrent device and PSG sleep recording as part of the Benchmark study. Both hypnogram sleep staging and sleep parameters were validated using a confusion matrix between the device prediction and the PSG prediction both per participant and pooled across participants. Prediction metrics computed included sensitivity, specificity, precision, accuracy and F1 score. The device EEG with EOM and the PSG C3-A2, C4-A1 derivatives were individually input into the automated hypnogram scoring (Python yasa 0.6.3 *SleepStaging*). Manual scoring of the PSG by a sleep physician (YC) was used as the gold-standard. The results of these comparisons are provided in **Supplemental Table 6.**

### *Supplemental 2: Threshold regression model and estimation*

Threshold regression models were fit on data that spanned the full positive and negative range of abscissa values. These models are defined by a positive turning point $t_p \geq 0$ where for $x \geq t_p$ the regression line goes from $f(x) = 0$ to $f(x) = m_p(x - t_p)$ and a negative turning point $t_n \leq 0$ where for $x \leq t_n$ the regression line goes from $f(x) = 0$ to $f(x) = m_n(x - t_n)$. These models can be reduced to linear regression. First transform the data $(x, y) \rightarrow (w, y)$ were

$$w = \begin{cases} x - t_n \; if \; x \leq t_n \\ 0 \; if \; t_n < x < t_p \\ r(x - t_p) if \; x \geq t_p \end{cases}$$

For values of $t_p$, $t_n$ and $r$, a least squares estimator can be used to fit a linear model to the transformed data values $(w, y)$. With $r = \frac{m_n}{m_p}$, the transformed data is linear, through the origin and has slope $m_n$. When $r = 1$ both slopes are identical; for $r \neq 1$ the positive half-space slope equals the regression estimate multiplied by $r$. Hence, for $r < 1$ the positive half-space slope is

less than the negative half-space slope and for $r > 1$ the positive half-space slope is greater than the negative half-space slope.

The linear fit was estimated using an F-statistics, the ratio of the explained variance (due to the model) and the unexplained variance (residuals). Grid search over the parameter space $t_p$, $t_n$ and $r$ was carried out and the values that minimized the mean sum of squared residuals (and hence maximized the F-statistic) was reported[81]. To avoid edge effects, $t_p$ and $t_n$ were set to ±*1.5* standard deviations[82]. Random intercept linear mixed models were similarly fit to the transformed data and grid search used to solve for the parameters that minimized the mean sum of squared residuals for the fixed effects. The autocorrelation function was used to confirm no residual autocorrelation following model estimation and fit.

***Supplemental 3: Physiological basis for electrical impedance spectroscopy change with glymphatic function.***

In normal adult men (women) between the ages of 60-86 years, the GM, WM and total intracranial volumes (TIV) are 614.3 ± 60.1 (562.6 ± 50.1 ml), 534.0 ± 57.2 ml (476.6 ± 44.7 ml) and 1603.0 ± 133.0 ml (1425.9 ± 109.0 ml)[83]. Average adult cerebral blood flow (CBF) is approximately 750 ml/min or 12.5 ml/sec. Assuming HR of 60 bpm, 12.5 ml of blood injected into the brain causes an approximate 50 mΩ decrease in the device IPG sampled at 80 kHz (see for example **Figure 2d**, IPG-Impedance Plethysmograph data taken from a female study participant). At 80 kHz, EIS measures the extracellular compartment and most of the intracellular compartment. Thus, the 12.5 ml increase in blood volume, representing a 12.5/1425.9 = 0.88% change in TIV, would be measured as a 50 mΩ decrease in resistance by EIS.

At low frequencies, EIS measures changes in extracellular volume. The interstitial cortical volume fraction α in awake rodents has been shown to be 14.1% and in sleeping rodents 23.4% whereas the tortuosity λ of the interstitial space remained unchanged across sleep and wake[2,84]. This suggests that in rodents, the sleep-induced volume expansion of the interstitial space occurs from a change in the cross-sectional area and not length. This is noteworthy because resistance of a conductor is proportional to $\frac{l}{A}$ where $l$ is the length and $A$ the cross-sectional area. Therefore, the increase in interstitial space fluid with glymphatic function will increase the cross-sectional area of the interstitial space channels and proportionally decrease the transcranial electrical resistance. In humans, the measurements range from 15-20%[85] but changes with sleep/wake have not been assessed. Using the rodent data as a proxy to what we might expect in humans, we would expect a 66% increase in interstitial volume with sleep to occur from of a 66% increase in cross-sectional area of the interstitial channels. The remaining extracellular compartment volumes contributing to the resistance at low EIS frequencies are CSF and blood plasma that occupy a total volume comparable to the awake interstitial volume. Therefore, the net extracellular compartment volume increase, or effective cross-sectional area increase, with sleep is 33%. Using the IPG relationship between fluid volume change and transcranial impedance, a 0.88% increase in fluid volume was measured as a 50 mΩ decrease in transcranial electrical resistance implying that a 33% volume increase would be measured as an 1875 mΩ decrease. This analysis uses the conclusion that the interstitial volume increase of glymphatic function is an increase in the interstitial channel cross-sectional area and similarly the assumption that the intravascular volume increase of cardiac output is from an increase in the intravascular cross-sectional area. The preceding analysis assumed a 66% increase in interstitial volume fraction as seen in rodents. Assuming a smaller 25% volume fraction increase

and using the same analysis, we would expect a 710 mΩ decrease in transcranial resistance with sleep.

***Supplemental 4: Benchtop and agar phantom characterization of electrodes and device.*** Electrodes were characterized according to the ANSI/AAMI EC12 standard for AC impedance, DC offset voltage, combined offset instability and internal noise, and bias current tolerance[57]. Defibrillation overload recovery was not tested as it is not relevant to the present application. Pairs of electrodes were immersed in a 140 mM NaCl solution, facing each other and separated by 3-4 mm. AC impedance at 10 Hz was measured using a multifunction DAQ module (Analog Discover 2, Digilent) configured for 2-point impedance measurement. An excitation voltage of 100 millivolts peak-to-peak (mVpp) and a 10 kΩ series resistor guaranteed a maximum current of 10 microamps peak-to-peak (μApp). DC offset voltage was measured with a Fluke 87V multimeter. Offset instability and internal noise were measured over five minutes using a 24-bit digitizer module (ADS1299EVM, Texas Instruments, 67 nV resolution) sampling at 2000 samples per second, calibrated using a Keysight EDU33212A Signal Generator. Recorded data was subsequently filtered with a 0.15-100 Hz first order bandpass (simulating EC12 filtering) or the 0.3-50 Hz EEG bandpass filter described in **Signal Processing – Electroencephalography**. Peak-to-peak values over the 5-minute period are reported. Bias current tolerance was measured with a multifunction DAQ module using its 14-bit digitizer (0.32 mV resolution) as data logger (sampling every 10 seconds for 8 hours), and its power supply to apply 200 nA DC across the pair of electrodes (2 V across a 10 MΩ resistor in series). The maximum voltage deviation relative to the initial offset voltage before current application is reported. All results are found in **Supplemental Table 7**.

Benchtop validation of the investigational device EIS compared the measured to the theoretical resistance and reactance at each frequency on a circuit model of brain parenchymal impedance

(the load) with separate models for each of the four electrode impedances. The circuit diagram for these benchtop measurements is shown in **Supplemental Figure 2.** The load was modelled using 2R1C parallel circuit and the four electrode-skin interfaces were modeled by individual 2R1C circuits with a charge transfer resistance in parallel to a double layer capacitance that was in series with a resistor embodying the electrolyte and stratum corneum resistance. The resistance and capacitance values for the load were based on observed participant resistance and reactance over the EIS frequencies. Two sets of parameters for the electrode impedance models were used, a low-impedance model and a high-impedance model. These were selected to cover the observed range of subject electrode impedances over the range of EIS frequencies. The parameters for the complete set of benchtop tests are found in **Supplemental Table 8** and included (i) calibration measurements of purely resistive loads, (ii) calibration of a 2R1C load varying the parallel resistor $R_s$ to simulate changes in the interstitial space resistance, and (iii) calibration of a fixed 2R1C load while varying the electrode impedances at each electrode between low and high impedance settings to test the sensitivity to expected variations during use. The absolute error between the measured and theoretical resistance and reactance for the benchtop tests are reported in **Supplemental Table 9** and in **Supplemental Table 10**, respectively. The measured impedances reported were rotated by multiplying by the factor $e^{-j\omega T}$ with the value $T$ chosen so that the reactance at 256kHz was zero[59]. The absolute error of the resistance reveals a systematic positive bias implicating contributions to the resistance in the device or benchtop setup that were not fully compensated by the device calibration. For the measurements of the 2R1C benchtop tests, the resistance bias is 0.278 Ω and the bias un-adjusted and adjusted RMSE are 0.321 Ω and 0.144 Ω, respectively. The reactance did not show a systematic bias. The RMSE of the reactance for the 2R1C benchtop tests is 0.128 Ω. Because we are interested in the dispersion of the resistance over frequencies, or the difference between the resistance at a low frequency and at a high frequency, the bias cancels out. Using the signal processing pipeline to fit the Debye model, **Supplemental Table 11** reports the

dispersion prediction error from theoretical value at each frequency relative to 128 kHz. Reported values are for the 2R1C electrode impedance sensitivity tests. The 1 kHz minus 128kHz dispersion is representative of the parenchymal resistance $R_P$ computed from the difference between the extrapolated DC resistance and the infinite frequency resistance. This dispersion had an RMSE of 0.147 Ω approaching the bias-adjusted RMSE of the 2R1C benchtop tests in **Supplemental Table 9**, and represents a 3.1% measurement error in the theoretical dispersion value of 4.766 Ω.

The device EIS showed the accuracy needed to reliably measure a single $R_P$ value but to evaluate glymphatic function it needs to detect changes in $R_P$. These changes are small by comparison to the absolute value of $R_P$. As discussed, the overnight decrease ranges between 500 mΩ and 2000 mΩ. With the current time-multiplexing settings, the device completes approximately 84 scans over a 7-hour night of sleep, or 6 to 23 mΩ average decrease between scans. The statistical models used in the analysis of the Benchmarking Study and Regression Study required significance testing of the mean change in $R_P$ between sleep and wake, and testing significance of predictors of $R_P$ in linear mixed models. These tests depend on the SD of the Debye model dispersion estimate which for the electrode impedance sensitivity tests was 0.113 Ω, slightly less than the bias-adjusted RMSE. **Supplemental Table 12** shows that the minimum change in $R_P$ with 25 and 100 EIS scans that is statistically significant is 44 mΩ and 22 mΩ, respectively. Note that during sleep, $R_P$ decreases with glymphatic function and therefore each measurement arises from a distribution with a different mean but the same SD $\sigma$. Using the linearity of expectation and statistical independence of each $R_P$ measurement, the standard error of the mean of $R_P$ is $\frac{\sigma}{\sqrt{n}}$ for $n$ samples. Using the Fisher transform[86] to solve for the minimum significant correlation detectable at a given sample size, **Supplemental Table 11** reports that weak to moderate correlations of $R_P$ with predictors will be significant at 100 and 25

EIS scans, respectively. These estimates are optimistic since not all sources of error are accounted by the electrode impedance sensitivity tests.

Agar phantom testing over 12 hours was used as a final quality check for each fully assembled device. These tests measured the device combined noise level from the electronics, electrochemical interfaces between the electrodes, EEG gel and agar. **Supplemental Figure 3** shows the device periodogram, EEG recording and power spectral density from an agar phantom test.

**Data availability**

The data supporting the results in this study are available from the corresponding author with Institutional Review Board approval and Data Use Agreement permitting non-commercial use of data for independent validation, publication and sharing of new findings.

**Code availability**

Code used for the analysis and to produce figures are available upon reasonable request to the corresponding author.

1484 **Supplemental Table 1. Demographic, genetic and psychometric results of the**
1485 **Benchmarking Study, Replication Study and Combined Study.**
1486

| | **Benchmarking Study** | **Replication Study** | **Combined Study** |
|---|---|---|---|
| **N** | 30 | 14 | 44 |
| **Age ± SD (Range)** | 61.8 ± 2.7 (56, 66) | 55.6 ± 4.6 (49, 63)* | 59.8 ± 4.4 (49, 66) |
| **Female (Male)** | 14 (16) | 7 (7) | 21 (23) |
| **APOEe4 (not APOEe4)** | 8 (22) | 5 (9) | 13 (31) |
| **MoCA ± SD (Range)** | 27.8 ± 1.1 (26, 30) | 28.6 ± 1.2 (26, 30) | 28.1 ± 1.2 (26, 30) |
| **GDS ± SD (Range)** | 0.7 ± 1.1 (0, 4) | 0.6 ± 1.2 (0, 4) | 0.7 ± 1.1 (0, 4) |

1487 Montreal Cognitive Assessment, MoCA; Geriatric Depression Scale, GDS. *P<0.001
1488 Benchmarking vs. Replication Study, unpaired t-test.

**Supplemental Table 2. EEG band power, hypnogram, and $R_P$ as individual predictions of parenchymal contrast enhancement when added to the null model following overnight sleep.**

| | Predictor | Estimate | 95% CI | P Value | LRT | LRT P Value |
|---|---|---|---|---|---|---|
| **Predictors Added to Null Model** | **Delta Band Power** | 19.121 | (5.482, 32.760) | **0.007** | 7.50 | **0.006** |
| | **Theta Band Power** | -3.755 | (-11.982, 4.473) | 0.378 | 0.81 | 0.368 |
| | **Alpha Band Power** | -7.279 | (-12.264, -2.294) | **0.005** | 8.12 | **0.004** |
| | **Beta Band Power** | -5.329 | (-7.786, -2.873) | **<0.001** | 17.49 | **<0.001** |
| | **Heart Rate** | -21.624 | (-49.814, 6.566) | 0.139 | 2.28 | 0.131 |
| | **WASO Time** | -0.003 | (-0.045, 0.038) | 0.881 | 0.02 | 0.879 |
| | **N1 Sleep Time** | -0.128 | (-0.213, -0.042) | **0.004** | 8.46 | **0.004** |
| | **N2 Sleep Time** | -0.031 | (-0.071, 0.009) | 0.139 | 2.28 | 0.131 |
| | **N3 Sleep Time** | 0.025 | (-0.024, 0.075) | 0.322 | 1.02 | 0.313 |
| | **REM Sleep Time** | 0.031 | (-0.023, 0.086) | 0.268 | 1.28 | 0.258 |
| | **Parenchymal Resistance** | -38.080 | (-61.348, -14.812) | **0.002** | 10.15 | **0.001** |
| | | | | | | |
| **Null Model Fixed Effects** | **Blood CE** | 10.29 | (5.45, 15.13) | **<0.001** | – | – |
| | **CSF CE** | 148.48 | (123.40, 173.56) | **<0.001** | – | – |
| | **Age** | -1.31 | (-1.91, -0.71) | **<0.001** | – | – |
| | **Male Sex** | -2.69 | (-5.42, 0.063) | 0.060 | – | – |
| | **APOE ε4** | -3.29 | (-6.50, -0.091) | **0.048** | – | – |
| | | | | | | |
| **Null Model Random Effects** | $\sigma^2$ | 70.50 | – | – | – | – |
| | $T_{00\ ROI}$ | 12.60 | – | – | – | – |

Wake After Sleep Onset, WASO; Rapid Eye Movement, REM; Confidence Interval, CI; Likelihood Ratio Test, LRT. **Bolded P values reflect significant associations at P < 0.05**. Likelihood ratio test taken between null model and model with predictor.

**Supplemental Table 3. Multivariate models of morning brain parenchymal contrast enhancement using overnight and morning Rp, HR and EEG hypnogram predictors.**

| | | Full Model | | | Selected Model | | | Bootstrap Analysis | | | |
|---|---|---|---|---|---|---|---|---|---|---|---|
| **Predictor Period** | **Fixed Effect Predictors** | **Estimate** | **CI** | **p** | **Estimate** | **CI** | **p** | **Bootstrap Inclusion Frequency (%)** | **RMSD Ratio** | **Relative Conditional Bias (%)** | **Bootstrap Median** |
| **Overnight Sleep Opportunity** | Blood CE | 0.87 | -5.26, 7.00 | 0.786 | – | – | – | 11.6 | 2.14 | 386.83 | 0 |
| | CSF CE | 221.86 | 185.38, 258.34 | **<0.001** | 225.82 | (208.18, 243.47) | **<0.001** | 100.0 | 0.94 | 0.01 | 225.13 |
| | Age | -0.30 | -0.82, 0.23 | 0.286 | – | – | – | 39.8 | 1.86 | 107.95 | 0 |
| | Male Sex | -2.70 | -5.77, 0.36 | 0.094 | – | – | – | 41.8 | 1.07 | 53.57 | 0 |
| | APOE ε4 | -4.60 | -7.86, -1.35 | **0.008** | -5.33 | (-8.34, -2.31) | **0.001** | 81.6 | 0.98 | 16.33 | -4.77 |
| | $R_P$ | -76.16 | -99.79, -52.53 | **<0.001** | -67.17 | (-87.78, -46.56) | **<0.001** | 100.0 | 1.16 | -5.30 | -72.57 |
| | REM Time | 0.16 | 0.08, 0.24 | **<0.001** | 0.16 | (0.09, 0.23) | **<0.001** | 99.0 | 1.06 | 1.30 | 0.16 |
| | N1 Time | -0.30 | -0.43, -0.16 | **<0.001** | -0.32 | (-0.43, -0.21) | **<0.001** | 98.8 | 1.09 | 0.95 | -0.31 |
| | N2 Time | -0.10 | -0.14, -0.05 | **<0.001** | -0.10 | (-0.15, -0.06) | **<0.001** | 98.0 | 0.80 | -1.01 | -0.10 |
| | N3 Time | -0.09 | -0.15, -0.03 | **0.004** | -0.07 | (-0.12, -0.02) | **0.007** | 86.8 | 0.72 | -1.15 | -0.08 |
| | WASO Time | -0.07 | -0.13, -0.01 | **0.037** | -0.07 | (-0.12, -0.02) | **0.006** | 78.6 | 0.74 | 21.00 | -0.07 |
| | Heart Rate | -13.08 | -44.72, 18.57 | 0.432 | – | – | – | 24.2 | 1.84 | 133.52 | 0 |
| **Morning Sleep Opportunity** | Blood CE | 11.33 | 6.39, 16.28 | **<0.000** | 10.84 | (5.98,15.71) | **<0.001** | 98.6 | 0.97 | -5.49 | 10.59 |
| | CSF CE | 132.86 | 101.23, 164.50 | **<0.000** | 140.28 | (113.86, 166.71) | **<0.001** | 100.0 | 1.04 | 1.82 | 135.82 |
| | Age | -0.81 | -1.47, -0.144 | **0.022** | -0.95 | (-1.55, -0.34) | **0.003** | 75.8 | 1.28 | 38.20 | -0.94 |
| | Male Sex | -4.27 | -7.73, -0.82 | **0.020** | -3.24 | (-5.93, -0.55) | **0.023** | 69.0 | 0.84 | 9.25 | -3.57 |
| | APOE ε4 | -13.22 | -23.65, -2.79 | **0.017** | -9.25 | (-13.20, -5.29) | **<0.001** | 92.6 | 1.06 | -13.49 | -9.74 |
| | $R_P$ | 38.06 | 7.87, 68.24 | **0.018** | 34.42 | (5.25, 63.59) | **0.025** | 65.4 | 0.81 | 20.18 | 37.42 |
| | REM Time | 0.58 | 0.10, 1.06 | **0.024** | 0.41 | (0.20, 0.62) | **<0.001** | 88.2 | 1.00 | -14.04 | 0.40 |
| | N1 Time | -0.28 | -0.59, 0.02 | 0.080 | -0.26 | (-0.50, -0.02) | **0.040** | 61.6 | 0.93 | 36.23 | -0.29 |
| | N2 Time | -0.11 | -0.24, 0.022 | 0.116 | -0.13 | (-0.26, -0.01) | 0.051 | 41.4 | 1.30 | 63.35 | 0 |
| | N3 Time | -0.18 | -0.37, 0.00 | 0.063 | -0.17 | (-0.33, -0.021) | **0.031** | 44.2 | 0.65 | 15.70 | 0 |
| | WASO Time | 0.19 | -0.10, 0.56 | 0.344 | – | – | – | 33.4 | 1.53 | 57.53 | 0 |
| | Heart Rate | -23.75 | -107.49, 59.98 | 0.591 | – | – | – | 18.2 | 2.01 | -28.96 | 0 |

Electroencephalography, EEG; Parenchymal Resistance, $R_P$; Heart Rate, HR; Contrast Enhancement, CE; 95% Confidence Interval, CI; Backward Elimination, BE; Root-Mean Square Deviation, RMSD; within ROI variability, $\sigma^2$; inter-ROI variability, $T_{00\ ROI}$. **Bolded P values reflect significant associations at P < 0.05**. Shaded cells demark the **null model** that includes blood CE, CSF CE and potential biological confounders.

**Supplemental Table 4. The change in parenchymal resistance resulting from large changes in EEG band power and heart rate during REM sleep, NREM sleep and wake for each study.**

| | | | Fixed Effects | | | | Threshold Model Parameters | | |
|---|---|---|---|---|---|---|---|---|---|
| **Study / Condition** | **Sleep Stage** | **Predictors** | **Estimate** | **CI** | **p** | **DF** | **Positive Threshold** | **Negative Threshold** | **Slope Ratio** |
| **Benchmarking Study / Overnight Sleep Op** | **REM** | Δdelta | -0.42 | (-0.62, -0.21) | **<0.001** | 240 | 1.28 | -1.5 | 2 |
| | | Δtheta | -0.41 | (-0.91, 0.082) | 0.105 | 240 | 1.5 | -1.3 | 0.5 |
| | | Δalpha | -0.05 | (-0.21, 0.10) | 0.504 | 240 | 1.5 | -0.08 | 2 |
| | | Δbeta | 0.54 | (0.16, 0.91) | **0.006** | 240 | 1.5 | -1.35 | 0.5 |
| | | ΔHR | 0.10 | (-0.26, 0.47) | 0.588 | 202 | 1.5 | -0.9 | 0.5 |
| | **NREM** | Δdelta | -0.21 | (-0.46, 0.039) | 0.099 | 1038 | 1.5 | -1.5 | 0.95 |
| | | Δtheta | -0.12 | (-0.33, 0.090) | 0.263 | 1038 | 1.23 | -1.43 | 0.5 |
| | | Δalpha | -0.14 | (-0.30, 0.0063) | 0.061 | 1038 | 1.5 | -1.23 | 0.98 |
| | | Δbeta | 0.04 | (-0.039, 0.12) | 0.334 | 1038 | 1.3 | -1.5 | 2 |
| | | ΔHR | 0.13 | (0.014, 0.25) | **0.029** | 820 | 1.5 | -0.25 | 0.5 |
| **Benchmarking Study / Overnight Sleep Deprivation** | **WAKE** | Δdelta | -0.07 | (-0.18, 0.046) | 0.243 | 631 | 0.75 | 0 | 0.5 |
| | | Δtheta | -0.08 | (-0.17, 0.0084) | 0.076 | 631 | 0.73 | -1.5 | 2 |
| | | Δalpha | 0.07 | (-0.049, 0.19) | 0.245 | 631 | 1.5 | 0 | 0.5 |
| | | Δbeta | 0.05 | (-0.15, 0.26) | 0.601 | 631 | 1.5 | -1 | 0.83 |
| | | ΔHR | -0.10 | (-0.20, 0.0017) | 0.055 | 596 | 0.05 | 0 | 0.5 |
| **Replication Study / Overnight Sleep Op** | **REM** | Δdelta | -0.69 | (-1.1, -0.33) | **0.000** | 78 | 1.43 | -1.38 | 2 |
| | | Δtheta | -0.23 | (-0.39, -0.074) | **0.006** | 78 | 0.1 | -1.5 | 2 |
| | | Δalpha | -0.19 | (-0.46, 0.084) | 0.183 | 78 | 1.1 | -0.1 | 1.25 |
| | | Δbeta | 0.27 | (-0.13, 0.68) | 0.196 | 78 | 1.48 | -0.45 | 1.08 |
| | | ΔHR | 1.08 | (0.45, 1.7) | **0.001** | 68 | 1.5 | -1.23 | 0.9 |
| | **NREM** | Δdelta | -0.32 | (-0.57, -0.064) | **0.015** | 341 | 1.5 | -0.8 | 0.6 |
| | | Δtheta | 0.03 | (-0.043, 0.11) | 0.379 | 341 | 0 | -1.5 | 2 |
| | | Δalpha | 0.03 | (-0.049,0.11) | 0.482 | 341 | 0.03 | -1.5 | 2 |
| | | Δbeta | 0.13 | (0.045, 0.22) | **0.003** | 341 | 0.38 | -1.5 | 2 |
| | | ΔHR | 0.05 | (-0.14, 0.25) | 0.602 | 294 | 0.63 | -1.5 | 1.13 |
| **Replication Study / Overnight Sleep Deprivation** | **WAKE** | Δdelta | 0.04 | (-0.075, 0.16) | 0.479 | 505 | 0.8 | -1.5 | 2 |
| | | Δtheta | 0.03 | (-0.043, 0.096) | 0.460 | 505 | 0 | -1.5 | 2 |
| | | Δalpha | 0.09 | (-0.063, 0.25) | 0.247 | 505 | 1.15 | -1.5 | 2 |
| | | Δbeta | 0.18 | (0.031, 0.34) | **0.019** | 505 | 1.48 | -1.43 | 2 |
| | | ΔHR | -0.11 | (-0.27, 0.056) | 0.204 | 405 | 1 | -0.35 | 0.88 |

Rapid eye movement, REM; non-REM, NREM; Confidence Interval, CI; Degrees of Freedom, DF; EEG band power predictor units in percent of total band power; HR predictor units beats-per-minute. **Bolded P values reflect significant associations at P < 0.05**. Predictor and parenchymal resistance values in regression models were scaled to zero mean and unit standard deviation to simplify effect size comparisons across predictors. Positive and negative thresholds are in units of predictor standard deviation. Models included confounding biological variables age, gender, and APOE ε4 status.

**Supplemental Table 5. The change in parenchymal resistance resulting from large changes in EEG band power and heart rate at NREM-REM and sleep-wake transitions for each study.**

| | | Fixed Effects | | | | | Threshold Model Parameters | | |
|---|---|---|---|---|---|---|---|---|---|
| **Study** | **Transition** | **Predictors** | **Estimate** | **CI** | **P** | **DF** | **Positive Threshold** | **Negative Threshold** | **Slope Ratio** |
| **Benchmarking Study** | **NREM to REM** | Δalpha | 0.86 | (-0.05, 1.77) | 0.073 | 52 | 0.725 | -1.5 | 0.5 |
| | | Δbeta | 1.01 | (0.18, 1.85) | **0.023** | 52 | 0.35 | -1.5 | 0.5 |
| | | Δdelta | -0.31 | (-0.96, 0.34) | 0.359 | 52 | 1.5 | -1.15 | 2 |
| | | ΔHR | 0.10 | (-0.27, 0.47) | 0.593 | 37 | 1.5 | 0 | 2 |
| | | Δtheta | 0.28 | (-0.37, 0.93) | 0.405 | 52 | 0 | -1.5 | 0.5 |
| | **REM to NREM** | Δalpha | -0.17 | (-0.46, 0.13) | 0.276 | 45 | 1.5 | 0 | 2 |
| | | Δbeta | -0.08 | (-0.29, 0.13) | 0.445 | 45 | 0.2 | -1.5 | 1.9 |
| | | Δdelta | -0.43 | (-0.74, -0.11) | **0.011** | 45 | 1 | -0.9 | 2 |
| | | ΔHR | 0.32 | (-0.13, 0.78) | 0.180 | 34 | 1.5 | -0.625 | 2 |
| | | Δtheta | -0.03 | (-0.17, 0.1) | 0.628 | 45 | 0 | 0 | 2 |
| | **Sleep to Wake** | Δalpha | -0.89 | (-1.71, -0.08) | **0.038** | 53 | 0.775 | -1.5 | 0.5 |
| | | Δbeta | 0.67 | (-0.14, 1.47) | 0.114 | 53 | 0.35 | -1.5 | 0.5 |
| | | Δdelta | 0.03 | (-0.17, 0.23) | 0.778 | 53 | 0.025 | -1.45 | 2 |
| | | ΔHR | -0.32 | (-1.01, 0.38) | 0.383 | 39 | 0 | -1.4 | 0.5 |
| | | Δtheta | 0.04 | (-0.2, 0.29) | 0.737 | 53 | 0.25 | -1.5 | 1.75 |
| | **Wake to Sleep** | Δalpha | -0.31 | (-0.98, 0.37) | 0.377 | 89 | 1.5 | -0.975 | 0.525 |
| | | Δbeta | 0.45 | (-0.07, 0.96) | 0.095 | 89 | 1.5 | -1.25 | 2 |
| | | Δdelta | -0.22 | (-0.6, 0.17) | 0.273 | 89 | 0.2 | -1.5 | 0.9 |
| | | ΔHR | -0.11 | (-0.25, 0.03) | 0.145 | 64 | 0 | 0 | 2 |
| | | Δtheta | -0.20 | (-0.68, 0.27) | 0.409 | 89 | 0.05 | -1.3 | 0.5 |
| **Replication Study** | **REM to NREM** | Δalpha | 0.26 | (-0.46, 0.97) | 0.493 | 8 | 1.5 | -0.1 | 2 |
| | | Δbeta | -0.75 | (-2.45, 0.94) | 0.400 | 8 | 0.175 | -1.325 | 0.5 |
| | | Δdelta | 2.23 | (-0.7, 5.16) | 0.167 | 8 | 1.15 | -1.475 | 1.8 |
| | | ΔHR | -0.75 | (-2.21, 0.71) | 0.342 | 7 | 0.825 | -0.675 | 0.5 |
| | | Δtheta | 0.11 | (-0.73, 0.95) | 0.803 | 8 | 1.5 | -0.675 | 1.9 |
| | **REM to NREM** | Δalpha | -2.79 | (-5.55, -0.04) | 0.073 | 12 | 1.5 | -1.5 | 0.5 |
| | | Δbeta | 0.05 | (-0.4, 0.51) | 0.825 | 12 | 0.4 | -0.625 | 2 |
| | | Δdelta | -2.05 | (-4.21, 0.12) | 0.092 | 12 | 1.05 | -1.5 | 0.5 |
| | | ΔHR | -0.73 | (-6.16, 4.7) | 0.782 | 3 | 0.9 | -0.975 | 0.5 |
| | | Δtheta | -2.04 | (-2.97, -1.11) | **0.001** | 12 | 0.05 | -1.5 | 0.5 |
| | **Wake to Sleep** | Δalpha | 0.23 | (-0.5, 0.96) | 0.557 | 17 | 1.5 | -0.225 | 2 |
| | | Δbeta | 1.65 | (0.54, 2.76) | **0.011** | 17 | 0.1 | -1.5 | 0.5 |
| | | Δdelta | 2.55 | (-3.56, 8.66) | 0.436 | 17 | 1.425 | -1.5 | 0.5 |
| | | ΔHR | 0.36 | (-0.2, 0.91) | 0.236 | 17 | 1.5 | -0.025 | 2 |
| | | Δtheta | 0.03 | (-0.66, 0.73) | 0.931 | 17 | 1.5 | 0 | 2 |

Rapid eye movement, REM; non-REM, NREM; Confidence Interval, CI; Degrees of Freedom, DF; EEG band power predictor units in percent of total band power; HR predictor units beats-per-minute. **Bolded P values reflect significant associations at P < 0.05.** Predictor and parenchymal resistance values in regression models were scaled to zero mean and unit standard deviation with coefficient estimates representing effect size in standard deviations. Positive and negative thresholds are in units of predictor standard deviation.

1528 **Supplemental Table 6. Comparison of investigational device and polysomnography hypnogram staging to manual scoring.**

1529

| Manual Scoring | Device | | | | | | | | | | |
|---|---|---|---|---|---|---|---|---|---|---|---|
| | W | REM | N1 | N2 | N3 | | sensitivity | specificity | precision | accuracy | f1 |
| W | 2653 | 56 | 256 | 156 | 6 | | 0.828 | 0.959 | 0.843 | 0.932 | 0.835 |
| REM | 121 | 1334 | 130 | 127 | 2 | | 0.801 | 0.972 | 0.776 | 0.954 | 0.788 |
| N1 | 162 | 44 | 583 | 250 | 0 | | 0.367 | 0.967 | 0.558 | 0.905 | 0.443 |
| N2 | 224 | 224 | 611 | 4490 | 20 | | 0.774 | 0.886 | 0.804 | 0.844 | 0.789 |
| N3 | 7 | 5 | 2 | 753 | 877 | | 0.969 | 0.945 | 0.525 | 0.947 | 0.681 |
| | PSG C3 | | | | | | | | | | |
| | W | REM | N1 | N2 | N3 | | sensitivity | specificity | precision | accuracy | f1 |
| W | 2922 | 56 | 68 | 79 | 2 | | 0.892 | 0.981 | 0.928 | 0.962 | 0.910 |
| REM | 40 | 1563 | 37 | 74 | 0 | | 0.893 | 0.989 | 0.910 | 0.978 | 0.901 |
| N1 | 178 | 54 | 467 | 339 | 1 | | 0.707 | 0.961 | 0.447 | 0.950 | 0.547 |
| N2 | 94 | 76 | 85 | 5188 | 126 | | 0.870 | 0.958 | 0.929 | 0.924 | 0.899 |
| N3 | 4 | 0 | 1 | 262 | 1377 | | 0.914 | 0.979 | 0.825 | 0.973 | 0.867 |
| | PSG C4 | | | | | | | | | | |
| | W | REM | N1 | N2 | N3 | | sensitivity | specificity | precision | accuracy | f1 |
| W | 3035 | 22 | 31 | 39 | 0 | | 0.974 | 0.991 | 0.964 | 0.987 | 0.969 |
| REM | 3 | 1665 | 21 | 25 | 0 | | 0.965 | 0.996 | 0.969 | 0.993 | 0.967 |
| N1 | 27 | 20 | 659 | 333 | 0 | | 0.885 | 0.974 | 0.631 | 0.969 | 0.736 |
| N2 | 10 | 12 | 32 | 5493 | 22 | | 0.913 | 0.990 | 0.984 | 0.960 | 0.947 |
| N3 | 0 | 5 | 0 | 104 | 1535 | | 0.985 | 0.990 | 0.920 | 0.990 | 0.951 |

1530 Polysomnography, PSG; Wake, W; Rapid eye movement, REM

1531 **Supplemental Table 7: Electrode characterization according to ANSI/AAMI EC12*.**

1532

| Electrode Pair # | AC Impedance at 10 Hz [Ω] | DC Offset Voltage [mV] | Combined Offset Instability and Internal Noise [μV] | | Bias Current Tolerance [mV] |
|---|---|---|---|---|---|
| | | | EC12 (0.15-100 Hz) | EEG (0.3-50 Hz) | |
| 1 | 609 | 0.5 | 22.9 | 9.7 | 11.2 |
| 2 | 759 | 0.3 | 126.4 | 28.2 | 10.7 |
| 3 | 1023 | 3.8 | 13.3 | 7.9 | 10.8 |
| 4 | 1035 | 1.4 | 19.6 | 8.0 | 7.0 |
| 5 | 583 | 1.4 | 7.1 | 1.9 | 9.5 |
| 6 | 424 | 1.1 | 8.1 | 3.8 | 9.3 |

1533 Alternating Current, AC; Direct Current, DC; EC12, ANSI/AAMI EC12:2000/(R)2020.

*ANSI/AAMI EC12 reference values are as follows: AC impedance under 3000 Ω in any pair, under 2000 Ω on average; DC offset under 100 mV; offset instability and internal noise under 150 μV; tolerance to bias under 100 mV.

**Supplemental Table 8. Benchtop tests for assessing calibration and sensitivity to electrode impedance.**

| | | Electrode Configuration | | | | Load | Measured Load Components |
|---|---|---|---|---|---|---|---|
| | | Left | | Right | | | Measured |
| | **Setting** | **MASTOID** | **IN-EAR** | **IN-EAR** | **MASTOID** | **[Ω]** | **[Ω]** |
| | **Cal R 20** | Low | Low | Low | Low | 20 | 20.0 |
| | **Cal R 40** | Low | Low | Low | Low | 40.2 | 40.2 |
| | **Cal R 60** | Low | Low | Low | Low | 60.4 | 60.3 |
| | **Cal R 80** | Low | Low | Low | Low | 80.6 | 80.5 |
| | **Cal R 100** | Low | Low | Low | Low | 100 | 100.4 |
| **Calibration 2R1C** | **Cal 2R1C 20** | Low | Low | Low | Low | 20\|(470 + 22n) | Rs = 20, Rp=468.2, Cp = 23.3n |
| **Calibration 2R1C** | **Cal 2R1C 40** | Low | Low | Low | Low | 40.2\|(470 + 22n) | Rs = 40.2, Rp=468.2, Cp = 23.3n |
| **Calibration 2R1C** | **Cal 2R1C 60** | Low | Low | Low | Low | 60.4\|(470 + 22n) | Rs = 60.3, Rp=468.2, Cp = 23.3n |
| **Calibration 2R1C** | **Cal 2R1C 80** | Low | Low | Low | Low | 80.6\|(470 + 22n) | Rs = 80.5, Rp=468.2, Cp = 23.3n |
| **Calibration 2R1C** | **Cal 2R1C 100** | Low | Low | Low | Low | 100\|(470 + 22n) | Rs = 100.4, Rp=468.2, Cp = 23.3n |
| **Sensitivity to Electrode Impedance** | **Low All** | Low | Low | Low | Low | 50\|(470 + 22n) | Rs = 49.9, Rp=468.2, Cp = 23.3n |
| **Sensitivity to Electrode Impedance** | **High Right Mastoid** | Low | Low | Low | High | 50\|(470 + 22n) | Rs = 49.9, Rp=468.2, Cp = 23.3n |
| **Sensitivity to Electrode Impedance** | **High Right** | Low | Low | High | High | 50\|(470 + 22n) | Rs = 49.9, Rp=468.2, Cp = 23.3n |
| **Sensitivity to Electrode Impedance** | **High Right In-Ear** | Low | Low | High | Low | 50\|(470 + 22n) | Rs = 49.9, Rp=468.2, Cp = 23.3n |
| **Sensitivity to Electrode Impedance** | **High In-Ear** | Low | High | High | Low | 50\|(470 + 22n) | Rs = 49.9, Rp=468.2, Cp = 23.3n |
| **Sensitivity to Electrode Impedance** | **High Left In-Ear** | Low | High | Low | Low | 50\|(470 + 22n) | Rs = 49.9, Rp=468.2, Cp = 23.3n |
| **Sensitivity to Electrode Impedance** | **High Left** | High | High | Low | Low | 50\|(470 + 22n) | Rs = 49.9, Rp=468.2, Cp = 23.3n |
| **Sensitivity to Electrode Impedance** | **High Left Mastoid** | High | Low | Low | Low | 50\|(470 + 22n) | Rs = 49.9, Rp=468.2, Cp = 23.3n |
| **Sensitivity to Electrode Impedance** | **High Mastoids** | High | Low | Low | High | 50\|(470 + 22n) | Rs = 49.9, Rp=468.2, Cp = 23.3n |
| **Sensitivity to Electrode Impedance** | **High All** | High | High | High | High | 50\|(470 + 22n) | Rs = 49.9, Rp=468.2, Cp = 23.3n |

Element to change from one benchtop test to the next

**Supplemental Table 9. Absolute error of resistance for benchtop tests (values in ohms).**

| | Setting | 1kHz | 1.6kHz | 2.28kHz | 3.2kHz | 4.55kHz | 6.4kHz | 8.53kHz | 12.8kHz | 16kHz | 25.6kHz | 32kHz | 51.2kHz | 64kHz | 85.3kHz | 102kHz | 128kHz |
|---|---|---|---|---|---|---|---|---|---|---|---|---|---|---|---|---|---|
| Calibration R | Cal R 20 | 0.125 | 0.151 | 0.157 | 0.119 | 0.127 | 0.154 | 0.182 | 0.190 | 0.220 | 0.308 | 0.320 | 0.274 | 0.094 | 0.379 | 0.700 | 0.702 |
| | Cal R 40 | 0.220 | 0.161 | 0.152 | 0.192 | 0.221 | 0.094 | 0.164 | 0.117 | 0.127 | 0.151 | 0.200 | 0.301 | 0.134 | 0.438 | 0.344 | 0.396 |
| | Cal R 60 | 0.333 | 0.231 | 0.325 | 0.307 | 0.301 | 0.413 | 0.411 | 0.208 | 0.308 | 0.326 | 0.276 | 0.456 | 0.327 | 0.412 | 0.268 | 0.301 |
| | Cal R 80 | 0.104 | 0.175 | 0.242 | 0.205 | 0.314 | 0.140 | 0.154 | 0.257 | 0.258 | 0.332 | 0.333 | 0.257 | 0.284 | 0.298 | 0.317 | 0.230 |
| | Cal R 100 | 0.301 | 0.288 | 0.268 | 0.251 | 0.261 | 0.323 | 0.236 | 0.271 | 0.458 | 0.380 | 0.199 | 0.157 | 0.387 | 0.324 | 0.196 | 0.134 |
| Calibration 2R1C | Cal 2R1C 20 | 0.232 | 0.277 | 0.244 | 0.105 | 0.130 | 0.125 | 0.141 | 0.087 | 0.211 | 0.247 | 0.383 | 0.355 | 0.228 | 0.371 | 0.522 | 0.756 |
| | Cal 2R1C 40 | 0.191 | 0.117 | 0.112 | 0.305 | 0.207 | 0.042 | 0.207 | 0.149 | 0.268 | 0.157 | 0.134 | 0.240 | 0.314 | 0.242 | 0.421 | 0.311 |
| | Cal 2R1C 60 | 0.372 | 0.213 | 0.356 | 0.292 | 0.202 | 0.209 | 0.263 | 0.276 | 0.333 | 0.475 | 0.260 | 0.301 | 0.522 | 0.434 | 0.380 | 0.318 |
| | Cal 2R1C 80 | 0.215 | 0.166 | 0.249 | 0.175 | 0.186 | 0.252 | 0.231 | 0.168 | 0.348 | 0.384 | 0.303 | 0.211 | 0.333 | 0.331 | 0.280 | 0.143 |
| | Cal 2R1C 100 | 0.384 | 0.304 | 0.256 | 0.295 | 0.195 | 0.159 | 0.294 | 0.283 | 0.428 | 0.423 | 0.339 | 0.379 | 0.208 | 0.172 | 0.193 | 0.021 |
| Sensitivity to Electrode Impedance | Low All | 0.284 | 0.159 | 0.181 | 0.318 | 0.227 | 0.171 | 0.280 | 0.263 | 0.136 | 0.152 | 0.165 | 0.279 | 0.237 | 0.192 | 0.454 | 0.330 |
| | High Right Mastoid | 0.123 | 0.003 | 0.165 | 0.220 | 0.176 | 0.210 | 0.071 | 0.120 | 0.128 | 0.085 | 0.001 | 0.300 | 0.242 | 0.650 | 0.362 | 0.725 |
| | High Right | 0.131 | 0.242 | 0.079 | 0.279 | 0.232 | 0.253 | 0.274 | 0.144 | 0.202 | 0.186 | 0.167 | -0.022 | 0.383 | 0.586 | 0.620 | 0.911 |
| | High Right In-Ear | 0.259 | 0.256 | 0.249 | 0.297 | 0.252 | 0.347 | 0.183 | 0.182 | 0.279 | 0.256 | 0.212 | 0.315 | 0.139 | 0.529 | 0.457 | 0.576 |
| | High In-Ear | 0.384 | 0.263 | 0.109 | 0.233 | 0.350 | 0.236 | 0.237 | 0.292 | 0.266 | 0.259 | 0.312 | 0.327 | 0.379 | 0.415 | 0.446 | 0.450 |
| | High Left In-Ear | 0.210 | 0.169 | 0.236 | 0.313 | 0.262 | 0.319 | 0.229 | 0.269 | 0.280 | 0.332 | 0.324 | 0.168 | 0.303 | 0.255 | 0.361 | 0.310 |
| | High Left | 0.266 | 0.337 | 0.372 | 0.241 | 0.271 | 0.281 | 0.252 | 0.167 | 0.388 | 0.501 | 0.416 | 0.266 | 0.128 | 0.225 | 0.218 | 0.006 |
| | High Left Mastoid | 0.341 | 0.325 | 0.217 | 0.225 | 0.222 | 0.193 | 0.185 | 0.242 | 0.430 | 0.363 | 0.269 | 0.242 | 0.143 | 0.097 | 0.268 | 0.018 |
| | High Mastoids | 0.307 | 0.227 | 0.235 | 0.364 | 0.286 | 0.192 | 0.348 | 0.363 | 0.339 | 0.277 | 0.238 | 0.146 | 0.498 | 0.455 | 0.492 | 0.487 |
| | High All | 0.517 | 0.412 | 0.447 | 0.374 | 0.418 | 0.420 | 0.342 | 0.397 | 0.425 | 0.461 | 0.375 | 0.418 | 0.527 | 0.727 | 0.852 | 0.843 |

1544 **Supplemental Table 10. Absolute error of reactance for benchtop tests (values in ohms).**

1545

| | Setting | 1kHz | 1.6kHz | 2.28kHz | 3.2kHz | 4.55kHz | 6.4kHz | 8.53kHz | 12.8kHz | 16kHz | 25.6kHz | 32kHz | 51.2kHz | 64kHz | 85.3kHz | 102kHz | 128kHz |
|---|---|---|---|---|---|---|---|---|---|---|---|---|---|---|---|---|---|
| Calibration R | Cal R 20 | 0.087 | -0.031 | 0.055 | -0.046 | 0.010 | -0.016 | 0.104 | -0.030 | 0.142 | 0.237 | 0.172 | 0.188 | 0.018 | 0.250 | 0.197 | 0.288 |
| | Cal R 40 | 0.032 | 0.042 | 0.011 | 0.055 | -0.054 | -0.057 | 0.126 | 0.035 | 0.018 | -0.027 | 0.027 | 0.087 | -0.070 | 0.057 | 0.102 | 0.040 |
| | Cal R 60 | 0.103 | 0.007 | -0.025 | 0.070 | -0.052 | -0.017 | 0.025 | 0.044 | 0.069 | -0.071 | 0.090 | -0.041 | -0.032 | -0.129 | -0.050 | -0.107 |
| | Cal R 80 | 0.036 | 0.073 | 0.015 | -0.132 | -0.042 | 0.064 | 0.012 | -0.010 | 0.047 | 0.072 | 0.040 | -0.010 | -0.061 | -0.092 | -0.162 | -0.181 |
| | Cal R 100 | -0.066 | -0.054 | 0.028 | -0.019 | 0.011 | 0.153 | 0.057 | -0.051 | -0.002 | 0.022 | 0.045 | -0.003 | -0.133 | -0.024 | -0.050 | -0.121 |
| Calibration 2R1C | Cal 2R1C 20 | 0.044 | -0.039 | -0.037 | 0.019 | 0.043 | 0.033 | 0.031 | 0.051 | 0.091 | 0.143 | 0.210 | 0.211 | 0.237 | 0.285 | 0.413 | 0.380 |
| | Cal 2R1C 40 | 0.001 | -0.070 | -0.029 | 0.084 | -0.049 | 0.030 | -0.050 | -0.033 | 0.026 | 0.000 | -0.008 | 0.020 | 0.117 | 0.074 | 0.097 | 0.114 |
| | Cal 2R1C 60 | 0.019 | 0.006 | -0.043 | -0.017 | 0.009 | 0.032 | 0.120 | -0.120 | -0.005 | 0.034 | -0.149 | 0.089 | 0.106 | 0.041 | 0.204 | 0.122 |
| | Cal 2R1C 80 | 0.095 | -0.005 | 0.018 | 0.145 | -0.018 | -0.073 | 0.001 | 0.017 | 0.013 | 0.010 | 0.145 | 0.058 | 0.076 | -0.012 | -0.028 | 0.104 |
| | Cal 2R1C 100 | -0.030 | -0.118 | -0.014 | 0.065 | -0.066 | 0.025 | 0.070 | 0.055 | 0.074 | 0.037 | 0.174 | 0.158 | 0.012 | 0.092 | 0.041 | 0.105 |
| Sensitivity to Electrode Impedance | Low All | 0.015 | -0.066 | 0.047 | -0.052 | 0.046 | 0.016 | 0.068 | -0.040 | -0.032 | -0.112 | 0.006 | 0.107 | 0.121 | 0.006 | 0.093 | 0.112 |
| | High Right Mastoid | 0.113 | 0.084 | 0.030 | 0.095 | 0.131 | -0.034 | 0.043 | 0.043 | 0.103 | 0.139 | 0.160 | 0.251 | 0.309 | 0.388 | 0.389 | 0.306 |
| | High Right | 0.029 | 0.059 | -0.024 | 0.159 | 0.000 | 0.098 | 0.028 | 0.016 | 0.059 | 0.124 | 0.186 | 0.136 | 0.243 | 0.204 | 0.459 | 0.335 |
| | High Right In-Ear | 0.015 | -0.074 | -0.001 | -0.019 | 0.073 | 0.044 | 0.076 | 0.042 | 0.011 | 0.073 | 0.047 | 0.131 | 0.123 | -0.009 | 0.150 | 0.133 |
| | High In-Ear | 0.071 | -0.015 | 0.000 | -0.074 | 0.026 | -0.104 | -0.007 | 0.028 | 0.087 | 0.045 | 0.021 | 0.103 | 0.203 | 0.111 | 0.043 | 0.160 |
| | High Left In-Ear | -0.007 | 0.001 | 0.015 | 0.013 | -0.042 | -0.168 | 0.045 | 0.010 | -0.049 | 0.006 | -0.032 | 0.038 | 0.237 | 0.150 | 0.070 | 0.137 |
| | High Left | -0.150 | -0.117 | -0.154 | -0.178 | 0.012 | -0.104 | -0.025 | -0.124 | -0.172 | -0.159 | -0.127 | -0.253 | -0.173 | -0.147 | -0.124 | -0.099 |
| | High Left Mastoid | -0.173 | -0.093 | -0.169 | -0.045 | -0.104 | -0.073 | 0.001 | -0.104 | -0.032 | -0.211 | -0.271 | -0.187 | -0.212 | -0.076 | -0.251 | -0.091 |
| | High Mastoids | 0.034 | -0.002 | 0.036 | -0.023 | -0.100 | -0.010 | -0.054 | 0.032 | -0.042 | -0.103 | 0.008 | -0.006 | 0.083 | 0.082 | 0.176 | 0.058 |
| | High All | -0.041 | -0.114 | -0.083 | -0.109 | -0.091 | -0.066 | -0.051 | 0.065 | 0.083 | 0.103 | 0.013 | 0.138 | 0.278 | 0.296 | 0.389 | 0.401 |

1546

1547

1548

**Supplemental Table 11. Debye model absolute prediction error (ohms) of dispersion relative to 128kHz.**

| | Setting | 1kHz | 1.6kHz | 2.28kHz | 3.2kHz | 4.55kHz | 6.4kHz | 8.53kHz | 12.8kHz | 16kHz | 25.6kHz | 32kHz | 51.2kHz | 64kHz | 85.3kHz | 102kHz |
|---|---|---|---|---|---|---|---|---|---|---|---|---|---|---|---|---|
| Sensitivity to Electrode Impedance | Low All | -0.037 | -0.040 | -0.044 | -0.051 | -0.063 | -0.080 | -0.093 | -0.098 | -0.091 | -0.058 | -0.042 | -0.017 | -0.010 | -0.004 | -0.002 |
| | High Right Mastoid | -0.243 | -0.250 | -0.260 | -0.278 | -0.309 | -0.345 | -0.368 | -0.352 | -0.311 | -0.187 | -0.133 | -0.054 | -0.032 | -0.014 | -0.006 |
| | High Right | -0.247 | -0.252 | -0.261 | -0.277 | -0.302 | -0.332 | -0.350 | -0.331 | -0.291 | -0.175 | -0.124 | -0.050 | -0.030 | -0.013 | -0.006 |
| | High Right In-Ear | -0.109 | -0.113 | -0.120 | -0.132 | -0.152 | -0.178 | -0.197 | -0.197 | -0.177 | -0.110 | -0.079 | -0.032 | -0.019 | -0.008 | -0.004 |
| | High In-Ear | -0.128 | -0.130 | -0.134 | -0.140 | -0.150 | -0.162 | -0.168 | -0.158 | -0.139 | -0.084 | -0.060 | -0.024 | -0.015 | -0.006 | -0.003 |
| | High Left In-Ear | -0.055 | -0.053 | -0.051 | -0.046 | -0.039 | -0.027 | -0.015 | 0.000 | 0.005 | 0.007 | 0.006 | 0.003 | 0.002 | 0.001 | 0.000 |
| | High Left | 0.065 | 0.069 | 0.074 | 0.082 | 0.098 | 0.119 | 0.136 | 0.144 | 0.133 | 0.087 | 0.063 | 0.026 | 0.016 | 0.007 | 0.003 |
| | High Left Mastoid | 0.067 | 0.070 | 0.075 | 0.084 | 0.099 | 0.118 | 0.135 | 0.142 | 0.131 | 0.085 | 0.062 | 0.026 | 0.015 | 0.007 | 0.003 |
| | High Mastoids | -0.119 | -0.120 | -0.121 | -0.124 | -0.127 | -0.131 | -0.130 | -0.116 | -0.100 | -0.059 | -0.042 | -0.017 | -0.010 | -0.004 | -0.002 |
| | High All | -0.202 | -0.209 | -0.221 | -0.240 | -0.271 | -0.311 | -0.338 | -0.329 | -0.293 | -0.178 | -0.127 | -0.052 | -0.031 | -0.013 | -0.006 |

| | | | | | | | | | | | | | | | |
|---|---|---|---|---|---|---|---|---|---|---|---|---|---|---|---|
| RMSE | 0.147 | 0.151 | 0.157 | 0.168 | 0.186 | 0.209 | 0.224 | 0.216 | 0.193 | 0.117 | 0.084 | 0.034 | 0.020 | 0.009 | 0.004 |
| Load Value | 4.766 | 4.724 | 4.654 | 4.526 | 4.282 | 3.877 | 3.374 | 2.461 | 1.931 | 0.995 | 0.685 | 0.286 | 0.183 | 0.099 | 0.066 |
| Error % | 3.1% | 3.2% | 3.4% | 3.7% | 4.3% | 5.4% | 6.6% | 8.8% | 10.0% | 11.8% | 12.2% | 12.0% | 11.1% | 8.8% | 6.1% |

**Supplemental Table 12: Minimum significant change in mean $R_p$ and correlation with a predictor using the $R_p$ standard deviation of the electrode impedance sensitivity tests.**

| **Number of Samples** | **25** | **100** |
|---|---|---|
| **Standard Deviation [Ω]** | 0.113 | 0.113 |
| **Standard Error [Ω]** | 0.023 | 0.011 |
| **Minimum Significant Change [Ω]** | 0.044 | 0.022 |
| **Minimum Significant Correlation** | 0.39 | 0.20 |

Brain parenchymal resistance, $R_p$**.**

1559

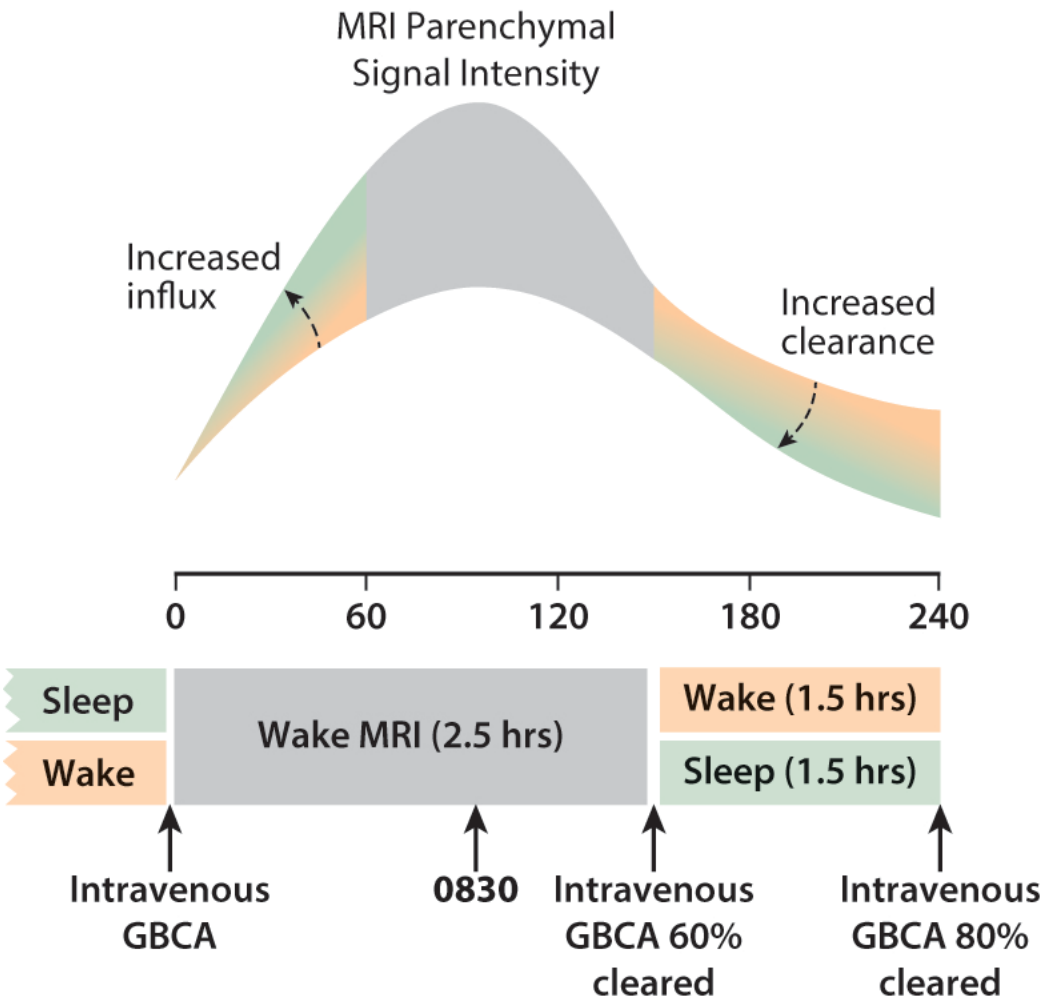


**Supplemental Figure 1.** An illustration of the effect of increased CSF influx into the brain parenchyma and clearance from the parenchyma on contrast-enhanced MRI signal intensity in the Benchmarking study. An increase in CSF influx into the brain parenchyma following intravenous GBCA leads to greater contrast delivery to the brain parenchyma and a corresponding increase in MRI signal intensity. MRI signal intensity of the brain parenchyma has been shown to peak at approximately 90 minutes post-injection[15] which occurred at time 0830 in the Benchmarking study. With a terminal half-life of 109 minutes[28], intravenous contrast is 60% cleared at 140 minutes post-injection when the morning sleep/wake intervention begins and is 80% cleared at the end of the morning intervention when the second post-contrast MRI scan is acquired. During this morning intervention, an increase in CSF clearance from the brain parenchyma leads to a corresponding decrease in MRI signal intensity.

**Supplemental Figure 2.**

**a**

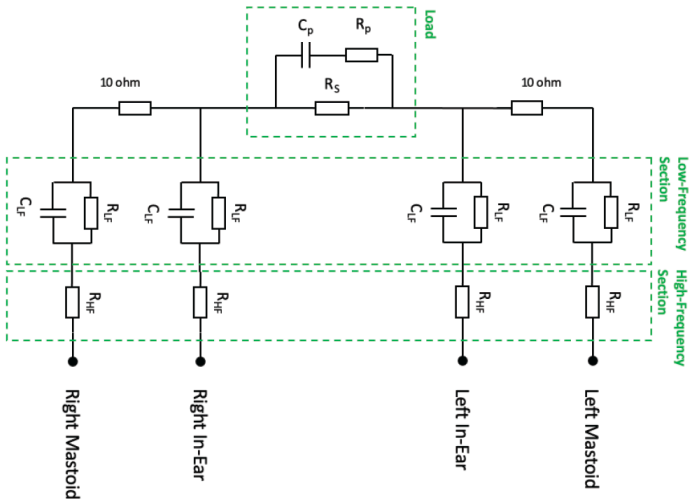


**b**

**Electrode Models**

| | $R_{HF}$ | $R_{LF}$ | $C_{LF}$ |
|---|---|---|---|
| **Low** | 270 | 1k | 180n |
| **High** | 620 | 3.3k | 82n |

**c**

**Load Models**

| | $R_s$ | $R_p$ | $C_p$ |
|---|---|---|---|
| **Cal Loads** | 0-100 | -/470 | -/22n |
| **Realistic Load** | 50* | 470 | 22n |

* 50 realized with a 49.9 ohm resistor

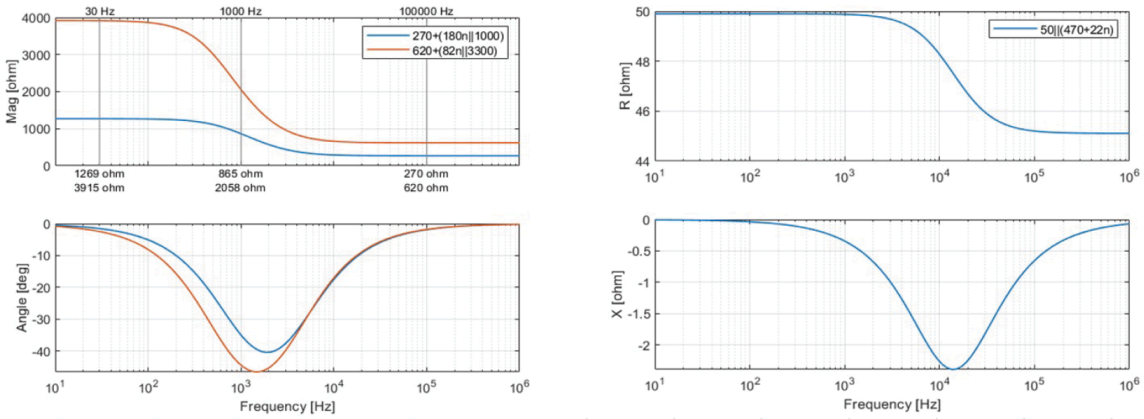


**Supplemental Figure 2. a,** Circuit model of transcranial measurements using four-point electrical impedance spectroscopy and models for each of the four electrode contact impedances. **b**, Electrode impedance models comprised a low impedance and a high impedance model, representing the range of in-human impedances. **c**, Calibration loads varied the resistance $\mathbf{R_s}$ of the free fluid or interstitial fluid compartment from 20 to 100 Ω in increments of 20 Ω, with and additional $R_pC_p$ in parallel to simulate complex loads. The realistic load parameters were chosen to create a frequency dispersion that approximated the in-human measured dispersions. **d**, Electrode impedance dispersion over the measured frequencies for the low and high impedance model. **e**, Load impedance dispersion over the measured frequencies using the Real Load model.

**Supplemental Figure 3.**

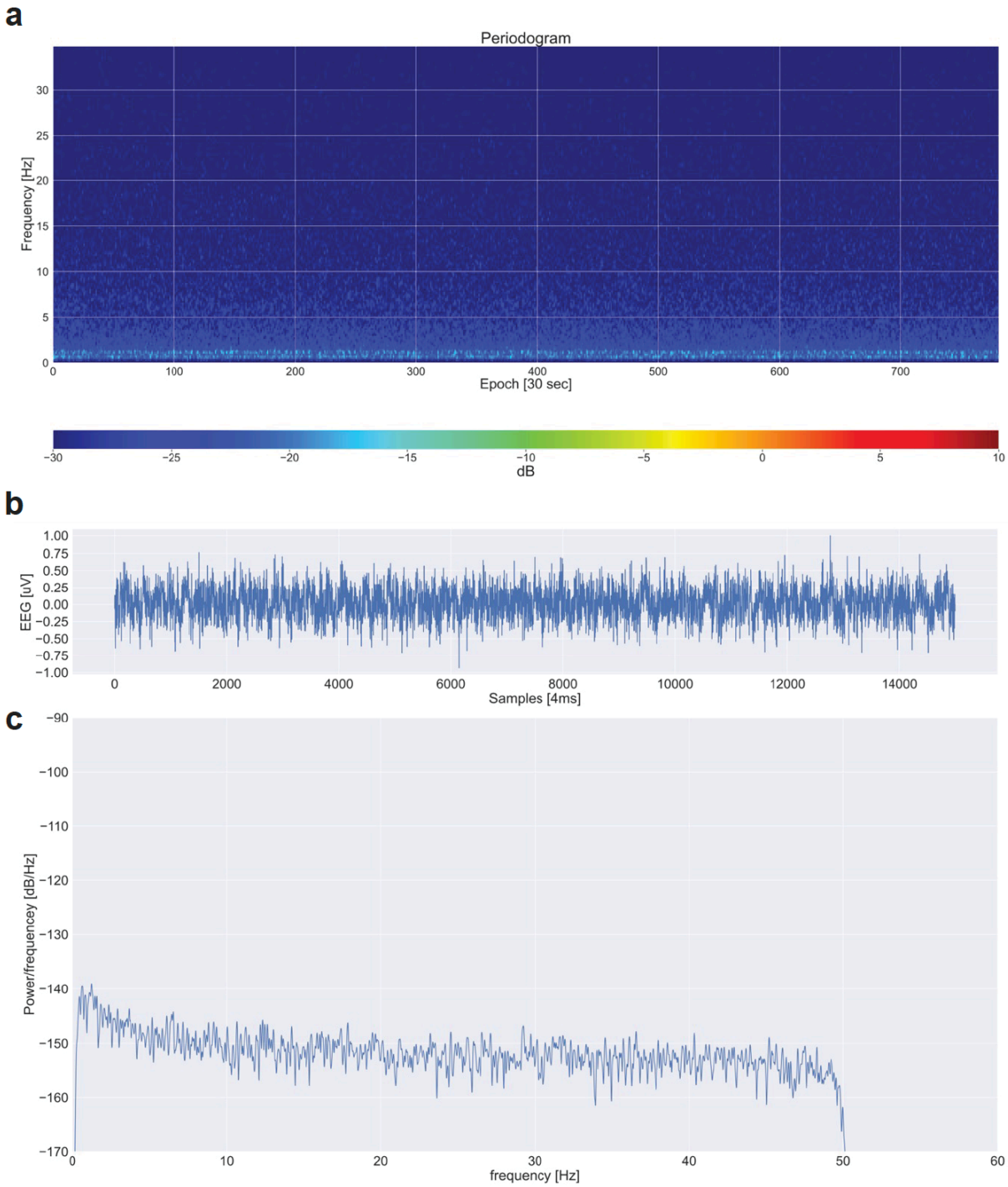


**Supplemental Figure 3. a**, Periodogram of a device over a 12 hour test using four Ag/AgCl sintered disk electrodes on an Agar phantom with EEG gel. For reference, human EEG beta power during NREM sleep is above -10dB on the device. **b**, EEG recording over an epoch shows 0.5 μV peak-to-peak noise. **c**, Power spectral density shows a noise floor at -150dB/Hz with a 1/f increase to -140db/Hz below 10Hz.

## REFERENCES


1 Iliff, J. J. *et al.* A paravascular pathway facilitates CSF flow through the brain parenchyma and the clearance of interstitial solutes, including amyloid β. *Sci Transl Med* **4**, 147ra111 (2012). https://doi.org/10.1126/scitranslmed.3003748

2 Xie, L. *et al.* Sleep drives metabolite clearance from the adult brain. *Science* **342**, 373-377 (2013). https://doi.org/10.1126/science.1241224

3 Iliff, J. J. *et al.* Impairment of glymphatic pathway function promotes tau pathology after traumatic brain injury. *J Neurosci* **34**, 16180-16193 (2014). https://doi.org/10.1523/JNEUROSCI.3020-14.2014

4 Harrison, I. F. *et al.* Impaired glymphatic function and clearance of tau in an Alzheimer's disease model. *Brain* **143**, 2576-2593 (2020). https://doi.org/10.1093/brain/awaa179

5 Ishida, K. *et al.* Glymphatic system clears extracellular tau and protects from tau aggregation and neurodegeneration. *J Exp Med* **219** (2022). https://doi.org/10.1084/jem.20211275

6 Cui, H. *et al.* Decreased AQP4 Expression Aggravates α-Synuclein Pathology in Parkinson's Disease Mice, Possibly via Impaired Glymphatic Clearance. *J Mol Neurosci* **71**, 2500-2513 (2021). https://doi.org/10.1007/s12031-021-01836-4

7 Zou, W. *et al.* Blocking meningeal lymphatic drainage aggravates Parkinson's disease-like pathology in mice overexpressing mutated α-synuclein. *Transl Neurodegener* **8**, 7 (2019). https://doi.org/10.1186/s40035-019-0147-y

8 Hablitz, L. M. & Nedergaard, M. The Glymphatic System: A Novel Component of Fundamental Neurobiology. *J Neurosci* **41**, 7698-7711 (2021). https://doi.org/10.1523/JNEUROSCI.0619-21.2021

9 Klostranec, J. M. *et al.* Current Concepts in Intracranial Interstitial Fluid Transport and the Glymphatic System: Part II-Imaging Techniques and Clinical Applications. *Radiology* **301**, 516-532 (2021). https://doi.org/10.1148/radiol.2021204088

10 Hablitz, L. M. *et al.* Circadian control of brain glymphatic and lymphatic fluid flow. *Nat Commun* **11**, 4411 (2020). https://doi.org/10.1038/s41467-020-18115-2

11 Hablitz, L. M. *et al.* Increased glymphatic influx is correlated with high EEG delta power and low heart rate in mice under anesthesia. *Sci Adv* **5**, eaav5447 (2019). https://doi.org/10.1126/sciadv.aav5447

12 Eide, P. K., Vinje, V., Pripp, A. H., Mardal, K. A. & Ringstad, G. Sleep deprivation impairs molecular clearance from the human brain. *Brain* **144**, 863-874 (2021). https://doi.org/10.1093/brain/awaa443

13 Ringstad, G. *et al.* Brain-wide glymphatic enhancement and clearance in humans assessed with MRI. *JCI Insight* **3** (2018). https://doi.org/10.1172/jci.insight.121537

14 Deike-Hofmann, K. *et al.* Glymphatic Pathway of Gadolinium-Based Contrast Agents Through the Brain: Overlooked and Misinterpreted. *Invest Radiol* **54**, 229-237 (2019). https://doi.org/10.1097/RLI.0000000000000533

15 Richmond, S. B. *et al.* Quantification approaches for magnetic resonance imaging following intravenous gadolinium injection: A window into brain-wide glymphatic function. *Eur J Neurosci* **57**, 1689-1704 (2023). https://doi.org/10.1111/ejn.15974

16 Bera, T. K. Bioelectrical Impedance Methods for Noninvasive Health Monitoring: A Review. *J Med Eng* **2014**, 381251 (2014). https://doi.org/10.1155/2014/381251

17 Abasi, S., Aggas, J. R., Garayar-Leyva, G. G., Walther, B. K. & Guiseppi-Elie, A. Bioelectrical Impedance Spectroscopy for Monitoring Mammalian Cells and Tissues

under Different Frequency Domains: A Review. *ACS Meas Sci Au* **2**, 495-516 (2022). https://doi.org/10.1021/acsmeasuresciau.2c00033

18 Stupin, D. D. *et al.* Bioimpedance Spectroscopy: Basics and Applications. *ACS Biomater Sci Eng* **7**, 1962-1986 (2021). https://doi.org/10.1021/acsbiomaterials.0c01570

19 Gabriel, S., Lau, R. W. & Gabriel, C. The dielectric properties of biological tissues: II. Measurements in the frequency range 10 Hz to 20 GHz. *Phys Med Biol* **41**, 2251-2269 (1996). https://doi.org/10.1088/0031-9155/41/11/002

20 Gabriel, C. Dielectric properties of biological tissue: variation with age. *Bioelectromagnetics* **Suppl 7**, S12-18 (2005). https://doi.org/10.1002/bem.20147

21 Jessen, N. A., Munk, A. S., Lundgaard, I. & Nedergaard, M. The Glymphatic System: A Beginner's Guide. *Neurochem Res* **40**, 2583-2599 (2015). https://doi.org/10.1007/s11064-015-1581-6

22 Nakamura, K. *et al.* Diurnal fluctuations in brain volume: Statistical analyses of MRI from large populations. *Neuroimage* **118**, 126-132 (2015). https://doi.org/10.1016/j.neuroimage.2015.05.077

23 Elvsåshagen, T. *et al.* Cerebral blood flow changes after a day of wake, sleep, and sleep deprivation. *Neuroimage* **186**, 497-509 (2019). https://doi.org/10.1016/j.neuroimage.2018.11.032

24 Dagum, P. Non-invasive assessment of glymphatic flow and neurodegeneration from a wearable device. (**2022**).

25 Dagum, P. Non-invasive assessment of glymphatic flow and neurodegeneration from a wearable device. (2022).

26 Nasreddine, Z. S. *et al.* The Montreal Cognitive Assessment, MoCA: a brief screening tool for mild cognitive impairment. *J Am Geriatr Soc* **53**, 695-699 (2005). https://doi.org/10.1111/j.1532-5415.2005.53221.x

27 Brown, L. M. & Schinka, J. A. Development and initial validation of a 15-item informant version of the Geriatric Depression Scale. *Int J Geriatr Psychiatry* **20**, 911-918 (2005). https://doi.org/10.1002/gps.1375

28 Administration., U. F. a. D. *Gadavist (gadobutrol) injection, for intravenous use*, <https://www.accessdata.fda.gov/drugsatfda_docs/label/2011/201277s000lbl.pdf> (2011).

29 Heinze, G., Wallisch, C. & Dunkler, D. Variable selection - A review and recommendations for the practicing statistician. *Biom J* **60**, 431-449 (2018). https://doi.org/10.1002/bimj.201700067

30 Iliff, J. J. *et al.* Brain-wide pathway for waste clearance captured by contrast-enhanced MRI. *J Clin Invest* **123**, 1299-1309 (2013). https://doi.org/10.1172/JCI67677

31 Boukamp, B. A. A Linear Kronig-Kramers Transform Test for Immittance Data Validation. *Journal of The Electrochemical Society* **142**, 1885 (1995).

32 Schonleber, M., Klotz, D. & Ivers-Tiffee, E. A Method for Improving the Robustness of linear Kramers-Kronig Validity Tests. *Electrochimica Acta* **131**, 20-27 (2014).

33 Song, J. *et al.* Electrical Impedance Changes at Different Phases of Cerebral Edema in Rats with Ischemic Brain Injury. *Biomed Res Int* **2018**, 9765174 (2018). https://doi.org/10.1155/2018/9765174

34 Abboud, T., Mielke, D. & Rohde, V. Mini Review: Impedance Measurement in Neuroscience and Its Prospective Application in the Field of Surgical Neurooncology. *Front Neurol* **12**, 825012 (2021). https://doi.org/10.3389/fneur.2021.825012

35 Witkowska-Wrobel, A., Aristovich, K., Crawford, A., Perkins, J. D. & Holder, D. Imaging of focal seizures with Electrical Impedance Tomography and depth electrodes in real time. *Neuroimage* **234**, 117972 (2021). https://doi.org/10.1016/j.neuroimage.2021.117972

36 Romsauerova, A. *et al.* Multi-frequency electrical impedance tomography (EIT) of the adult human head: initial findings in brain tumours, arteriovenous malformations and chronic stroke, development of an analysis method and calibration. *Physiol Meas* **27**, S147-161 (2006). https://doi.org/10.1088/0967-3334/27/5/S13

37 Iliff, J. J. *et al.* Cerebral arterial pulsation drives paravascular CSF-interstitial fluid exchange in the murine brain. *J Neurosci* **33**, 18190-18199 (2013). https://doi.org/10.1523/JNEUROSCI.1592-13.2013

38 Ringstad, G., Vatnehol, S. A. S. & Eide, P. K. Glymphatic MRI in idiopathic normal pressure hydrocephalus. *Brain* **140**, 2691-2705 (2017). https://doi.org/10.1093/brain/awx191

39 Mestre, H. *et al.* Aquaporin-4-dependent glymphatic solute transport in the rodent brain. *Elife* **7** (2018). https://doi.org/10.7554/eLife.40070

40 Mestre, H. *et al.* Flow of cerebrospinal fluid is driven by arterial pulsations and is reduced in hypertension. *Nat Commun* **9**, 4878 (2018). https://doi.org/10.1038/s41467-018-07318-3

41 Jiang-Xie, L. F. *et al.* Neuronal dynamics direct cerebrospinal fluid perfusion and brain clearance. *Nature* **627**, 157-164 (2024). https://doi.org/10.1038/s41586-024-07108-6

42 Piantino, J., Lim, M. M., Newgard, C. D. & Iliff, J. Linking Traumatic Brain Injury, Sleep Disruption and Post-Traumatic Headache: a Potential Role for Glymphatic Pathway Dysfunction. *Curr Pain Headache Rep* **23**, 62 (2019). https://doi.org/10.1007/s11916-019-0799-4

43 Nedergaard, M. & Goldman, S. A. Glymphatic failure as a final common pathway to dementia. *Science* **370**, 50-56 (2020). https://doi.org/10.1126/science.abb8739

44 Goldman, N., Hablitz, L. M., Mori, Y. & Nedergaard, M. The Glymphatic System and Pain. *Med Acupunct* **32**, 373-376 (2020). https://doi.org/10.1089/acu.2020.1489

45 Braun, M. & Iliff, J. J. The impact of neurovascular, blood-brain barrier, and glymphatic dysfunction in neurodegenerative and metabolic diseases. *Int Rev Neurobiol* **154**, 413-436 (2020). https://doi.org/10.1016/bs.irn.2020.02.006

46 Gakuba, C. *et al.* General Anesthesia Inhibits the Activity of the "Glymphatic System". *Theranostics* **8**, 710-722 (2018). https://doi.org/10.7150/thno.19154

47 Miao, A. *et al.* Brain clearance is reduced during sleep and anesthesia. *Nat Neurosci* **27**, 1046-1050 (2024). https://doi.org/10.1038/s41593-024-01638-y

48 Kress, B. T. *et al.* Impairment of paravascular clearance pathways in the aging brain. *Ann Neurol* **76**, 845-861 (2014). https://doi.org/10.1002/ana.24271

49 Wang, M. *et al.* Focal Solute Trapping and Global Glymphatic Pathway Impairment in a Murine Model of Multiple Microinfarcts. *J Neurosci* **37**, 2870-2877 (2017). https://doi.org/10.1523/JNEUROSCI.2112-16.2017

50 Li, M. *et al.* Impaired Glymphatic Function and Pulsation Alterations in a Mouse Model of Vascular Cognitive Impairment. *Front Aging Neurosci* **13**, 788519 (2021). https://doi.org/10.3389/fnagi.2021.788519

51 Xu, Z. *et al.* Deletion of aquaporin-4 in APP/PS1 mice exacerbates brain Aβ accumulation and memory deficits. *Mol Neurodegener* **10**, 58 (2015). https://doi.org/10.1186/s13024-015-0056-1

52 Simon, M. *et al.* Loss of perivascular aquaporin-4 localization impairs glymphatic exchange and promotes amyloid β plaque formation in mice. *Alzheimers Res Ther* **14**, 59 (2022). https://doi.org/10.1186/s13195-022-00999-5

53 Pedersen, T. J., Keil, S. A., Han, W., Wang, M. X. & Iliff, J. J. The effect of aquaporin-4 mis-localization on Aβ deposition in mice. *Neurobiol Dis* **181**, 106100 (2023). https://doi.org/10.1016/j.nbd.2023.106100

54 Burfeind, K. G. *et al.* The effects of noncoding aquaporin-4 single-nucleotide polymorphisms on cognition and functional progression of Alzheimer's disease. *Alzheimers Dement (N Y)* **3**, 348-359 (2017). https://doi.org/10.1016/j.trci.2017.05.001

55 Zeppenfeld, D. M. *et al.* Association of Perivascular Localization of Aquaporin-4 With Cognition and Alzheimer Disease in Aging Brains. *JAMA Neurol* **74**, 91-99 (2017). https://doi.org/10.1001/jamaneurol.2016.4370

56 Simon, M. J. *et al.* Transcriptional network analysis of human astrocytic endfoot genes reveals region-specific associations with dementia status and tau pathology. *Sci Rep* **8**, 12389 (2018). https://doi.org/10.1038/s41598-018-30779-x

57 Instrumentation, A. N. S. I. A. f. A. o. M. Vol. EC12:2000/(R)2020 (2020).

58 Ayllon, D., Seoane, F. & Gil-Pita, R. Cole equation and parameter estimation from electrical bioimpedance spectroscopy measurements - A comparative study. *Annu Int Conf IEEE Eng Med Biol Soc* **2009**, 3779-3782 (2009). https://doi.org/10.1109/IEMBS.2009.5334494

59 De Lorenzo, A., Andreoli, A., Matthie, J. & Withers, P. Predicting body cell mass with bioimpedance by using theoretical methods: a technological review. *J Appl Physiol (1985)* **82**, 1542-1558 (1997). https://doi.org/10.1152/jappl.1997.82.5.1542

60 Gabriel, S., Lau, R. W. & Gabriel, C. The dielectric properties of biological tissues: III. Parametric models for the dielectric spectrum of tissues. *Phys Med Biol* **41**, 2271-2293 (1996). https://doi.org/10.1088/0031-9155/41/11/003

61 Welch, P. The use of the fast Fourier transform for the estimation of power spectra: A method based on time averaging over short, modified periodograms. *IEEE Trans. Audio Electroacoust* **15**, 70-73 (1967).

62 Vallat, R. & Walker, M. P. An open-source, high-performance tool for automated sleep staging. *Elife* **10** (2021). https://doi.org/10.7554/eLife.70092

63 Quinn, A. J., Lopes-Dos-Santos, V., Dupret, D., Nobre, A. C. & Woolrich, M. W. EMD: Empirical Mode Decomposition and Hilbert-Huang Spectral Analyses in Python. *J Open Source Softw* **6** (2021). https://doi.org/10.21105/joss.02977

64 Heart rate variability: standards of measurement, physiological interpretation and clinical use. Task Force of the European Society of Cardiology and the North American Society of Pacing and Electrophysiology. *Circulation* **93**, 1043-1065 (1996).

65 Janelidze, S. *et al.* Head-to-Head Comparison of 8 Plasma Amyloid-β 42/40 Assays in Alzheimer Disease. *JAMA Neurol* **78**, 1375-1382 (2021). https://doi.org/10.1001/jamaneurol.2021.3180

66 Roberts, K. F. *et al.* Amyloid-β efflux from the central nervous system into the plasma. *Ann Neurol* **76**, 837-844 (2014). https://doi.org/10.1002/ana.24270

67 Liu, H. *et al.* Acute sleep loss decreases CSF-to-blood clearance of Alzheimer's disease biomarkers. *Alzheimers Dement* (2023). https://doi.org/10.1002/alz.12930
68 Loh, S., Lamond, N., Dorrian, J., Roach, G. & Dawson, D. The validity of psychomotor vigilance tasks of less than 10-minute duration. *Behav Res Methods Instrum Comput* **36**, 339-346 (2004). https://doi.org/10.3758/bf03195580
69 Arsintescu, L. *et al.* Validation of a touchscreen psychomotor vigilance task. *Accid Anal Prev* **126**, 173-176 (2019). https://doi.org/10.1016/j.aap.2017.11.041
70 Arbuthnott, K. & Frank, J. Trail making test, part B as a measure of executive control: validation using a set-switching paradigm. *J Clin Exp Neuropsychol* **22**, 518-528 (2000). https://doi.org/10.1076/1380-3395(200008)22:4;1-0;FT518
71 *Digit Span (DGS)*, <https://cambridgecognition.com/digit-span-dgs/> (
72 *PVT Research Tool*, <https://apps.apple.com/tr/app/pvt-research-tool/id1475726298> (
73 Smith, A. *Symbol Digit Modalities Test*. (Western Psychological Association, 1992).
74 Reitan, R. *Trail Making Test: Manual for Administration and Scoring*. (1992).
75 Diagnostics, C. N. <https://c2n.com/> (
76 Piantino, J. *et al.* Link between Mild Traumatic Brain Injury, Poor Sleep, and Magnetic Resonance Imaging: Visible Perivascular Spaces in Veterans. *J Neurotrauma* **38**, 2391-2399 (2021). https://doi.org/10.1089/neu.2020.7447
77 Boespflug, E. L. *et al.* MR Imaging-based Multimodal Autoidentification of Perivascular Spaces (mMAPS): Automated Morphologic Segmentation of Enlarged Perivascular Spaces at Clinical Field Strength. *Radiology* **286**, 632-642 (2018). https://doi.org/10.1148/radiol.2017170205
78 Levendovszky, S. R. *et al.* Preliminary cross-sectional investigations into the human glymphatic system using multiple novel non-contrast MRI methods. *bioRxiv* (2023). https://doi.org/10.1101/2023.08.28.555150
79 Ohene, Y. *et al.* Non-invasive MRI of brain clearance pathways using multiple echo time arterial spin labelling: an aquaporin-4 study. *Neuroimage* **188**, 515-523 (2019). https://doi.org/10.1016/j.neuroimage.2018.12.026
80 Fultz, N. E. *et al.* Coupled electrophysiological, hemodynamic, and cerebrospinal fluid oscillations in human sleep. *Science* **366**, 628-631 (2019). https://doi.org/10.1126/science.aax5440
81 Fong, Y., Huang, Y., Gilbert, P. B. & Permar, S. R. chngpt: threshold regression model estimation and inference. *BMC Bioinformatics* **18**, 454 (2017). https://doi.org/10.1186/s12859-017-1863-x
82 Fong, Y., Di, C. & Permar, S. Change point testing in logistic regression models with interaction term. *Stat Med* **34**, 1483-1494 (2015). https://doi.org/10.1002/sim.6419
83 Farokhian, F., Yang, C., Beheshti, I., Matsuda, H. & Wu, S. Age-Related Gray and White Matter Changes in Normal Adult Brains. *Aging Dis* **8**, 899-909 (2017). https://doi.org/10.14336/AD.2017.0502
84 Ding, F. *et al.* Changes in the composition of brain interstitial ions control the sleep-wake cycle. *Science* **352**, 550-555 (2016). https://doi.org/10.1126/science.aad4821
85 Sun, Y. & Sun, X. Exploring the interstitial system in the brain: the last mile of drug delivery. *Rev Neurosci* **32**, 363-377 (2021). https://doi.org/10.1515/revneuro-2020-0057
86 Hotelling, H. New light on the correlation coefficient and its transforms. *Journal of the Royal Statistical Society. Series B (Methodological)* **15.2**, 193-232 (1953).